

Experimental and Theoretical Investigation of Relativistic Heavy Ion Collisions at RHIC – with Focus on Non-Central Collisions

PHD THESIS

WRITTEN BY: Máté Csanád



PHD SCHOOL OF PHYSICS
PARTICLE- AND ASTROPHYSICS PROGRAM

PHD SCHOOL LEADER: Dr. Zalán Horváth
PHD PROGRAM LEADER: Dr. Ferenc Csikor

SUPERVISOR: Dr. Ádám Kiss, professor
THESIS ADVISOR: Dr. Tamás Csörgő, scientific advisor

Eötvös University
Faculty of Natural Sciences
Budapest, Hungary
2007

Contents

1	Introduction	7
1.1	High energy heavy ion physics	8
1.2	General method of physics	9
1.3	Data taking - the Relativistic Heavy Ion Collider	9
1.4	Data analysis - correlation functions	11
1.5	Model building - the Buda-Lund hydro model	12
2	The PHENIX experiment at RHIC	13
2.1	The Relativistic Heavy Ion Collider	14
2.1.1	Tandem Van de Graaff generator	15
2.1.2	Linear Accelerator	15
2.1.3	The Booster synchrotron	15
2.1.4	The Alternating Gradient Synchrotron	16
2.1.5	The AGS to RHIC transfer line	16
2.2	The four RHIC experiments	17
2.2.1	BRAHMS	17
2.2.2	PHENIX	17
2.2.3	PHOBOS	18
2.2.4	STAR	18
2.3	The PHENIX	19
3	An online monitoring system for the Zero Degree Calorimeter	25
3.1	The zero degree calorimeter	26
3.1.1	Goals of the calorimeter	27
3.1.2	Construction of the ZDC	28
3.2	The online monitoring	28
3.2.1	Beam energy monitoring	29
3.2.2	Vertex position monitoring	29
3.2.3	LED signal monitoring	31
3.2.4	Expert plots	31

4	An online monitoring system for the Shower Max Detector	41
4.1	The Shower Max Detector	42
4.2	The SMD online monitoring	43
4.3	The Vernier scan	45
5	Two- and three-particle correlations at RHIC	53
5.1	Importance of correlation functions	54
5.2	Two-particle correlation functions	54
5.3	Three-particle correlation function	55
5.4	Dataset	56
5.5	Correcting for the Coulomb interaction	57
5.5.1	Definition and calculation the Coulomb-correction	57
5.5.2	Application of the Coulomb-correction	58
5.6	The effect of resonances on correlations	59
5.6.1	Basic definitions	60
5.6.2	The strength of the n -particle correlations	61
5.7	Partial coherence and core fraction of the source	62
5.8	The strength of two-particle correlations	63
5.9	Results summary	65
6	Two-particle source functions at RHIC	67
6.1	Power law tails in Au+Au collisions at RHIC	68
6.2	Assumption for the source function	68
6.3	Application to PHENIX data	70
6.4	Systematic tests	72
6.5	Direct fit to the experimental source functions	72
6.6	Determining the power law tail	81
7	Introduction to hydrodynamics	83
7.1	Relevance of hydrodynamics	84
7.2	Basic equations	84
7.3	Continuity, number density and the velocity field	86
7.4	The Euler-equation and the pressure	87
7.5	The energy equation and the temperature	89
7.6	Observables	89
8	Buda-Lund hydro model for ellipsoidally symmetric fireballs	93
8.1	Axially symmetric hydrodynamics	94
8.1.1	The Buda-Lund model	94
8.1.2	Transition from deconfined to hadronic matter	94

8.1.3	General Buda-Lund hydrodynamics	95
8.2	Ellipsoidal Buda-Lund hydro model	97
8.2.1	Buda-Lund hydro for relativistic, ellipsoidal expansions	98
8.2.2	Integration and saddlepoint approximation	101
8.3	The invariant momentum distribution	104
9	Elliptic flow from the Buda-Lund model	107
9.1	Elliptic flow in high energy heavy ion collisions	108
9.2	Calculating the elliptic flow	108
9.3	Elliptic flow for tilted ellipsoidal expansion	110
9.4	Universal scaling of the elliptic flow at RHIC	113
9.5	Comparison to experimental data	116
10	Correlation functions from the Buda-Lund model	123
10.1	The correlation function	124
10.2	Rapidity dependent HBT radii	126
11	From Quark Gluon Plasma to a Perfect Fluid of Quarks	131
11.1	Perfect fluids at RHIC	132
11.1.1	A sign for hydrodynamic behavior: elliptic flow	132
11.1.2	Relativistic perfect fluids	132
11.2	Characterizing the matter produced at RHIC	133
11.2.1	An advanced estimate on the initial energy density	133
11.2.2	Estimating the freeze-out temperature	134
11.2.3	Universal scaling of the elliptic flow	134
11.2.4	Chiral symmetry restoration	136
11.3	Summary of the results	137
	Statement of Contributions	138
	Acknowledgements	141
	List of figures	142
	List of tables	144
	Bibliography	145

Chapter 1

Introduction

Oh infinite heavens open, open up

Your hidden sacred volumes to my sight

THE TRAGEDY OF MAN, IMRE MADÁCH

“We simply do not yet know enough about the physics of elementary particles to be able to calculate the properties of such a melange with any confidence. . . . Thus our ignorance of microscopic physics stands as a veil, obscuring our view of the very beginning.”

S. Weinberg, about the first hundredth of a second [1]

1.1 High energy heavy ion physics

Ultra-relativistic collisions, so called “Little Bangs” of almost fully ionized Au atoms are observed at the experiments of the Relativistic Heavy Ion Collider of the Brookhaven National Laboratory, New York. The aim of these experiments is to create new forms of matter that existed in Nature a few microseconds after the Big Bang, the creation of our Universe.

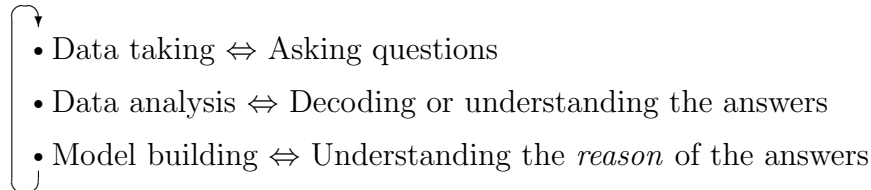
Quantum Chromodynamics (QCD), the theory of quarks and gluons, their color degree of freedom and the strong force interacting between them was established soon after Weinberg’s famous book [1] about the early Universe had been published. Confinement is an important (though mathematically never proven) property of QCD, its consequence is that quarks are bound into hadrons in a matter of normal temperature and pressure.

In the early Universe, energy density was many orders of magnitude higher than today, and at that high energy densities, deconfined phases of colored matter might have existed. Quark-gluon plasma (QGP) is such a phase, that might have existed during the first few microseconds after the Universe came into existence. This type of matter was searched for at the SPS, and experiments at RHIC are continuing this effort. Evidence for formation of a hot and dense medium in gold-gold collisions was found based on a phenomenon called jet quenching, and confirmed by its disappearance in deuteron-gold collisions [2].

A consistent picture emerged after the first three years of running the RHIC experiment: quarks indeed become deconfined, but also behave collectively, hence this hot matter acts like a liquid [3], not like an ideal gas theorists had anticipated when defining the term QGP. The situation is similar to as if prisoners (quarks and gluons confined in hadrons) have broken out of their cells at nearly the same time, but they find themselves on the crowded jail-yard coupled with all the other escapees. This strong coupling is exactly what happens in a liquid [4].

1.2 General method of physics

Physics, as a natural science, works in a way very similar to psychoanalysis, just Nature is our subject of investigation. The three main steps in researching the secrets of nature are data taking, data analysis and model building. These three steps are analogous to a situation, where one wants to get to know another person, by asking questions. The analogies for the three steps are:

- 
- Data taking \Leftrightarrow Asking questions
 - Data analysis \Leftrightarrow Decoding or understanding the answers
 - Model building \Leftrightarrow Understanding the *reason* of the answers

There is one more step, which makes this above process to a continually rising helix. This is represented above by the curved arrow, and means, that a model has to make predictions and call the next questions to see if they are right, and then comes the next answer, the next model and the next prediction, which calls a question again, and so on.

It is very important to see the whole process. For example, the one who tries to understand the reason of the answers, knows what questions to ask. Similarly the asker understands the answers better, because he/she knows to most details about the asked question.

This is not a big problem in the process of getting to know a person, where learning and practicing the separate tasks do not require a whole life, especially the second task, which is done by our ears and brain automatically.

In physics, the situation is not so easy. While the first two tasks are often done by the same people, the third is mostly separated from them. In my present Ph.D. thesis, I would like to show examples for all three tasks. The examples are from the field of heavy ion physics, but they are on different topics, and give insight into different kind of problems.

After this short introduction, let us see a description and some details of the three parts.

1.3 Data taking - the Relativistic Heavy Ion Collider

The front line of asking questions from Nature in the field of high energy heavy ion physics is at heavy ion colliders. Currently, the largest one is in Brookhaven on Long Island, New York, and this is the Relativistic Heavy Ion Collider. Here heavy (or sometimes not so

heavy) ions are accelerated to enormous energies and collided to each other. In these high energy collisions lots of new particles are produced, and through observing properties of these particles, we may see circumstances similar to the ones present at the birth of our Universe, the Big Bang.

The first part of the accelerating is done by pre-accelerators, and then two high speed beams of ions (grouped into bunches) are led in two co-centered rings, and are further accelerated in reverse directions in these rings. The two beams cross each other at six points, here, if the bunches are synchronized, ion-ion collisions can happen. At four of these crossings there is an experiment. These experiments are aggregations of detectors, which measure different properties of the particles produced in the collisions to find out how the matter looked like at the pressures and temperatures that were reached at a collision.

This type of experimentation is similar to a situation where we had only ice on the Earth, but thought, some other forms of water might possibly be formed under high pressure or at high temperature. So we accelerate pieces of ice and collide them together. Then from the re-frozen ice particles that are coming out of the collision we would try to figure out, if some liquid or gas form of water was formed, before the water pieces flew out to our detectors. In our case, we think, hadronic matter might possibly be melted or evaporated into a matter that has more degrees of freedom.

I was involved in data taking at one of these experiments, in PHENIX (Pioneering High ENergy Ion eXperiment). It consists of many detectors, there are some that measure the momentum of the particles, some measure the charge, then time of flight in the detectors and pathlength is measured, and so on.

With these detectors we can ask questions from Nature, for example we could ask:

“Is the spectrum of pions in such collisions a thermal spectrum?”

“Are there among the products of these collisions any pentaquarks?”

“What is the temperature of the center of the system that comes into existence after the collision?”

It is of primary importance that we have to build detectors, which “understand” our questions, eg. if we cannot identify particles, we won’t be able to measure the pion spectrum. Or, we have to build detectors, which have a high enough acceptance to measure the decomposition products of pentaquarks. And, our heavy ion collisions have to be intense

enough to have a big enough amount of particles.

Furthermore, all these questions depend more or less on idea on the meaning of the words in them. For example, it is a question, what we consider as temperature in those collisions, or how we want to identify pentaquarks.

There is a need to see the whole process of physics in one, and not just say: we are experimental physicists, and do not care about theories. Another problem could be, if one builds a model without respect to Nature. A model may be the most original and creative and beautiful model ever made, if it does not describe Nature, it's beauty does not correct this problem.

1.4 Data analysis - correlation functions

Data analysis means decoding and understanding the answers. For example we have to extract the particular events from the digitalized signal of the detectors, the particles in the events and their physical properties. After that, if we have the particles, we can measure eg. the pion spectrum or the correlation functions.

Correlation functions measure, how correlated the momenta of the particles in an ensemble are. For example, there are the two particle correlation functions, which depend on the two momenta of particle pairs, but can be projected on the sub-space of the momentum-difference of the pair. If the correlation function is high at zero relative momenta, it means, that there are many particles with nearly the same momentum.

Correlation functions are important to see the collective behavior or properties of particles. For example the observed size of a system can be measured by looking at two particle Bose-Einstein correlations. From the three-particle correlation functions we can conclude about the particle production, whether it was partly coherent or not, or how much does it undergo collective dynamics.

But until we get from particle-ensemble to the correlation function, there is a long way, which includes understanding the detectors to be able to make necessary corrections on the measurement and understanding the theory of correlations to be able measure the *right* correlation functions.

1.5 Model building - the Buda-Lund hydro model

We build models to understand reason of the answers. We imagine possible answerers, and if we see, that for example this answerer would have given other answers, that we have heard, we can tell, that the answerer is unlike this picture. And in most cases, the real quest is to find one answerer at all, that would give the same answers. And then, we are back at the first step, ask questions to see, if the answerer is really like what we imagined.

The Buda-Lund model is a hydrodynamical model which was developed to describe the 'Little Bang', the heavy ion collisions. It includes a solution of the equations of hydrodynamics, and calculates for a given set of parameters particle spectra, correlations functions and other observable quantities measured in heavy ion collisions. It assumes the existence of an expanding fireball arisen from the hot zone of these collisions and it's input parameters are the fireballs temperature and flow profile. After fitting the results of the model to the data, these input parameters can be determined.

Finally, with the found set of parameters, it is possible to make predictions for not fitted quantities also. If we measure these quantities, we can make refinements on the model to get a more clear picture. But only who works on the model knows, which observable quantities can be predicted from the model, or which measurements could exclude or confirm some characteristic features of the model.

“In general we look for a new law by the following process. First we guess it. Then we compare the consequences of the guess to see what would be implied if this law that we guessed is right. Then we compare the result of the computation to nature, with experiment or experience, compare it directly with observation, to see if it works. If it disagrees with experiment it is wrong.

In that simple statement is the key to science.

It does not make any difference how beautiful your guess is. It does not make any difference how smart you are, who made the guess, or what his name is — if it disagrees with experiment it is wrong.”

R. P. Feynman, about discovering new laws [5]

Chapter 2

The PHENIX experiment at RHIC

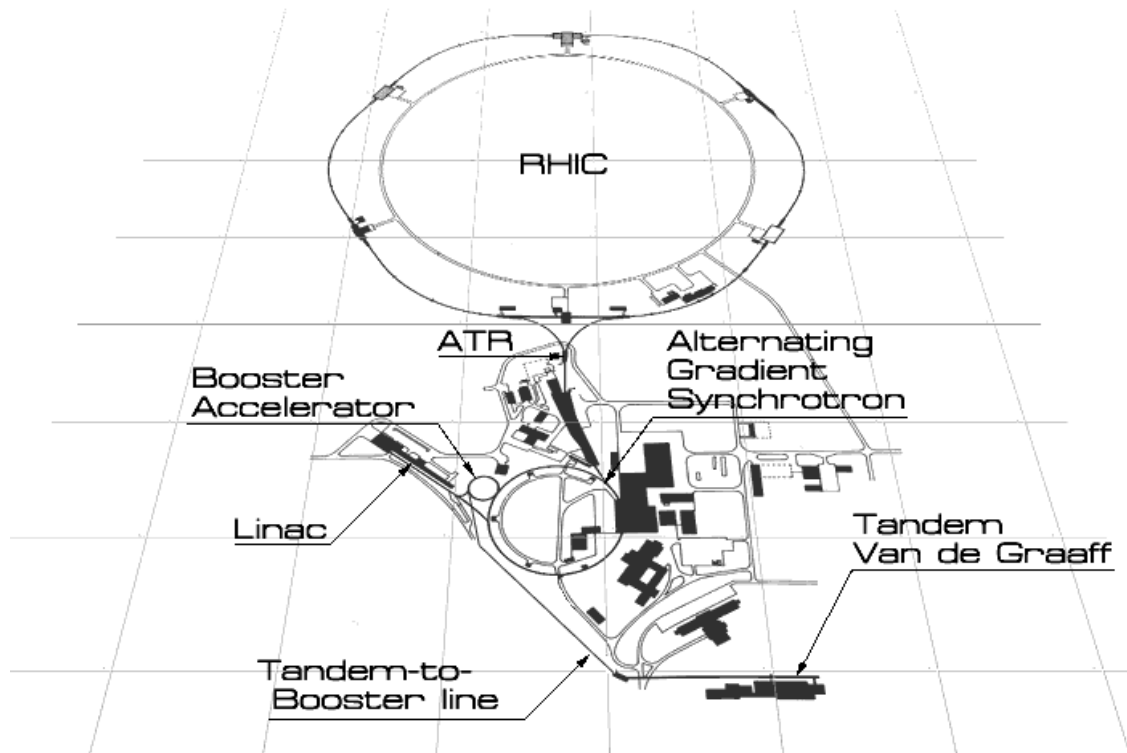


Figure 2.1: Aerial view of RHIC

On this figure, we see the RHIC ring and its pre-accelerator facilities. Gold ions start their journey in the Tandem Van de Graaff generator, then they travel to the Booster accelerator, after that they are accelerated to a higher speed in the Alternating Gradient Synchrotron, and finally they are injected into the RHIC ring where they reach their final speed and collide into one another.

2.1 The Relativistic Heavy Ion Collider

The Relativistic Heavy Ion Collider (RHIC) at Brookhaven National Laboratory is a research facility that began operation in 2000, following 10 years of development and construction. Hundreds of physicists from around the world use RHIC to study what the universe may have looked like in the first few moments after its creation. RHIC drives two intersecting beams of gold ions into a subatomic collision. These collisions may help us understand more about why the physical world works the way it does, from the smallest subatomic particles, to the largest stars.

An areal view of the RHIC complex with all its facilities is shown on fig. 2.1.

2.1.1 Tandem Van de Graaff generator

Completed in 1970, the Tandem Van de Graaff facility was for many years the world's largest electrostatic accelerator facility. It provides accelerated ion-beams ranging from hydrogen to uranium. The facility consists of two 15 million volt electrostatic accelerators, each about 24 meters long, aligned end-to-end.

To study heavy ion collisions at high energies, a 700 meter-long tunnel and beam transport system called the Tandem to Booster (TtB) Line was completed in 1986. From the Tandem, the bunches of ions enter the Tandem to Booster Line, which carries them through a vacuum via a magnetic field to the Booster. At this point, they are travelling at about 5% of the speed of light. This facility allows the delivery of heavy ions from Tandem to the Alternating Gradient Synchrotron (AGS) for further acceleration. The TtB now makes it possible for the Tandem to serve as the Relativistic Heavy Ion Collider's ion source.

2.1.2 Linear Accelerator

In addition to heavy ions, also proton-proton collisions are studied at RHIC. For these measurements, protons are supplied by the Linear Accelerator (Linac).

The basic components of the Linac include ion sources, a radiofrequency quadrupole pre-injector, and nine accelerator radiofrequency cavities spanning the length of 140 meter. The Linac is capable of producing up to a 35 milliamper proton beam at energies up to 200 MeV for injection into the AGS Booster or for the activation of targets at the Brookhaven Linac Isotope Producer. The Linac's location relative to the rest of the AGS complex is shown on fig. 2.1.

2.1.3 The Booster synchrotron

The Booster synchrotron is used to pre-accelerate particles entering the AGS ring. It's construction was begun in 1986 and completed in 1991. The Booster is less than one quarter the size of the AGS.

The Booster also plays an important role in the operation of the Relativistic Heavy Ion Collider (RHIC) by accepting heavy ions from the Tandem Van de Graaff facility via the Tandem to Booster beamline. It then feeds them to the AGS for further acceleration and

delivery to RHIC. Due to its superior vacuum, the Booster makes it possible for the AGS to accelerate and deliver heavy ions up to gold with its atomic mass of 197.

2.1.4 The Alternating Gradient Synchrotron

The Alternating Gradient Synchrotron name is derived from the concept of alternating gradient focusing, in which the field gradients of the accelerator's 240 magnets are successively alternated inward and outward, permitting particles to be propelled and focused in both the horizontal and vertical plane at the same time. Capable of accelerating 25 trillion protons with every pulse, and heavy ions such as gold and iron, the AGS is used by 850 users from 180 institutions from around the world annually.

As ions enter the AGS from the Booster, they are travelling at about 37% the speed of light. Then in the AGS, the velocity of the ions reaches 99.7% the speed of light.

Since 1960, the Alternating Gradient Synchrotron (AGS) has been one of the world's premiere particle accelerators, well known for the three Nobel Prizes won as a result of research performed there:

- In 1976, Samuel C.C. Ting and Burton Richter "for their pioneering work in the discovery of a heavy elementary particle of a new kind". In other words: for discovery of the J/Ψ particle as it confirmed the idea that baryonic matter is made out of quarks.
- In 1980, James Watson Cronin and Val Logsdon Fitch, "for the discovery of violations of fundamental symmetry principles in the decay of neutral K-mesons", i.e. the CP violation.
- In 1988, Leon Max Lederman, Melvin Schwartz, and Jack Steinberger "for the neutrino beam method and the demonstration of the doublet structure of the leptons through the discovery of the muon neutrino".

2.1.5 The AGS to RHIC transfer line

When the ion beam is travelling at top speed in the AGS, it is diverted to another beam line called the AGS to RHIC transfer line. At the end of this line, there is a "fork in the road", where a switching magnet sends the ion bunches down one of two beam lines. Bunches are

directed either left to the clockwise RHIC ring or right to travel counter-clockwise in the second RHIC ring. From here on, the counter-rotating beams are accelerated, as in the Booster and AGS, and then circulate in RHIC where they will be collided into one another at six interaction points.

2.2 The four RHIC experiments

RHIC's 2.4 mile ring has six intersection points where its two rings cross each other, allowing the particle beams to collide.

If RHIC's ring is thought of as a clock, the four current experiments are at 2 o'clock (BRAHMS), 6 o'clock (STAR), 8 o'clock (PHENIX) and 10 o'clock (PHOBOS) and. There are two additional intersection points at 12 and 4 o'clock where there are no experiments, but in the future some may be placed.

Let us now see some details about the four experiments.

2.2.1 BRAHMS

One of RHIC's two smaller detectors is the Broad Range Hadron Magnetic Spectrometer, or "BRAHMS". This device studies charged hadrons as they pass through its spectrometers.

BRAHMS measures only a small number of particles emerging from a specific set of angles during each collision. The momentum, energy and other characteristics of the particles are measured very precisely.

This collaboration has 51 participants from 14 institutions in eight countries. It was last operational in 2006 (RHIC Run 6).

2.2.2 PHENIX

The PHENIX detector records many different particles emerging from RHIC collisions, including photons, electrons, muons, and hadrons.

Photons and leptons are not affected by the strong interaction and can emerge unchanged from the interior of a RHIC collision, so they carry unmodified information about processes within the collision. A good analogy is that PHENIX looks "inside" the hot, dense matter

formed in the collision, much like x-ray or MRI images show medical doctors the “inside” of the human body. For example, escaping photons can reveal information about the initial temperatures reached in the collision.

PHENIX weighs 4,000 tons and has a dozen detector subsystems. Three large steel magnets produce high magnetic fields to bend charged particles along curved paths. Tracking chambers record hits along the flight path to measure the curvature and thus determine each particle’s momentum. Other detectors identify the particle type and/or measure the particle’s energy. Still others record where the collision occurred and determine whether each collision was a central one, a peripheral one, or something in between.

PHENIX has around 500 members from 69 institutions in 14 countries. A more detailed description of PHENIX is shown in the next section.

2.2.3 PHOBOS

The PHOBOS experiment is based on the premise that interesting collisions will be rare, but that when they do occur, new physics will be readily identified. Thus PHOBOS is designed to examine and analyze a very large number of unselected gold ion collisions. It consists of many silicon detectors surrounding the interaction region. With these detectors, it is possible to count the total number of produced particles and study their angular distribution. With this array one can look for unusual events, such as fluctuations in the number of particles or angular distribution, because it is known from other branches of physics that a characteristic of phase transitions is a fluctuation in observable events.

Seventy scientists from 12 institutions in three nations are working on PHOBOS. It was last operational in 2006 (RHIC Run 6), and it is being demounted in 2007.

2.2.4 STAR

The Solenoidal Tracker at RHIC (STAR) is an experiment which specializes in tracking the thousands of particles produced by each ion collision at RHIC. STAR’s “heart” is the Time Projection Chamber, which tracks and identifies particles emerging from the heavy ion collisions. As a collision occurs, STAR measures many parameters simultaneously to look for signs of the quark-gluon plasma. By using powerful computers it reconstructs the

sub-atomic interactions which produce the particles emerging from the collision.

The STAR team is composed of 550 collaborators from 46 institutions in 12 countries.

2.3 The PHENIX

The PHENIX Experiment consists of detectors, each of which perform a specific role in the measurements of a heavy ion collision. The detectors are grouped in two central arms and two muon arms. The ones in the central arms are capable of measuring a variety of particles including pions, protons, kaons, deuterons, photons, and electrons. The ones in the two muon arms focus on the measurement of muon particles. There are also additional event characterization detectors that provide additional information about a collision, and a set of three huge magnets that bend the trajectories of the charged particles. In tables 2.1-2.2 is a short description of the detectors. How they are arranged is shown on fig. 2.2.

The primary goal PHENIX was designed to achieve is to discover and study a new state of matter called the Quark-Gluon Plasma (QGP). This form of matter was predicted from perturbative QCD calculations to exist when quarks and gluons are not bound inside of nucleons. Our Universe is thought to have been in this state for a very short time after it's birth. There is still no real consensus in physics, what we consider as the QGP, and if we have already seen it or not. The situation is a little bit similar to that of Columbus, who thought to have found India, but it took decades until it was clear where his ships dropped the anchors [6].

Now, the science mission of PHENIX can be summarized as follows:

- Search for a new state of matter believed to be the state of matter existing in the universe shortly after the Big Bang. If it is found, then measure its properties.
- Study matter under extreme conditions of temperature and pressure.
- Study the most basic building blocks of nature like quarks and gluons, and the forces that govern them.

The milestone discoveries of PHENIX are the following.

There appears to be suppression of particles with a high transverse momentum (p_t) in Au+Au collisions at $\sqrt{s_{NN}}=200$ GeV [7,8]. PHENIX observes that there are fewer particles

Particle Characterization Detectors	
Drift Chamber (DC)	Measures the position and momentum of charged particles
Pad Chambers (PC)	Measures the position of charged particles with precision
Aerogel Cherenkov Counter	Identifies particles at high transverse momentum.
Ring Imaging Cherenkov Detector (RICH)	Identifies electrons
Time Expansion Chamber (TEC)	Measures the position and momentum of charged particles. Identifies particles.
Time-of-Flight (TOF)	Measures the position of charged particles. Identifies particles.
Electromagnetic Calorimeter (EMCal)	Measures the position and energy of charged and neutral particles. Identifies photons and charged particles. Has two types of detectors: Lead scintillator (PbSc) and lead glass (PbGl)
Hadron Blind Detector (HBD)	Identifies electrons in the high density hadron environment
Event Characterization Detectors	
Beam-Beam Counters (BBC)	Measures collision (vertex) position and centrality. Starts the stopwatch for an event.
Multiplicity Vertex Detector (MVD)	Measures vertex position and charged particle distributions.
Reaction Plane Detector (RxnP)	Measures reaction plane with high resolution.

Table 2.1: PHENIX central arm detectors

Muon Arm Detectors	
Muon Tracker (MuTr)	Measures position and momentum of muons
Muon Identifier (MuID)	Identifies muons
Muon Piston Calorimeter (MPC)	Measures neutral pions, eta particles, and jets over the region of $3.0 < \eta < 4.0$.
Event Characterization Detectors	
Zero Degree Calorimeters (ZDC)	Measures collision location and centrality.
Forward Calorimeters (FCal)	For deuteron+Au collisions, it can measure surviving neutrons and protons from the original deuteron.
“Heavy” Metal Detector	
PHENIX Magnets	Bends charged particles so that charge and momentum can be measured in both the central arm and the muon arm detectors.

Table 2.2: PHENIX detectors outside of the central arm

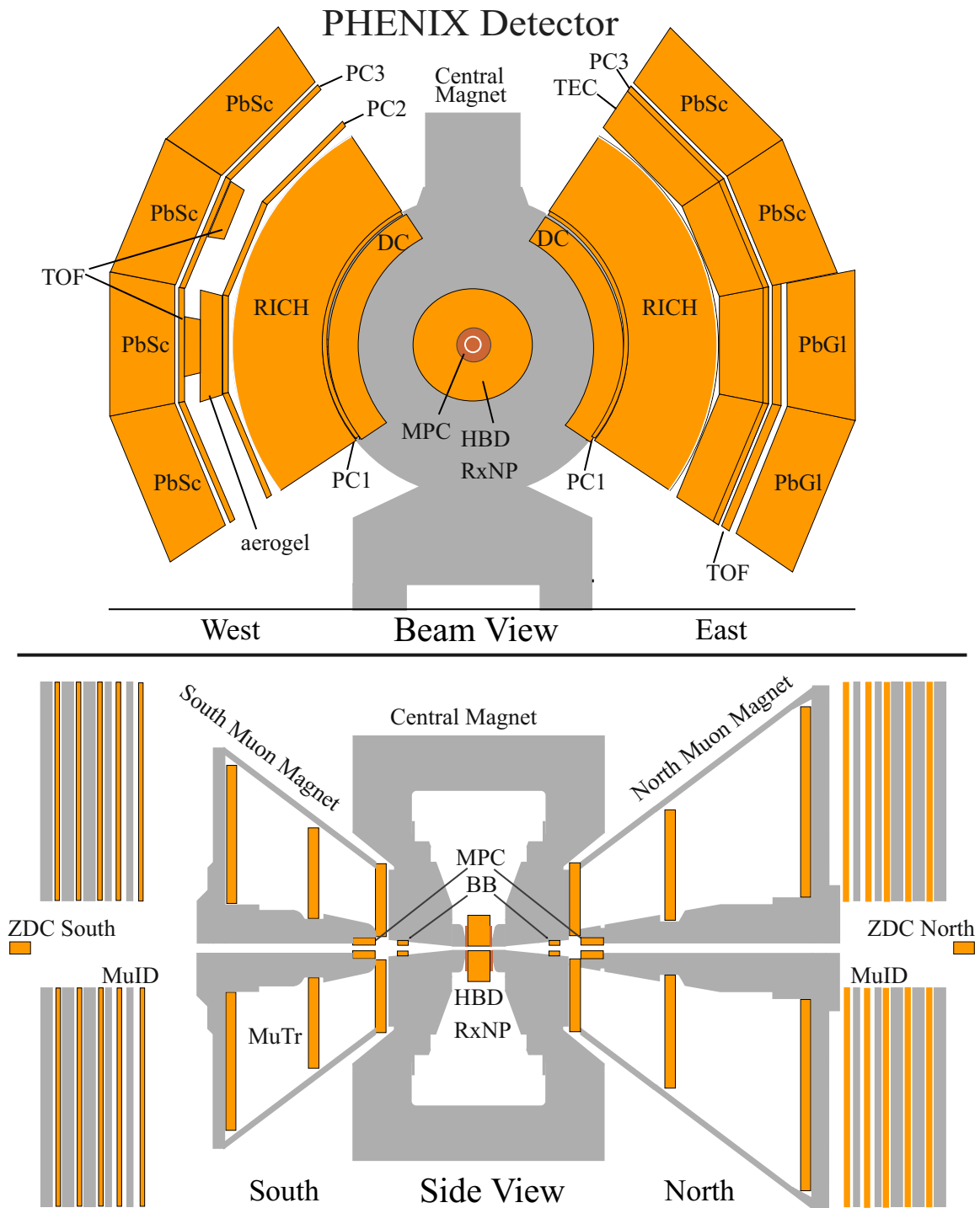


Figure 2.2: Detector arrangement in PHENIX during Run 7

with a high transverse momentum than what is expected from measurements of simpler proton collisions. This effect is referred to as jet suppression, since the majority of these particles are products of a phenomenon called jets, high energy and high transverse momentum particles. Jet suppression was predicted to occur if the QGP is formed, because of the energy loss of partons in the dense and hot matter.

There does not appear to be suppression of particles with a high transverse momentum in d+Au (deuteron+gold) collisions [2]. In these collisions, due to the small size of the deuteron, QGP can be formed only a very small region. This observation confirms that the suppression seen in Au+Au collisions is most likely due to the influence of a hot, dense and strongly interacting matter being produced in big enough quantities, such as a Quark-Gluon Plasma.

PHENIX is unique at RHIC in that it can identify individual electrons coming from the collision, many of which are the result of decays of heavier particles within the collision. PHENIX measures a number of electrons that is above the expected background [9]. The excess electrons are likely coming from decays of special particles with heavy charm quarks in them. Further study of these charmed particles will help us better understand if the Quark-Gluon Plasma has been formed.

PHENIX has measured the fluctuations in the charge and average transverse momentum of each collision, because during a phase transition, it is typical to see fluctuations in some properties of the system. So far, PHENIX reports no large charge fluctuations that might be seen if there is a phase transition from a Quark-Gluon Plasma [10]. PHENIX reports that there are excess fluctuations in transverse momentum, but they appear due to the presence of particles from jets [11]. The behavior of the fluctuations is consistent with the jet suppression phenomenon mentioned previously. Recent lattice calculations indicate, that the QGP may be formed in a cross-over like transition, so we do not have to see signs of a phase-transition necessarily, but these features need further investigation.

PHENIX observes high values of elliptic flow [12, 13]. The extracted flow values show significant sensitivity to both the collision centrality and the transverse momenta of emitted hadrons, suggesting rapid thermalization and relatively strong velocity fields. When scaled by the eccentricity of the collision zone, the scaled elliptic flow shows little or no dependence on centrality for charged hadrons with relatively low transverse momentum. A breakdown of

this scaling is observed for charged hadrons with $p_t > 1$ GeV/ c for the most central collisions. We also observe that the elliptic flow for all particles reaches a maximum at mid-centrality, and increases with p_t up to 2 GeV and then saturates or decreases slightly. Our results depart from hydrodynamically predicted behavior for $p_t > 2$ GeV/ c .

For transverse kinetic energies up to ~ 1 GeV, a scaling of the elliptic flow compatible with the hydrodynamic expansion of a thermalized fluid was observed for all produced particles. For large values of kinetic energy, the mesons and baryons scale separately. A broader type of scaling for the flow of both mesons and baryons is observed for the full transverse kinetic energy range of the data when quark number scaling is employed. [14]

PHENIX also made the first extraction of the full 1D emission source function for pions in Au+Au collisions at $\sqrt{s_{NN}} = 200$ GeV. [15]

Has PHENIX found the Quark-Gluon Plasma? What we can say, is that PHENIX found compelling experimental evidence [3] that heavy-ion collisions at RHIC produce a state of matter characterized by very high energy densities, density of unscreened color charges ten times that of a nucleon, large cross sections for the interaction between strongly interacting particles, strong collective flow, and early thermalization. Measurements indicate that this matter modifies jet fragmentation and has opacity that is too large to be explained by any known hadronic processes. This state of matter is not describable in terms of ordinary color-neutral hadrons, because there is no known self-consistent theory of matter composed of ordinary hadrons at the measured densities. Note however the surprising success of Humanic's Hadronic Rescattering Code (HRC) [16] that describes observables at RHIC in terms of ordinary hadrons with PDG standard, momentum dependent cross sections. Keeping this virtue of HRC in mind, still the most economical description is in terms of the underlying quark and gluon degrees of freedom. Models taking this approach have scored impressive successes in explaining many, but not all, of the striking features measured to date. There is not yet irrefutable evidence that this state of matter is characterized by quark deconfinement or chiral symmetry restoration, which would be a direct indication of quark-gluon plasma formation. The anticipated program of additional incisive experimental measurements combined with continued refinement of the theoretical description is needed to achieve a complete understanding of the state of matter created at RHIC.

Chapter 3

An online monitoring system for the Zero Degree Calorimeter

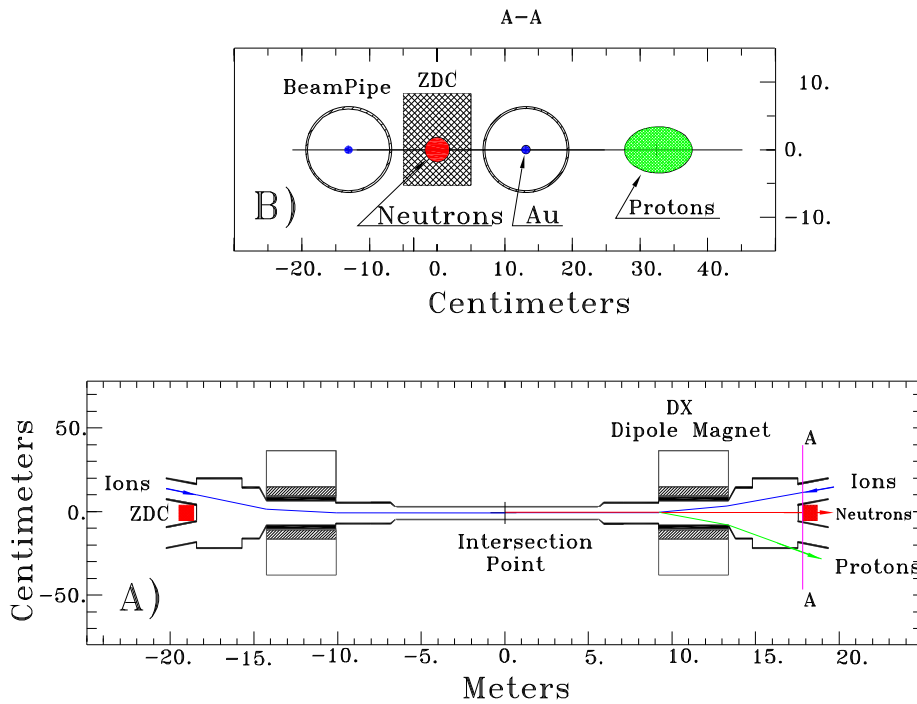


Figure 3.1: Plan view of the collision region "beam's eye" view of the ZDC location

3.1 The zero degree calorimeter

The Zero Degree Calorimeter (ZDC) is a neutron detector, which is placed in the line where the two beams of RHIC cross each other (the interaction region). It is present at all four experiments of the Relativistic Heavy Ion Collider and may be considered to be part of RHIC instrumentation also.

The ZDC was designed as a detector for luminosity measurement and monitoring, event geometry characterization. In heavy ion collisions it is used for centrality selection (with the Beam Beam Counters), to study Coulomb-dissociation, nuclear fragmentation processes, investigation of $\gamma\text{-}\gamma$ collisions, etc. In d+Au runs the ZDC (together with the Forward Hadron Calorimeter) is used for $p(d)+\text{Au} \rightarrow n+X$, $n(d)+\text{Au} \rightarrow p+X$, $d+\text{Au} \rightarrow X$ event classification [17–19].

My task at the ZDC was to develop the online monitoring software for this detector component. The online monitoring is a program that has to produce plots from the data that is currently taken.

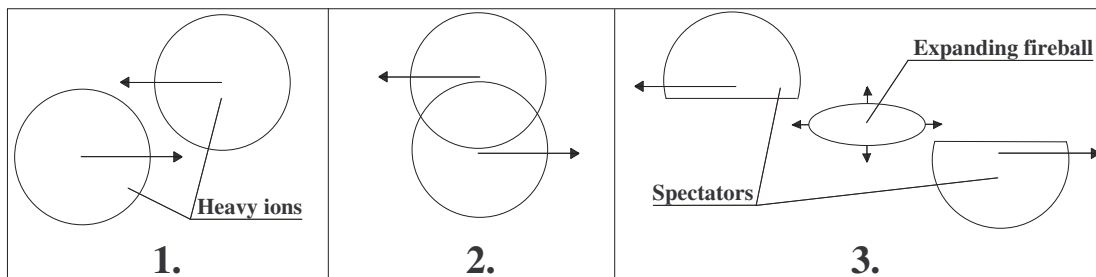


Figure 3.2: Sketch of a high energy heavy ion collision

In the first part, the two heavy ions are nearing to each other. Lorentz-contraction is neglected here to have a more clear picture. After that, they collide. From the region where they overlap arises an expanding fireball of new particles, and the other parts, the so called spectators continue their way. From these parts, protons and neutrons evaporate.

3.1.1 Goals of the calorimeter

It measures the energy of the neutrons that are evaporated from the spectators of the collision. These neutrons do not take part in the collision, and if they decouple from the protons, the magnetic field will not guide them to stay in the beampipe, and go straight forward into the Zero Degree Calorimeter, see fig. 3.1.

The energy of these neutrons can be computed from the center of mass energy ($\sqrt{s_{NN}}$). If we use the center of mass frame, where $\mathbf{p}_1 = -\mathbf{p}_2 = \mathbf{p}$:

$$s_{NN} = (p_1 + p_2)^2 = 2m^2 + 2(|\mathbf{p}|^2 + E^2) = 4E^2 \quad (3.1)$$

So, by measuring the energy of the evaporated neutrons, we access the fluctuations of the center of mass energy.

Another purpose of the ZDC is to measure the vertex position, the position, where the collision happened. This is possible, because the evaporated neutrons start their flight with the spectator part of the nucleus at the same time from the collision point. If in one direction, the neutrons reach the ZDC earlier, the vertex was nearer to this side. This is possible, because we read out not only energy, but timing information, too. The velocity of the neutrons equals within error the speed of light.

Expressed with these formulas:

$$z_{vertex} = (t_{south} - t_{north})c, \quad (3.2)$$

$$t_{vertex} = (z_{vertex} - L_{ZDC})/c, \quad (3.3)$$

if t_{south} and t_{north} are times when the neutron-shower was detected in the ZDC's and L_{ZDC} is the distance of the two ZDC's.

3.1.2 Construction of the ZDC

The Zero Degree Calorimeter is a Cherenkov light sampling calorimeter, and there is one at both ends of the interaction region.

Mechanically, each arm of the ZDC is subdivided into 3 identical modules with 2 interaction length each. The active medium is made from clear acrylic fibers interleaved with Tungsten absorber plates. This sandwich structure is tilted at 45 degree to the beam to align the optical fibers with the Cherenkov angle of forward particles in the shower. The energy resolution of the ZDC for 100 GeV neutrons is 21%. Time resolution is around 120 ps for 100 GeV neutrons which may be translated into a vertex position resolution of around 2.5cm.

The three analog signals coming from the slabs are digitalized after some amplifying, as well as their analog sum, and a timing signal for each channel. This information is then stored and analyzed by computers. Channel numbering is shown in table 3.1.

The energy is calibrated with an LED, which pulses with a low frequency. We take some events where there was no collision only an LED pulse, and we know the energy of the LED signal, and through this, energy of the detected particles can be calibrated. We monitor the LED energy too.

3.2 The online monitoring

The PHENIX Online Monitoring [20] is a software system, that has the purpose to monitor the data that is taken at the moment. For every detector-component there has to be an online monitor program, because if there won't be one, we might not notice that that particular component is not working properly, and the data from that detector is unusable.

channel	number
south analog sum	0
south slabs	1-3
north analog sum	4
north slabs	5-7

Table 3.1: ZDC channels

There are eight ZDC channels, six for the south and north slabs, and two more for the analog sums of these channels.

In this section, I show some plots of the ZDC and SMD online monitor. The code is available in ref. [21].

The code is part of the PHENIX Online Monitoring framework, and as such, `MakeCanvas` functions in `ZdcMonDraw.C` prepare the canvases and `Draw` functions draw the plots themselves. These plots have to be filled/computed in `ZdcMon.C`. Which `Draw` function produces which plot is shown in table 3.2.

3.2.1 Beam energy monitoring

We have a monitor for south and north beam energy. The upper panels in figs. 3.3 and 3.4 show the energy distribution in the north and south ZDC. The red dashed lines show the allowed region for the maximum of the curve. This is around 1700-1900 GeV for gold beam, and at 100 GeV for deuterium beam. In the latter case, we can have only one evaporated neutron, so the energy should be around 100 GeV, and in the former case, we saw, that the most likely number of evaporated neutrons is 17-19, so this energy region should be maintained.

3.2.2 Vertex position monitoring

We have a monitor for the south and north beam position. The left middle panel in figs. 3.3 and 3.4 show the vertex position, and the middle right is the same just for the events where the BBC level 1 trigger fired. The latter, corrected distribution has a gaussian shape, because if we have an event, where BBC level 1 trigger did not fire, it is very likely,

Plot	Drawing function	name
3.3-3.4	Draw1()	ZDC Main Monitor
4.3-4.4	Draw2()	SMD Expert Data
4.5	Draw3()	SMD Position Values
3.5	Draw4()	LED Energy Values
3.6	Draw5()	LED Timing Values
4.6	Draw6()	SMD Values South
4.6	Draw7()	SMD Values North
3.9	Draw8()	ZDC Ratio Values
3.10	Draw9()	ZDC BBC Vertex
3.7	DrawHistory(,0)	ZDC PPG History
4.7	DrawHistory(,1)	SMD South Y PPG History
4.7	DrawHistory(,2)	SMD South X PPG History
4.7	DrawHistory(,3)	SMD North Y PPG History
4.7	DrawHistory(,4)	SMD North X PPG History
3.8	DrawHistory(,5)	Position, vertex and energy history

Table 3.2: Drawing functions

This table shows which plots are generated with which function in the code of ZDC and SMD (see Chapter 4) online monitoring. In case of SMD figs. 4.6 and 4.7, several similar plots are generated for different the different SMD's and stripe directions, I only included one of these.

that this was a fake event. Some timing correction is still missing in fig. 3.4, as the maximum is very far from zero. This correction was already made for the Au+Au run, so the vertex position is in fig. 3.3 near to zero. ZDC vertex is also compared to BBC vertex on fig. 3.10, the ratio should be near one here.

3.2.3 LED signal monitoring

As we saw already, the energy calibration in ZDC is done via an LED signal. There is a plot for the LED energy values in fig. 3.5, where we can see, if the gain of some channels went bad for example, or if the LED energy changed during a run. This would cause the LED energy plots not to be constant. There are green lines on these plots, which show the values of the energy seen a few days ago. The values at the first ZDC slab on the north side deviate from this green line, because gain for that channel was changed in the meantime.

The timing is monitored as we see in fig. 3.6, this is more constant.

History of LED values for every channel is stored in a database and monitored. Some of these plots for ZDC are shown in fig. 3.7. Values on the horizontal axis are in units of 10^4 seconds. There were in the monitored interval of a few weeks four changes.

3.2.4 Expert plots

It is important to monitor the history of the main values that are measured by the ZDC, to keep track of changes. Because of this I included fig. 3.8 in the online monitoring. On this figure, the first two lines we see the history of the four SMD positions, see Chapter 4.

We have two plots for the energy history, what we see here is a constant energy with rare bad values. The explanation for them could be the same as in the previous paragraph. Interesting is here furthermore the small scattering of the energy values.

The vertex position history seems to have a large scattering, but this just due to the lack of strong deviations and small scales. It is nearly constant in the monitored interval.

With the plots in fig. 3.9 we constantly check, if we have correct values for gain factors in the ZDC slabs. If the gains are correct, the ratio deposited energies in the first and second plus third slab should be equal for north and south side, due to same geometry. Regardless of gain, the shape of the two plots should be and is the same in good runs.

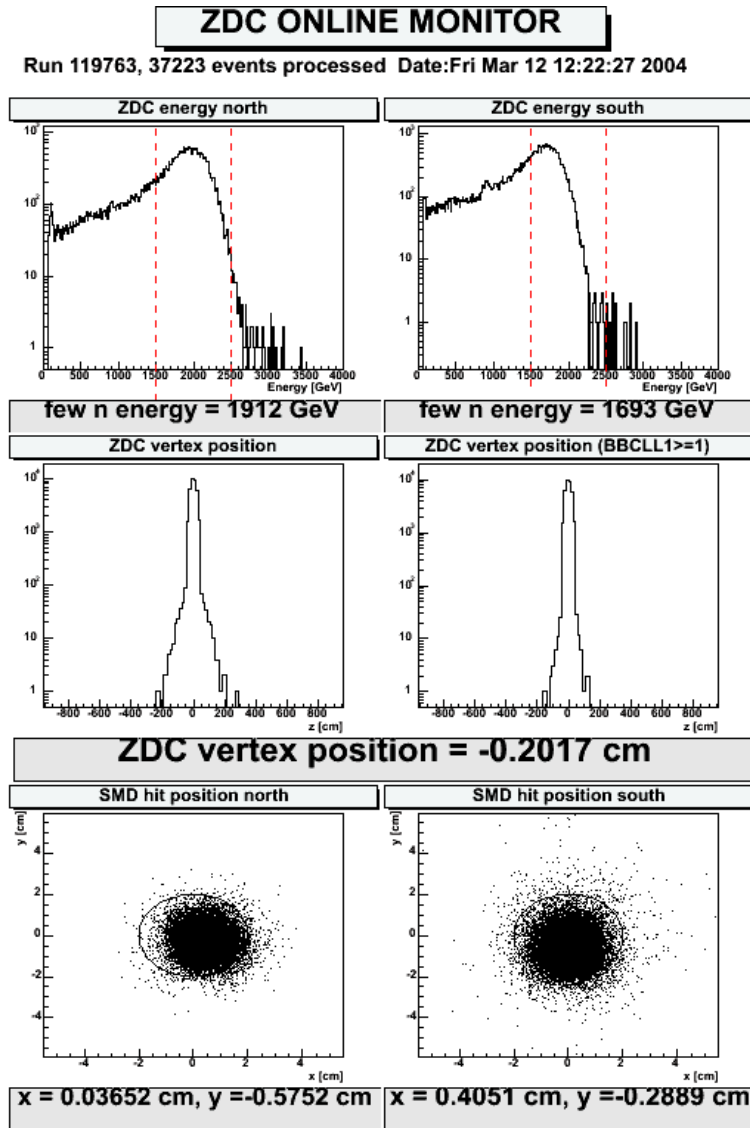


Figure 3.3: ZDC main online monitor in a Au+Au run

This figure shows the ZDC online monitor in a Au+Au run. In the first row, we see the energy distributions in the north and south side calorimeters. The plots in the second row show the vertex position distribution, on the left hand side with a cut made with help of the BBC. In the last row, we see the transverse position distribution measured via the SMD, see Chapter 4. All plots show values within the normal ranges.

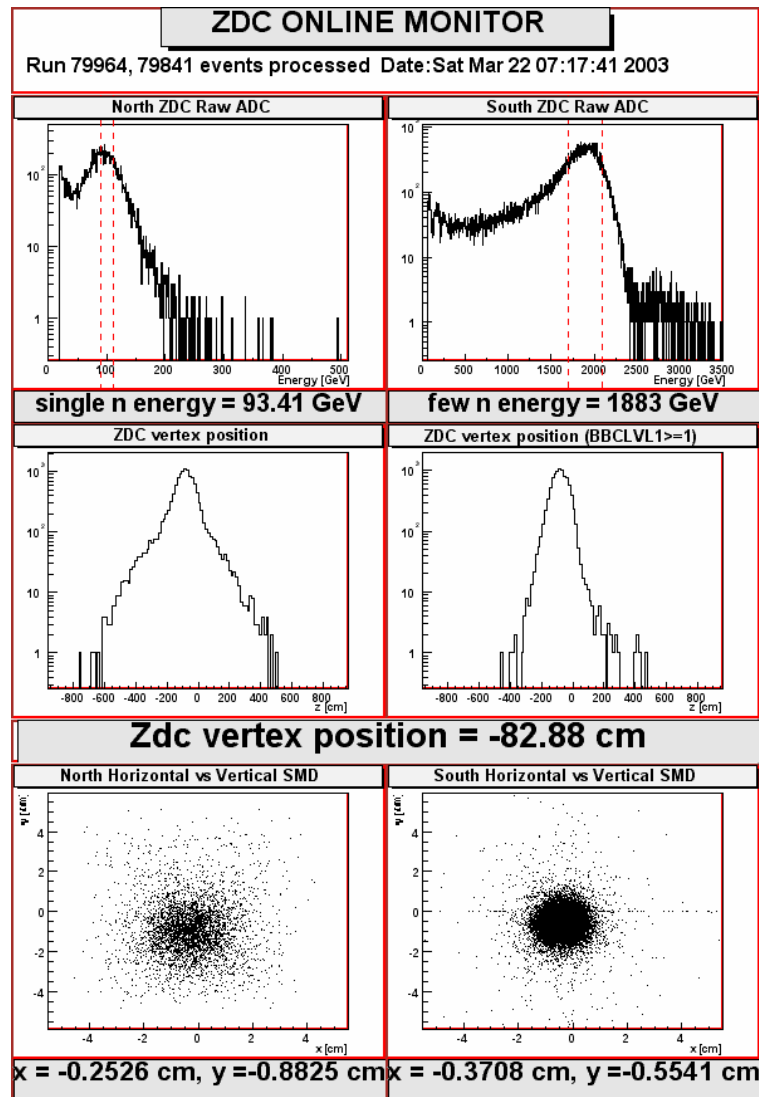


Figure 3.4: ZDC main online monitor in a d+Au run

The plots shown in this figure are similarly arranged as in fig. 3.3. The nominal value of the energy maximum on the deuteron side is smaller here, and the measured value is in the allowed $100 \text{ GeV} \pm 10 \text{ GeV}$ range. An other feature is, that the vertex distribution was broader here and had a maximum shifted towards the south side. Later, the ZDC timing was corrected and then the maximum moved to zero, as in fig. 3.3.

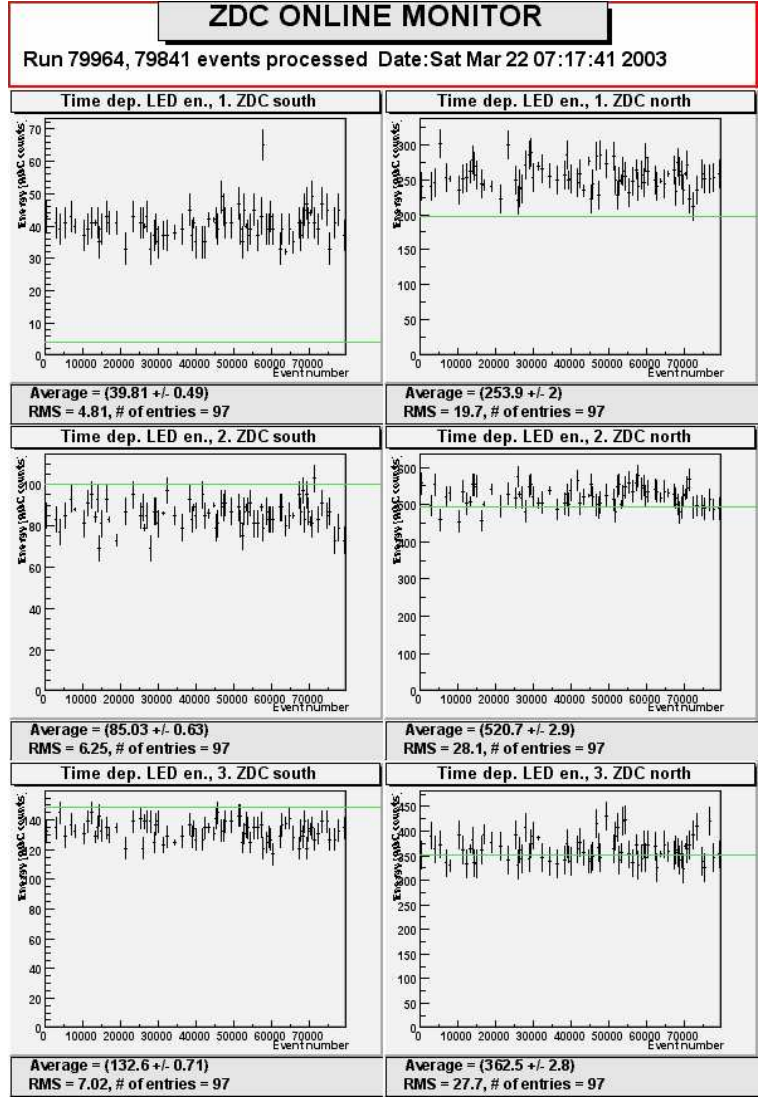


Figure 3.5: LED energy values versus event number

In this set of plots we see the time (event number) dependence of the LED energy. The south side is shown on the right, the north side on the left. The individual rows correspond to the deposited energy measured in the first, second and third ZDC slab, respectively. Green lines represent the average values measured a few days formerly.

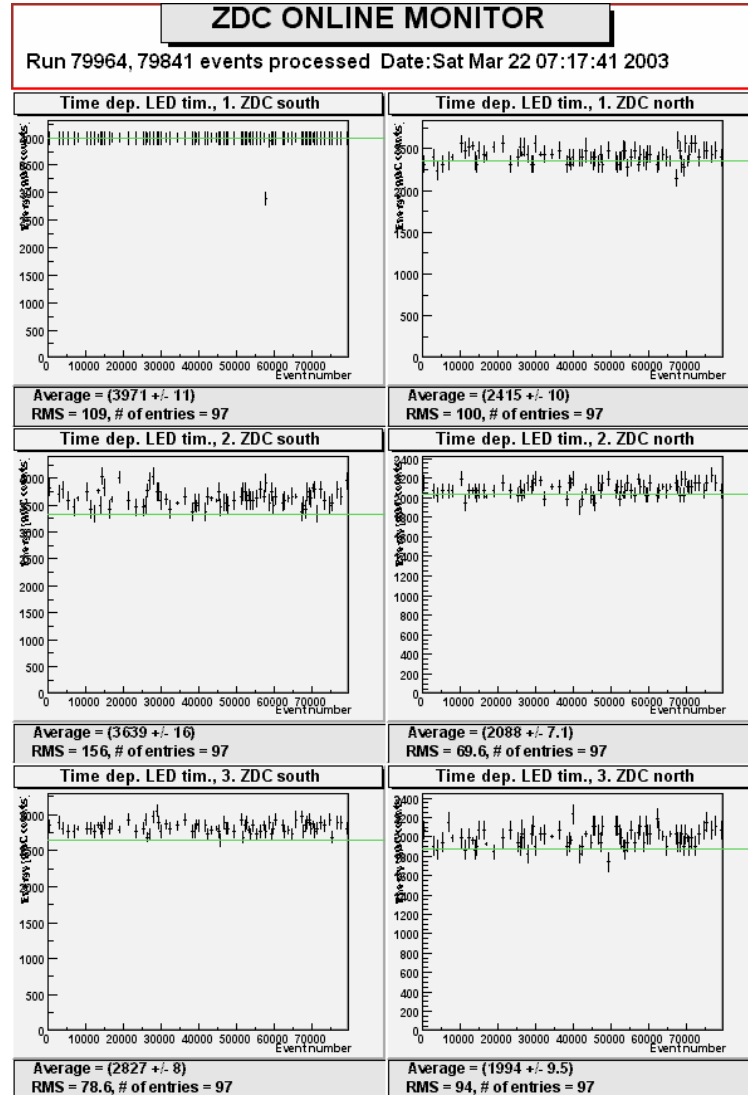


Figure 3.6: LED timing values versus event number

LED timing values are plotted here versus the event number. Arrangement of the plots is the same as in fig. 3.5. There are acceptable random fluctuations, but in the first slab on the south side, all values are in the last bin. Because of this overflow, some corrections on the timing signal had to be made.

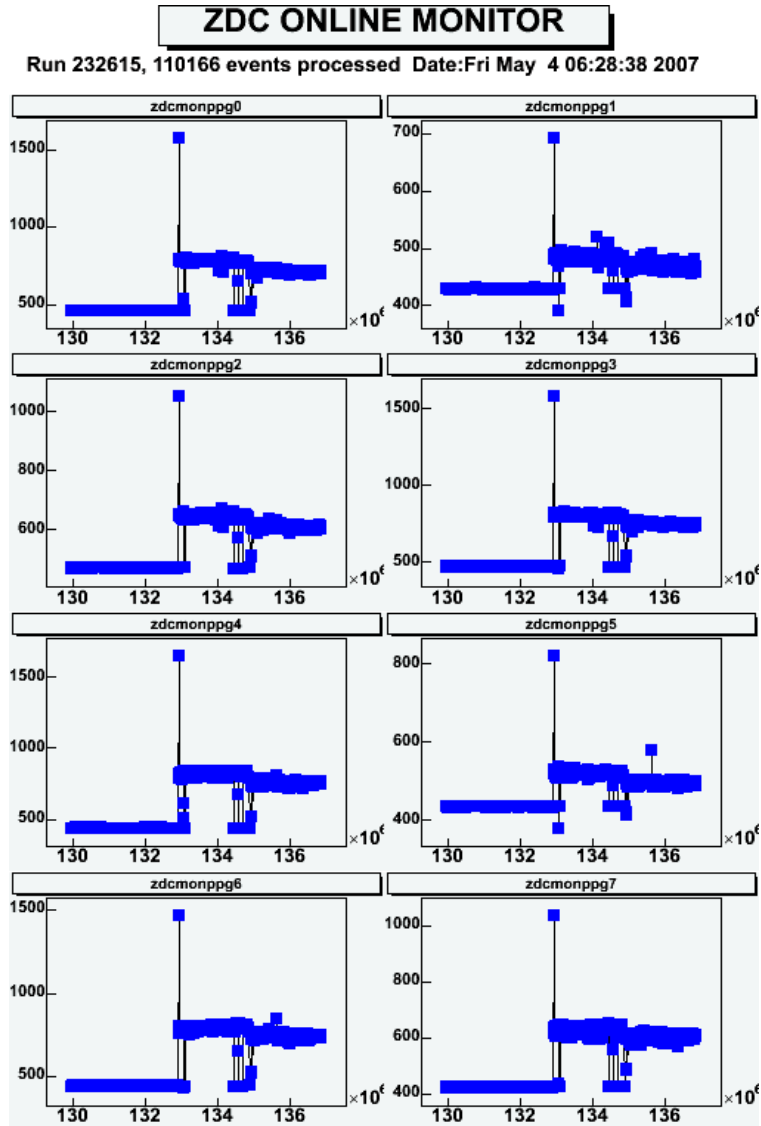


Figure 3.7: Expert plots in a Au+Au run

The average LED energy deposited in the ZDC's is plotted here versus the time of the run in which it was measured. The covered period of time plotted in these figures is around one and a half month. The significant change noticeable on all eight plots (corresponding to the two times three ZDC modules plus the two analog sums) is due to a change in the high voltage setting in our detectors.

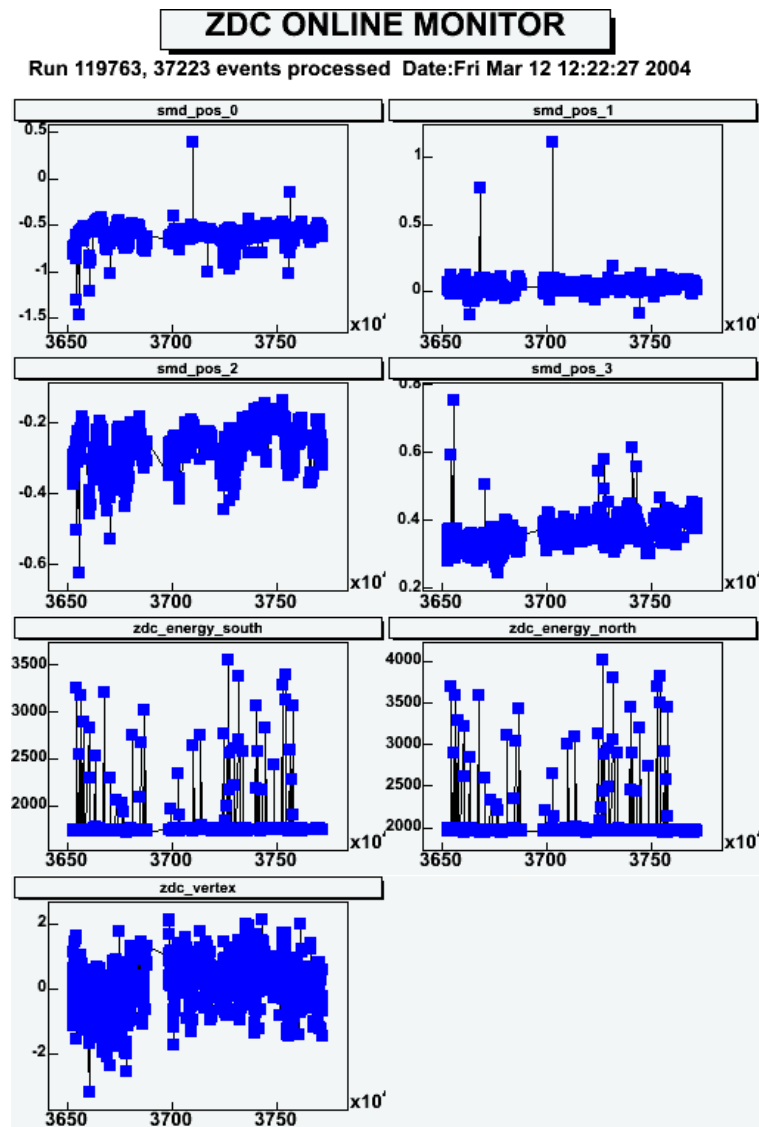


Figure 3.8: Expert plots in a Au+Au run

In the first four figures the history of the position measured in the SMDs is plotted here. After that the average deposited energy in the south and north ZDC is shown. There is a clearly visible constant line at around 2000 GeV, the higher values are caused by runs with low event number, when energy could not have been determined properly. The last plot shows the vertex position history. The covered period of time plotted in these figures is around two weeks.

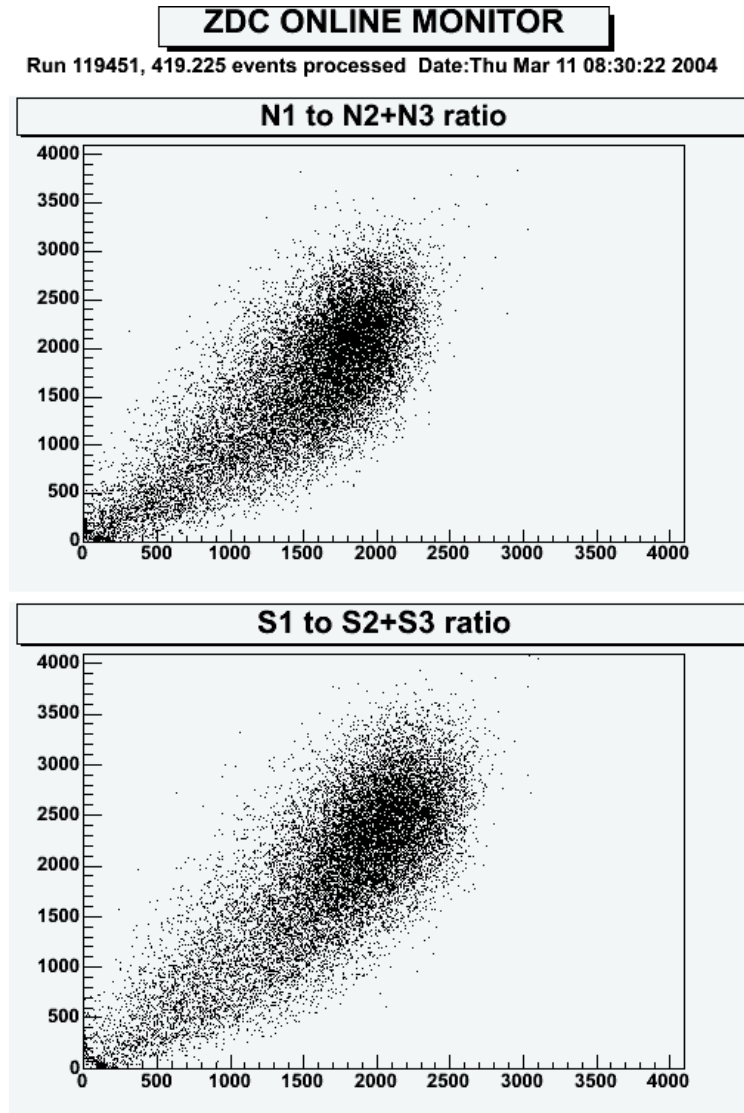


Figure 3.9: Expert plots in a Au+Au run

In the top panel, the correlation between the deposited energies in the first and the second plus third ZDC slab is plotted. The bottom panel shows the same correlation for the south side. The slope of the distributions should be the same for both sides, as it represents the ratio of the gain factors used in the individual ZDC slabs.

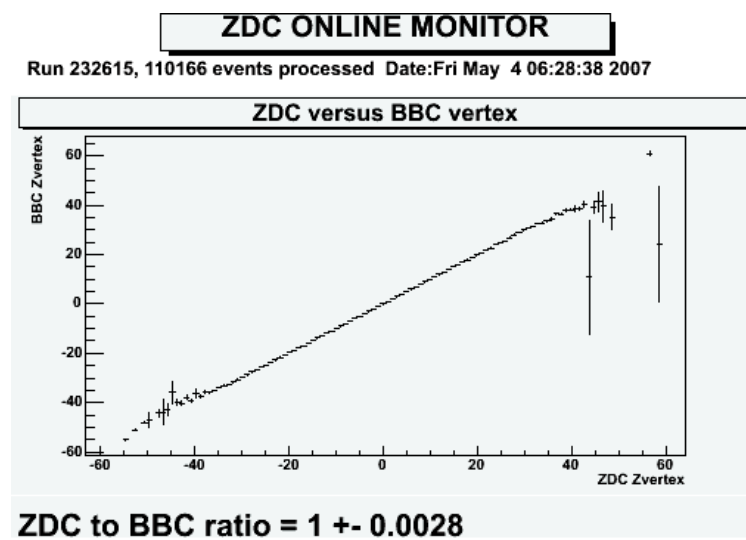


Figure 3.10: ZDC to BBC vertex in a Au+Au run

Vertex calculated from ZDC versus vertex calculated on BBC is shown on this plot. It shows, that vertex position calculated from the BBC and the ZDC were in agreement during the run, so both detectors worked properly.

Chapter 4

An online monitoring system for the Shower Max Detector

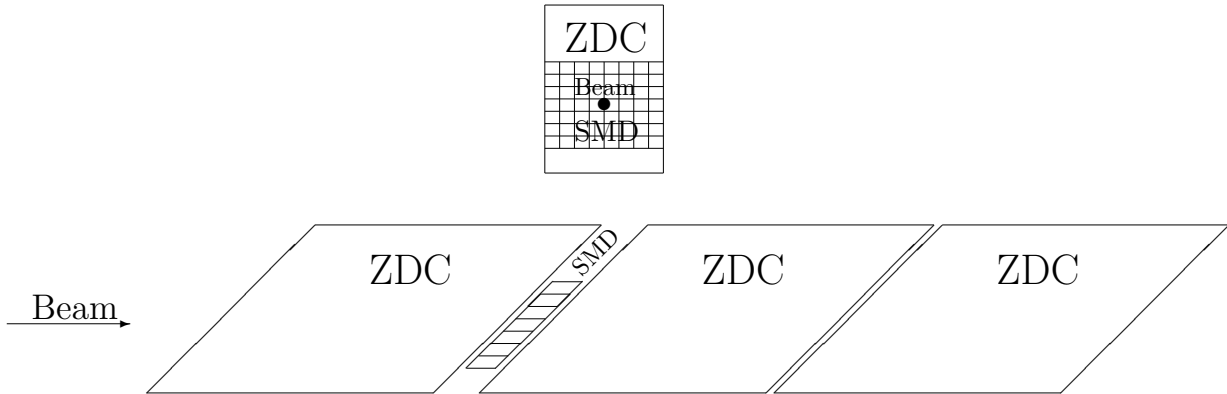


Figure 4.1: Beam and side view of the SMD within the ZDC modules

4.1 The Shower Max Detector

The ZDC's are present at all four experiment of the Relativistic Heavy Ion Collider as they may be considered to be part of RHIC instrumentation also due to their role in beam diagnostics and event characterization. The Shower Maximum Detector (SMD) is an X-Y scintillator strip detector inserted between 1st and 2nd ZDC modules, see fig. 4.1. This location corresponds (approximately) to hadronic shower maximum position. The SMD is to the PHENIX ZDC's among the four RHIC ZDC's.

It is useful for a study of transverse momentum distribution of beam fragmentation products, beam steering and beam profile studies due to beam divergence. The horizontal x coordinate is sampled by 7 scintillator strips of 15 mm width each, while the vertical y coordinate is sampled by 8 strips of 20 mm width each, tilted by 45 degrees. The active area covered by SMD is 105 mm \times 110 mm. The SMD position resolution depends on energy deposited in the scintillator and varies from around 10 mm at small number of charged particles crossing the SMD to values smaller than 3 mm when number of particles exceed 100. For comparison, the spread of neutrons due to Fermi motion is about 2.2 cm at 100 GeV.

As mentioned before, with the SMD we can measure the beam position, if we look at the energy distribution of the shower in the vertical and horizontal strips. I measure the beam position on the following way then:

channel	number
south horizontal strips	8-15
south vertical strips	16-22
south analog sum	23
north horizontal strips	24-31
north vertical strips	32-38
north analog sum	39

Table 4.1: SMD channels

There are 32 SMD channels, seven and eight for the vertical and horizontal strips respectively, and two more for the analog sums.

$$x = \sum_{i=1}^7 \left(\frac{E_i x_i}{\sum E_i} - \frac{x_i}{7} \right), \quad (4.1)$$

$$y = \sum_{i=1}^8 \left(\frac{E_i y_i}{\sum E_i} - \frac{y_i}{8} \right), \quad (4.2)$$

where E_i is the energy deposited in the i th slab and x_i is its position. Fig. 4.2 shows a possible energy distribution. In the formulas the average position of the slabs is subtracted to have the $(x, y) = 0$ position at the physical center of the SMD.

Now, we have the beam energy and position at both the north and south side. It is very important to monitor these to see immediately, if there is a change in these basic quantities.

4.2 The SMD online monitoring

The SMD online monitoring works similarly and is very much connected to the ZDC online monitoring, described in Section 3.2. The drawing functions are summarized in table 3.2.

In this section, I show some plots of the SMD online monitor. The code is available in ref. [21]. The main SMD monitor is the one that measures the transverse distribution of neutrons. The last two plots in figs. 3.3-3.4 show the north and south SMD position distribution. Scattering is bigger in the deuteron case, the hits for the gold beam are relatively more concentrated. In fig. 3.3 there is a circle drawn around the middle, and the maximum

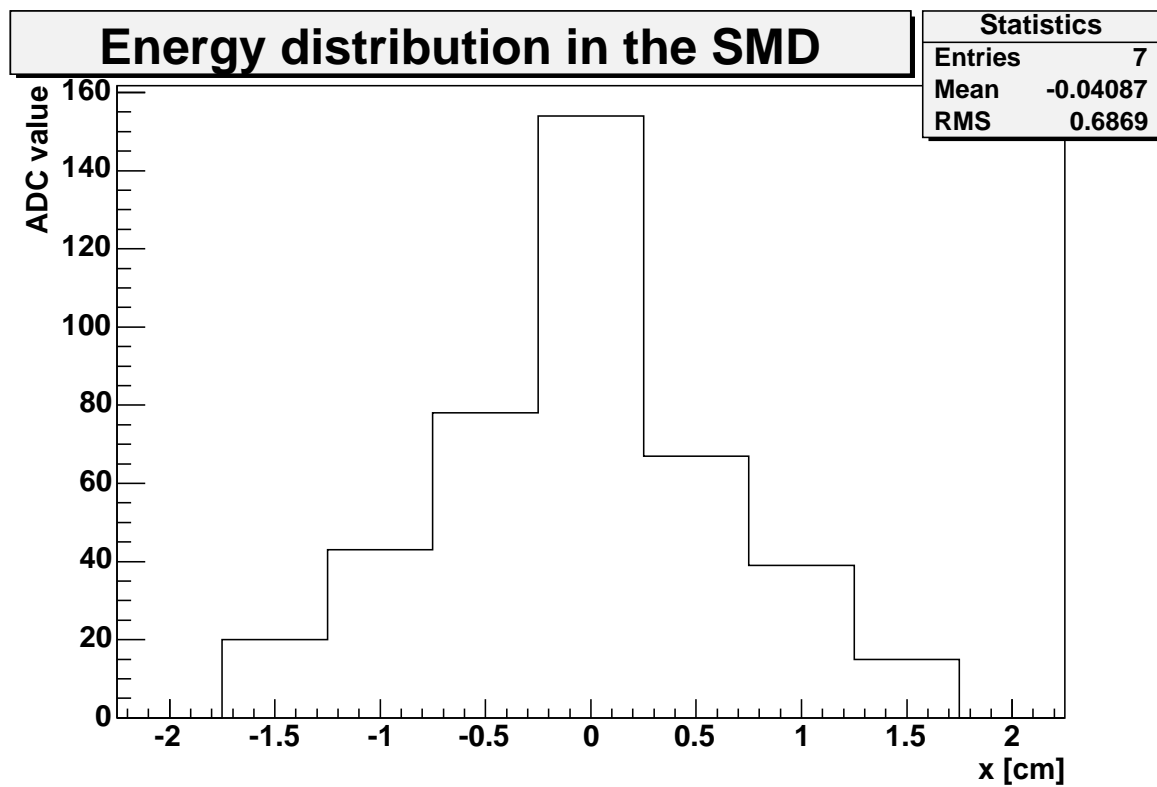


Figure 4.2: SMD energy distribution

In this figure, we see the energy distribution in the horizontal slabs of the north SMD. If we take the average of the positions weighted with the deposited energy, we get the mean position.

of the distribution should be in this circle.

On the main expert plots, in figs. 4.3-4.4, projected transverse beam centroid distributions are shown in one dimension in the SMDs. After that, there are plots to look at the correlations between SMD position and ZDC energy. This is very useful, because if a little peak appears in the ZDC energy distribution, we could possibly see, from which direction this 'noise' comes. The other four plots show the raw ADC distributions for the sum of the SMD channels.

SMD position history is monitored inside of a run as well, these plots are in fig. 4.5. The green lines are at hard-coded values and represent the value seen a few weeks ago. We see, that the south horizontal position did slightly change, the others are pretty constant. The error bars come from the averaging, which is made for 1000 events here also.

The raw ADC values of the SMD channels are included in the online monitoring also, the north channels are shown in fig. 4.6. The smaller histogram is made with a cut in the ZDC energy (eg. here in Au+Au, $E_{ZDC} < 200$ MeV), and it helps testing that cut. If these small histograms start to increase, the cut limit might have to be revised. Furthermore, the location of the peaks in the larger histograms helps to determine gain factors in SMD channels.

History of LED values for every channel is stored in a database. Some of these plots for SMD are shown in fig. 4.7. On fig. 3.8, the first two lines we see the history (from a database) of the four SMD positions. In the monitored time-interval, there were no big changes, we can just see, that in a short interval of around 80000 seconds we had no beam. The strong deviations on these plots are due to averaging problems. I average 1000 events and put their value to the database, but there can be a short period with lots of bad events, or if a run ends before the completion of 1000 events, averaging goes wrong.

4.3 The Vernier scan

Vernier scans are done from time to time in RHIC to diagnose possible beam steering problems. We also use this to be able to calibrate the SMDs. In a vernier scan, the beam position is changed by the main control room stepwise, and we look at our position values, if they give back the motion. We get the positions from the control room as a function of time, and then

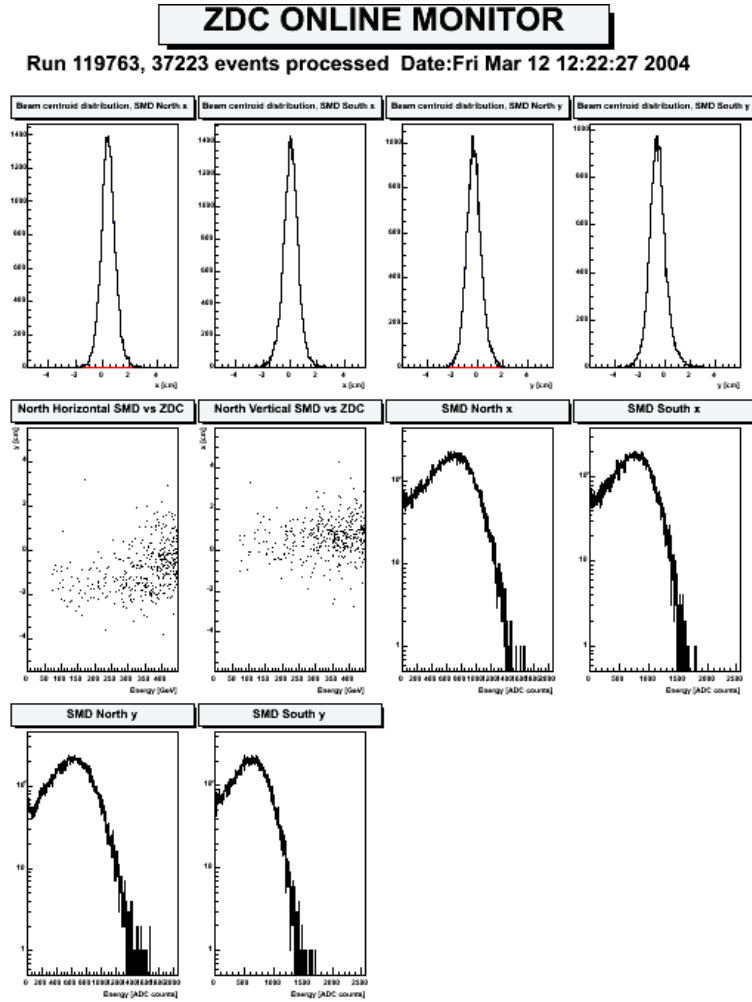


Figure 4.3: Expert plots in a Au+Au run

The first four plots show the beam position distribution in the four (south and north, horizontal and vertical) SMD sets. The first two plots in the second row show the correlation between energy and position, while the in the last plots we see the distribution of the raw ADC signal from the SMDs.

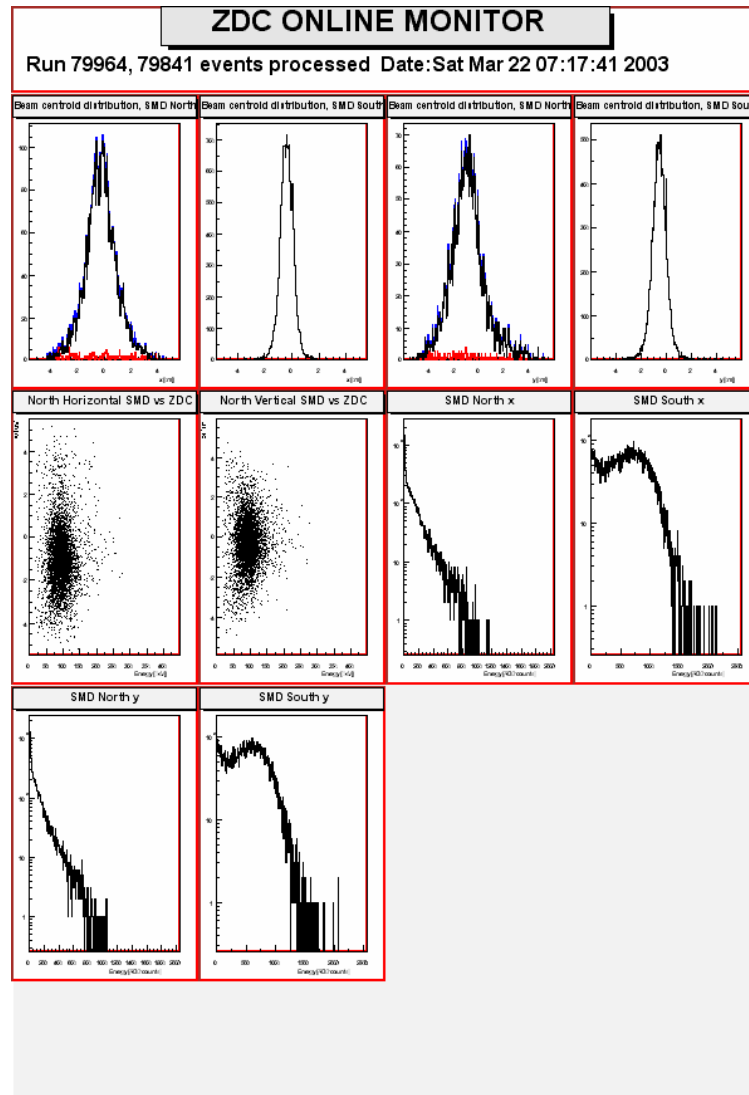


Figure 4.4: Expert plots in a d+Au run

The plots shown here are the same as in fig. 4.3, just in a d+Au run. The south, Au side plots are very similar, but on the north side the energy is smaller, and the scale of the correlation plots was changed also.

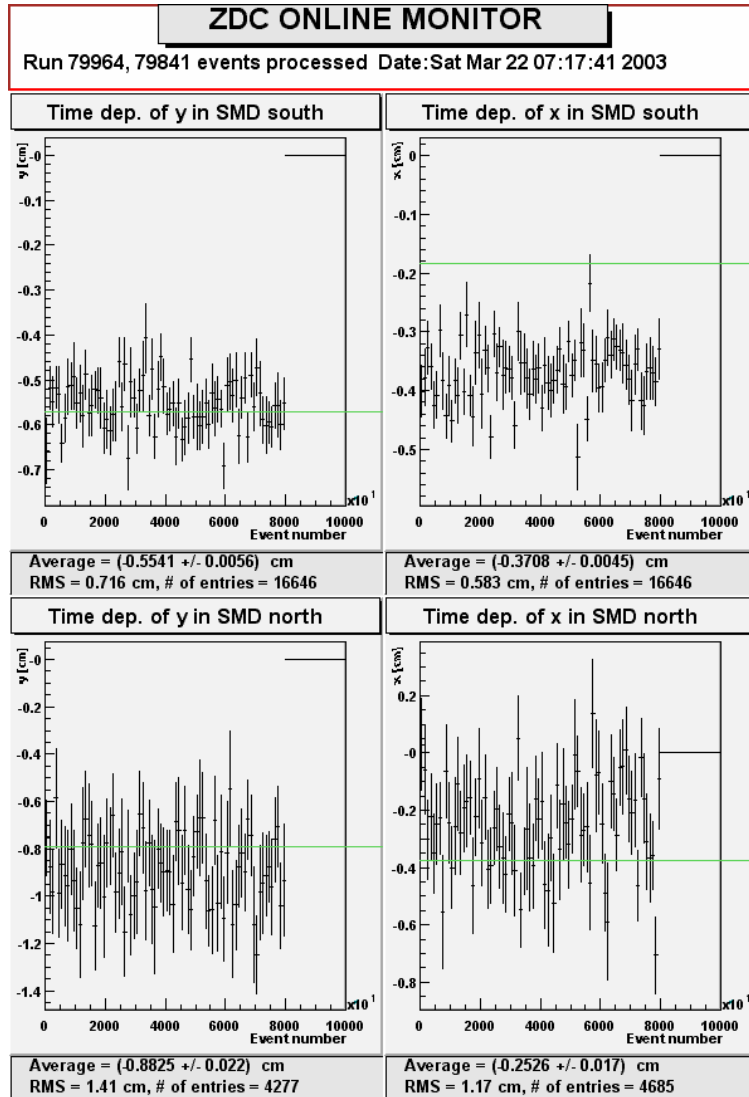


Figure 4.5: SMD position versus event number

Time – event number – dependence of the beam position is shown in these figures. There are large but acceptable random fluctuations in this run.

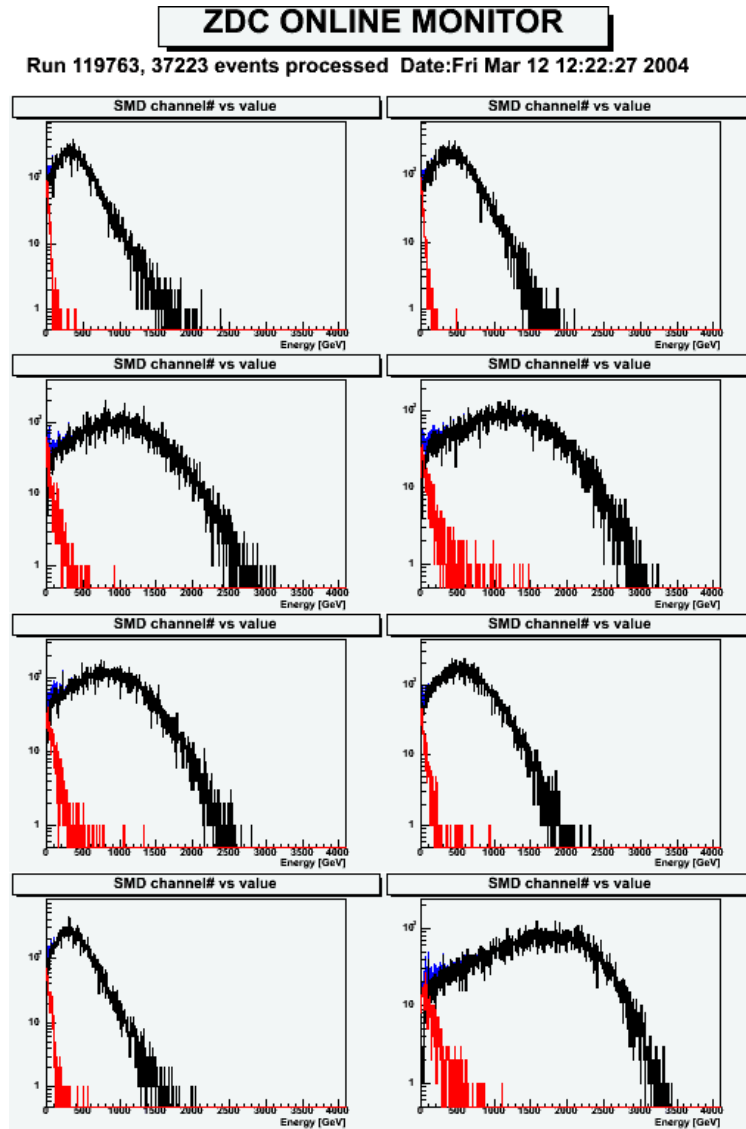


Figure 4.6: Raw ADC value distributions in the north vertical SMD

Distribution of the raw ADC signal coming from north vertical SMDs is shown here. The width of the distribution changes from plot to plot, due to different gains in different photomultipliers. Red curves show the ADC signal only for events with $E_{ZDC} < 200$ MeV.

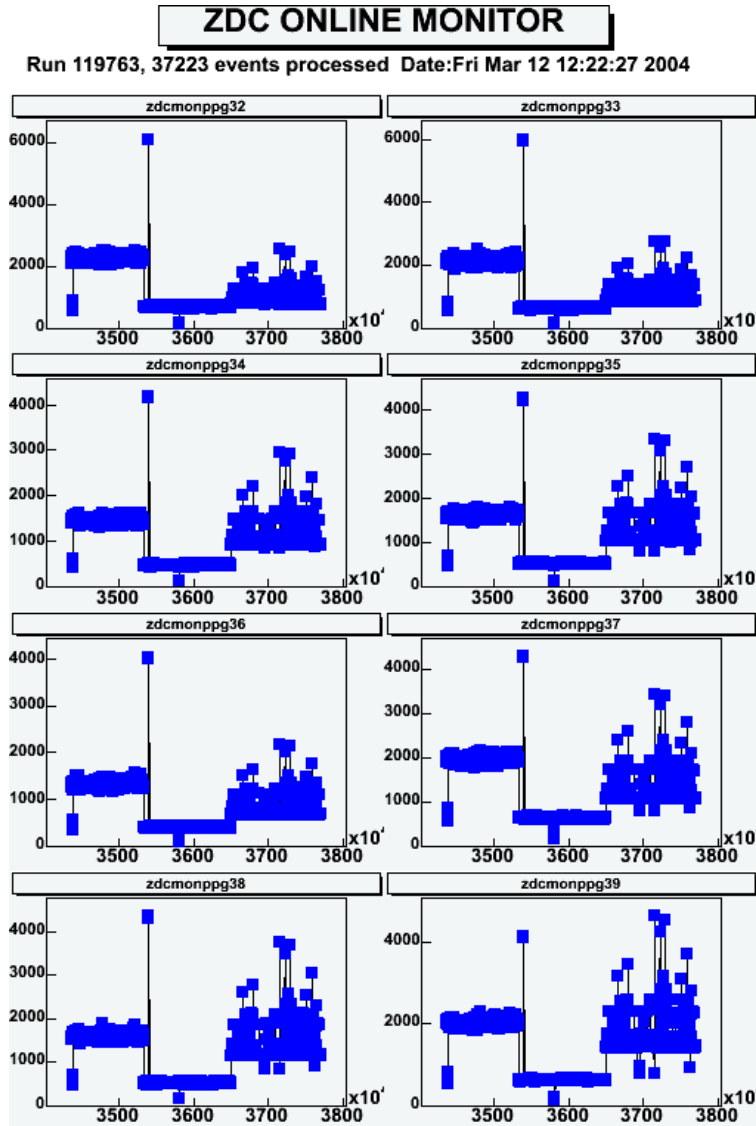


Figure 4.7: LED energy in the SMD stripes in a Au+Au run

The average LED energy deposited in the north vertical SMD stripes is plotted here versus the time of the run in which it was measured, similarly to fig. 3.7. Two significant changes are noticeable on all eight plots corresponding to the eight strips. Both of the shifts are due to a change in the high voltage setting in our detectors. The covered period of time plotted in these figures is around one and a half month.

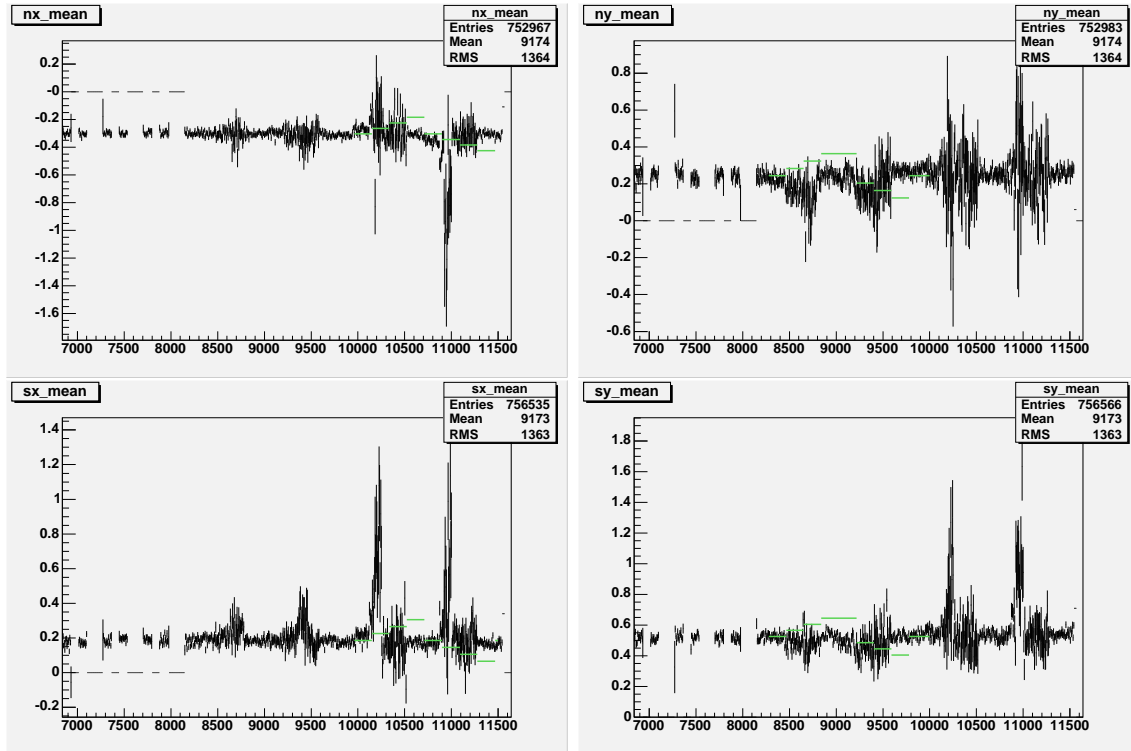


Figure 4.8: Vernier scan plots

Plots of a Vernier scan. Green straight lines show the desired position, while the values with error bars are the monitored positions. The moving is clearly visible while it does not reproduce the beam positions given by the main control room. Further corrections are necessary and the calibration of the detector has to be improved.

compare to the monitored values. This is shown in fig. 4.8.

What we have learned from the plots is that there was a synchronization problem, and we also had to improve the calibration, but the beam movement is well monitored.

Chapter 5

Two- and three-particle correlations at RHIC

5.1 Importance of correlation functions

Correlation functions are important to see the collective properties of particles and space-time structure of the emitting source, eg. the observed size of a system can be measured by two particle Bose-Einstein correlations [22]. From a consistent analysis of two- and three-particle correlations one can establish an experimental measure of thermalization and coherence in the source [23].

The strength of the two-pion Bose-Einstein correlation function λ_* (or simply λ) is found to be sensitive to the partial restoration of $U_A(1)$ symmetry in ultra-relativistic nuclear collisions. An increase in the yield of the η' meson, proposed earlier as a signal of partial $U_A(1)$ restoration, is shown to create a hole in the low p_t region of $\lambda(p_t)$. [24–27].

5.2 Two-particle correlation functions

The two-particle correlation function measures the correlations between particle pairs. It's theoretical definition is:

$$C_2(p_1, p_2) = \frac{N_2(p_1, p_2)}{N_1(p_1)N_1(p_2)} \quad (5.1)$$

where $N_2(p_1, p_2)$ is the two-particle invariant momentum distribution, and $N_1(p)$ is the one-particle spectrum. This can be measured as a function of two momenta, but if there is not enough statistics, we can project it to one dimension: we measure it as a function of

$$q_{\text{inv}} = \sqrt{-(p_1 - p_2)^2}. \quad (5.2)$$

The experimental definition is, when projected to one dimension:

$$C_2(q_{\text{inv}}) = \frac{A(q_{\text{inv}})}{B(q_{\text{inv}})} \quad (5.3)$$

Experimentally, the two particle correlation function is the ratio of the actual and mixed or background pair distributions. The actual pair distribution is

$$A(q_{\text{inv}}) = \int \frac{d^3p_1}{E_1} \frac{d^3p_2}{E_2} \delta_{\Delta q}(q_{\text{inv}} - q_{\text{inv}}(p_1, p_2)) N_2(p_1, p_2) \quad (5.4)$$

and the mixed or background pair distribution is

$$B(q_{\text{inv}}) = \int \frac{d^3p_1}{E_1} \frac{d^3p_2}{E_2} \delta_{\Delta q}(q_{\text{inv}} - q_{\text{inv}}(p_1, p_2)) N_1(p_1)N_1(p_2) \quad (5.5)$$

The $\delta_{\Delta q}$ function is used here in the sense, that it gives one, if the invariant momentum of the pair is in a bin around a given q_{inv} , and zero otherwise.

The momentum distributions are measured, so we have to integrate them in order to get the two-particle correlation function. But if we integrate over the whole momentum-space, we waste a lot of time, as the pair distributions can be computed on a more reasonable way from the data. First, the actual pair distribution can be measured as

$$A(q_{\text{inv}}) = \sum_{\text{events}} \left(\sum_{\text{pairs}} \delta_{\Delta q}(q_{\text{inv}} - q_{\text{inv}}(p_1, p_2)) \right) \quad (5.6)$$

Here, the first sum is on the selected events, and the second on the detected pairs in an event. This way, we get a histogram, which is filled at one q_{inv} value everytime there is a particle pair in an event with this q_{inv} .

This way, we have to sum only on the momentum-pairs, where we have a real particle pair, and before, we summed on all momentum-pairs.

The mixed distribution can be measured similarly, but here we sum on every particle pair, not just on pairs from the same event. This will give a background distribution:

$$B(q_{\text{inv}}) = \sum_{\text{mixed pairs}} \delta_{\Delta q}(q_{\text{inv}} - q_{\text{inv}}(p_1, p_2)) \quad (5.7)$$

We can pre-normalize the correlation function, as we multiply it by the ratio of the integral of the distributions:

$$C_2(q_{\text{inv}}) = \frac{A(q_{\text{inv}})}{B(q_{\text{inv}})} \times \frac{\int B}{\int A} \quad (5.8)$$

5.3 Three-particle correlation function

The theoretical definition is

$$C_3(p_1, p_2, p_3) = \frac{N_3(p_1, p_2, p_3)}{N_1(p_1)N_1(p_2)N_1(p_3)} \quad (5.9)$$

so it is defined through the three- and one-particle invariant momentum distribution.

Again, we have to project it to one dimension with

$$q_3 = \sqrt{-q_{\text{inv},12}^2 - q_{\text{inv},23}^2 - q_{\text{inv},31}^2}, \text{ where} \quad (5.10)$$

$$q_{\text{inv},ij} = \sqrt{-(p_i - p_j)^2}, \quad (5.11)$$

or, one can also project it to three dimensions:

$$C_3(q_{\text{inv},12}, q_{\text{inv},23}, q_{\text{inv},31}). \quad (5.12)$$

Then, the three-particle correlation function can be measured the following way, similarly to the two-particle case:

$$C_3 = \frac{A}{B} \quad (5.13)$$

here, the normalization can be determined from the fit, or the

$$C_3 = \frac{A}{B} \times \frac{\int B}{\int A} \quad (5.14)$$

pre-normalization can be used.

The actual triplet distribution is

$$A(q_{\text{inv},12}, q_{\text{inv},23}, q_{\text{inv},31}) = \int \frac{d^3 p_1}{E_1} \frac{d^3 p_2}{E_2} \frac{d^3 p_3}{E_3} \delta_{\Delta q}(q_{\text{inv},12} - q_{\text{inv},12}(p_1, p_2)) N_3(p_1, p_2, p_3) \quad (5.15)$$

and the mixed triplet distribution is

$$B(q_3) = \int \frac{d^3 p_1}{E_1} \frac{d^3 p_2}{E_2} \frac{d^3 p_3}{E_3} \delta_{\Delta q}(q_3 - q_3(p_1, p_2, p_3)) N_1(p_1) N_1(p_2) N_3(p_3) \quad (5.16)$$

Here we use the one method described in the previous section:

$$A(q_3) = \sum_{\text{events}} \left(\sum_{\text{triplets}} \delta_{\Delta q}(q_3 - q_3(p_1, p_2, p_3)) \right) \quad (5.17)$$

and

$$A(q_3) = \sum_{\text{mixed triplets}} \delta_{\Delta q}(q_3 - q_3(p_1, p_2, p_3)) \quad (5.18)$$

5.4 Dataset

We studied 70M $\sqrt{s_{\text{NN}}} = 200$ GeV RHIC Au+Au collisions recorded at PHENIX during Run 4. Charged tracks were detected by the Drift Chamber and Pad Chambers. The Time Of Flight detector and the Electromagnetic Calorimeters were used to identify π^+ particles, and we had 200M π^+ 's, 900M π^+ pairs and more than 4G π^+ triplets in this analysis. We measured from this data sample the two-pion correlation function C_2 as a function of $q_{\text{inv}} = \sqrt{(k_1 - k_2)^2}$ and the three-pion correlation function C_3 as a function of q_{inv} of the three pairs in the triplet, q_{12}, q_{23}, q_{31} .

5.5 Correcting for the Coulomb interaction

Due to Coulomb-interaction charged particles repulse each other, thus identical sign charged particle pairs will have a larger momentum-difference, and there will be fewer pairs at lower relative momenta. Because of this, there will be a 'Coulomb-hole' in the raw correlation functions. To treat this effect and to get more accurately the 'pure' Bose-Einstein correlations one has to correct for the Coulomb-correction.

5.5.1 Definition and calculation the Coulomb-correction

This correction works as follows for the two-particle case. The basic equation, which connects the two-particle correlation function and the two-particle source function, is

$$C(q) = \int d^3r_{12} S(r_{12}) |\Phi_C(r_{12}, q)|^2, \quad (5.19)$$

with q being the momentum difference of the two particles (more precisely $q = 2k_{12}$), $C(q)$ the ("raw") two-particle correlation function r_{12} the three-vector of relative spatial coordinates, Φ_C the wave-function of the two particles, including the Coulomb-effect. Finally, $S(r_{12})$ is the two-particle source function, defined via the single particle source function $S_1(r)$,

$$S(r_{12}) = \int d^3R S_1\left(R + \frac{r_{12}}{2}\right) S_1\left(R - \frac{r_{12}}{2}\right), \quad (5.20)$$

where R is the three-vector of the average spatial coordinates.

The ("pure") Bose-Einstein correlation function (the Coulomb-corrected correlation function), which we would like to determine experimentally to study the Bose-Einstein type of correlations of a system, would then be:

$$C_0(q) = \int d^3r_{12} S(r_{12}) |\Phi_0(r_{12}, q)|^2, \quad (5.21)$$

where everything is the same as in eq. 5.19, just instead of Φ_C , we use Φ_0 , which is the two-particle planewave-function, ie their outgoing wave-function without Coulomb interaction (it is valid for the case when final state interactions are negligible), calculable as:

$$\Phi_0(r_{12}, q) = \frac{1}{\sqrt{2}} (e^{ik_{12}r_{12}} + e^{-ik_{12}r_{12}}). \quad (5.22)$$

Note that $k_{12} = q/2$ appears in it, and it depends on r_{12} , q and the angle between r_{12} and q , similarly to Φ_C . With this and the definition of C_0 (eq. 5.21) we can explicitly calculate C_0

from S (see ref. [28]):

$$C_0(q) = 1 + \frac{|\tilde{S}(q)|^2}{|\tilde{S}(0)|^2}, \quad (5.23)$$

where $\tilde{S}(q)$ is the Fourier-transform of $S(r_{12})$.

From eqs. 5.19-5.21 we get a connection between the Coulomb-corrected and the “raw” correlation function:

$$C(q) = \frac{\int d^3r_{12} S(r_{12}) |\Phi_C(r_{12}, q)|^2}{\int d^3r_{12} S(r_{12}) |\Phi_0(r_{12}, q)|^2} \times C_0(q). \quad (5.24)$$

Thus we get a Coulomb-correction factor of:

$$K_{\text{Coulomb},2}(q) = \frac{\int d^3r_{12} S(r_{12}) |\Phi_C(r_{12}, q)|^2}{\int d^3r_{12} S(r_{12}) |\Phi_0(r_{12}, q)|^2} \quad (5.25)$$

We use basically the same technique in the three-particle case, and there we get the following factor:

$$K_{\text{Coulomb},3}(k_{12}, k_{23}) = \frac{\int d^3r_{12} d^3r_{23} S(r_{12}, r_{23}) |\Phi_C(r_{12}, r_{23}, k_{12}, k_{23})|^2}{\int d^3r_{12} d^3r_{23} S(r_{12}, r_{23}) |\Phi_0(r_{12}, r_{23}, k_{12}, k_{23})|^2}, \quad (5.26)$$

with a generalized r_{ij} and k_{ij} , the relative momentum and coordinate of each pair of a triplet (the third one with the indices 31 is already given if we know the ones with 12 and 23).

The multiparticle wavefunction can be calculated with a method detailed in ref. [28]. This method is based on a solution of the two-body Coulomb-problem that is symmetrized to approximate the (for $n = 3$ analytically not yet resolved) n -body Coulomb-problem ($n=2$ or 3 in our case).

5.5.2 Application of the Coulomb-correction

In eqs. 5.25-5.26 we see, that the Coulomb-correction depends on the source function, and the source function can only be calculated from the correlation function, thus a method to determine the Coulomb-correction would be to (numerically) invert the integral equation of eq. 5.19, but this is very complicated, furthermore we would get correlated errors on the datapoints in the measured source function.

A simpler method is to use the following iterative method. Assume a (parametrical) source function shape, from which (using eq. 5.21) one can calculate the Coulomb-corrected

correlation function analytically. Then one just assumes some input parameters from the source function, calculates the Coulomb-correction with that, then divides the measured raw correlation function with it. This gives a zeroth order correlation function. This then one fits with the analytical correlation function and determines a new set of parameters. With these parameters one then calculates the source function and a new Coulomb-correction etc:

- Set source parameters to some initial value
- Compute the Coulomb-correction with current source parameters
- Correct the correlation function with this Coulomb-correction
- Obtain new source parameters from the fit

The fix point of this iteration process is at the right values of the source parameters. Although this method is obviously not model-independent, it has an advantage: the statistical error of the last fit gives the final statistical error properly.

It is important that the Coulomb-correction has an error, which has to be propagated into the error of the corrected data points. This error comes mostly from the multi-dimensional integrations (that have to be carried out using Monte-Carlo techniques), and is point-to-point fluctuating. This error was estimated (from the fluctuations of the Coulomb-correction) to be 0.5% in case of the two-particle Coulomb-correction, and 8% in the three-particle case.

5.6 The effect of resonances on correlations

To take into account the effect of resonances, one can utilize the core-halo picture [23, 29], and characterize the system with a hydrodynamically evolving core and a halo of the decay products of the long-lived resonances. For the Coulomb-correction we assume the same parametric shape for both source parts, eg a Gaussian, just the halo source has to be much broader than the core source, because it consists of the decay product of the long lived resonances. Large relative radii correspond to very small momentum differences in case of correlation functions, for example, distances of 50 fm correspond to 4 MeV/ c in momentum. Whereas resolution in PHENIX is above 5MeV/ c , thus the halo effects in the correlation functions are below the experimental momentum resolution. Hence one has to assume a halo width much bigger than the core width, $R_h \gg R_c$. Role of this unresolvable parameter R_h was investigated in present analysis, by taking $R_h \rightarrow \infty$, but its actual value did not

change the results significantly.

In this section, we shall describe the core-halo model, as it is a basic assumption about the particle emitting source present in high energy heavy ion collisions [23, 29].

5.6.1 Basic definitions

The central assumption of the core/halo model is that the reduction of the strength of the n -particle Bose-Einstein correlation functions (how they differ at zero relative momenta from the theoretical value of two) is due only to the presence of the long-lived resonances [30].

The emission function of the whole source can be written as a sum of a contribution from the core and from the halo, where halo stands for the decay products of the (unresolvable) long-lived resonances. The core is indexed with (c), the halo is by (h):

$$S(x, k) = S_c(x, p) + S_h(x, p). \quad (5.27)$$

We furthermore assume, that some fraction of the core emits particles in a coherent manner (e.g. due to emerging formation of pion lasers or Bose-Einstein condensates of pions), so we define

$$S_c(x, p) = S_c^p(x, p) + S_c^i(x, p) \quad (5.28)$$

where the upper index p stands for coherent component (p as partially coherent), upper index i stands for incoherent component of the source.

The one-particle invariant spectrum is then given by

$$N(p) = \int d^4x S(x, p) = N_c(p) + N_h(p) \quad (5.29)$$

and the core contribution is a sum of the coherent and incoherent components:

$$N_c(p) = \int d^4x S_c(x, p) = N_c^p(p) + N_c^i(p) \quad (5.30)$$

One can introduce the momentum dependent core fractions $f_c(p)$ and partially coherent core fractions $p_c(p)$ as

$$f_c(p) = N_c(p)/N(p) \quad (5.31)$$

$$p_c(p) = N_c^p(p)/N_c(p) \quad (5.32)$$

The halo and the incoherent fractions f_h, f_i are

$$f_h(p) = N_h(p)/N(p) = 1 - f_c(p) \quad (5.33)$$

$$f_i(p) = N_c^i(p)/N_c(p) = 1 - p_c(p) \quad (5.34)$$

5.6.2 The strength of the n -particle correlations

We define the n -particle correlation function as

$$C_n(p_1, p_2, \dots, p_n) = \frac{N_n(p_1, p_2, \dots, p_n)}{N_1(p_1)N_1(p_2) \cdots N_1(p_n)}. \quad (5.35)$$

We find [23] that the strength of the n -particle correlation function (extrapolated from finite relative momenta to zero relative momentum) is given by the following formula,

$$C_n(p_i = p_j, \forall(i, j)) = 1 + \lambda_{*,n} = 1 + \sum_{j=2}^n \binom{n}{j} \alpha_j f_c^j [(1 - p_c)^j + j p_c (1 - p_c)^{j-1}], \quad (5.36)$$

where α_j counts the number of fully mixing permutations of j elements. This can be calculated from a simple recurrence, as obtained in ref. [30]: There are exactly $\binom{n}{j}$ different ways to choose j different elements from among n different elements. Since all the $n!$ permutations can be written as a sum over the fully mixing permutations, the counting rule yields a recurrence relation for α_j , ref. [30]:

$$\alpha_n = n! - 1 - \sum_{j=1}^{n-1} \binom{n}{j} \alpha_j. \quad (5.37)$$

The first few values of α_j are then $\alpha_1 = 0$, $\alpha_2 = 1$, $\alpha_3 = 2$ and $\alpha_4 = 9$.

From this, we have the following explicit expressions for the first few intercept parameters:

$$\lambda_{*,2} = f_c^2[(1 - p_c)^2 + 2p_c(1 - p_c)] \quad (5.38)$$

$$\begin{aligned} \lambda_{*,3} &= 3f_c^2[(1 - p_c)^2 + 2p_c(1 - p_c)] \\ &+ 2f_c^3[(1 - p_c)^3 + 3p_c(1 - p_c)^2] \end{aligned} \quad (5.39)$$

$$\begin{aligned} \lambda_{*,4} &= 6f_c^2[(1 - p_c)^2 + 2p_c(1 - p_c)] \\ &+ 8f_c^3[(1 - p_c)^3 + 3p_c(1 - p_c)^2] \\ &+ 9f_c^4[(1 - p_c)^4 + 4p_c(1 - p_c)^3] \end{aligned} \quad (5.40)$$

In the above equations, the effective intercept parameters, the core fraction and the partially coherent fraction are evaluated at a mean momentum p , $\lambda_{*,n} = \lambda_{*,n}(p)$, $f_c = f_c(p)$ and $p_c = p_c(p)$.

5.7 Partial coherence and core fraction of the source

Let us consider the definition of f_c (core fraction) and p_c (partial coherent fraction of the core) defined in eqs. 5.31-5.32 and the core-halo model result for λ_2 and λ_3 of eqs. 5.38-5.39.

We thus get from eq. 5.36

$$C_2(p_1 = p_2) = 1 + \lambda_2, \text{ and} \quad (5.41)$$

$$C_3(p_1 = p_2 = p_3) = 1 + \lambda_3. \quad (5.42)$$

To calculate the allowed f_c , p_c region, one has to determine λ_2 and λ_3 . In order to determine λ_2 and λ_3 we have to extrapolate the correlation functions back to zero relative momenta. To do that, we fitted two- and three-particle correlation functions for $0.2 < p_t < 2.0$ GeV/ c and $0 - 92\%$ centrality, using the invariant momentum difference $q \equiv q_{\text{inv}}$ as variable and the following shapes (in $\hbar c = 1$ units):

$$\text{Gauss: } C_2(q) = 1 + \lambda \exp(-|Rq|^2) \quad (5.43)$$

$$\text{Levy: } C_2(q) = 1 + \lambda \exp(-|Rq|^\alpha) \quad (5.44)$$

$$\text{Edgeworth: } C_2(q) = 1 + \lambda \exp(-|Rq|^2) \left(1 + \frac{\kappa_3}{3!} H_3(\sqrt{2}|Rq|)\right), \quad (5.45)$$

where R is the HBT (Bose-Einstein) radius of the source (or, in more dimensions the HBT radii), H_3 is the third Hermite polynomial, and κ_3 it's coefficient (the Edgeworth form is a model-independent expansion [31], of which we keep only the first term, to measure deviation from the Gauss form). We fitted only those points with $q_{\text{inv}} > 0.02$ GeV/ c due to a non-BEC and non-Coulomb structure seen at low q_{inv} (see the gray lines on fig. 5.1).

Here only the Levy fits had acceptable confidence levels, the Gauss and Edgeworth fits did not. These and the Coulomb-corrected correlation functions are shown on fig. 5.1. The three-dimensional C_3 was projected onto the $q_{12} = q_{23} = q_{31}$ line.

From these fits we determined λ_2 and λ_3 , and calculated the allowed f_c vs p_c region, using the 3σ contours from eqs. 5.41-5.42, see fig. 5.2. The size of the region obtained from C_3 is much larger due to the smaller number of triplets compared to pairs.

Compared to former NA44 analysis (see refs. [23, 32, 33]), the resulting allowed region is at a little bit higher f_c values, but note, that we calculated the parameters using Levy fits and not Gaussian ones. Also note, that the center-of-mass collision energy is much higher at RHIC than at SPS.

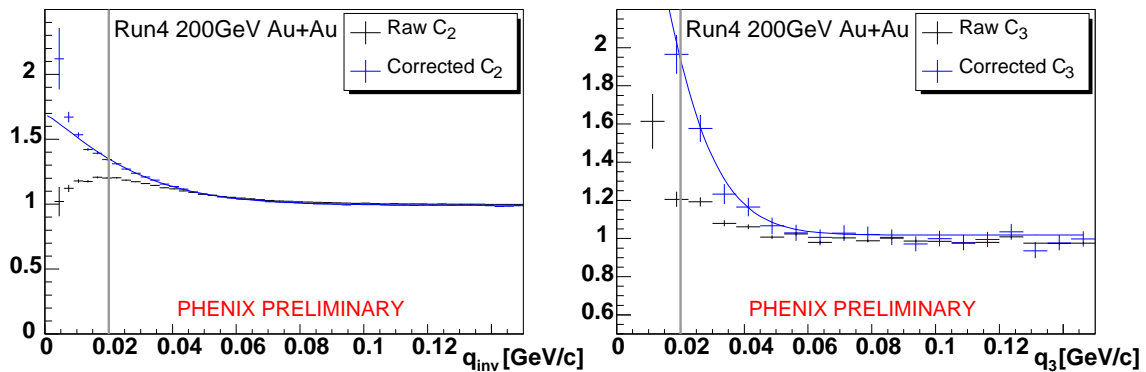


Figure 5.1: Raw- and Coulomb-corrected correlation functions

Raw- and Coulomb-corrected two- and three-particle correlation functions are shown for $0.2 < p_t < 2.0$ GeV/ c and 0 – 92% centrality with Levy fits. Points with $q_{inv} < 0.02$ GeV/ c were excluded from the fits.

5.8 The strength of two-particle correlations

In the second part of the analysis, we have analyzed two-pion correlation functions in 10 p_t bins from 0.2 GeV/ c to 0.5 GeV/ c with 0 – 92% centrality by fitting them with the above Gauss, Levy and Edgeworth shapes.

The parameters as a function of average transverse mass ($\lambda(m_t)$, $R(m_t)$, $\alpha(m_t)$ and $\kappa_3(m_t)$) for Gauss, Levy and Edgeworth fits are shown on fig. 5.3. The α parameter of the Levy distribution controls the long-range source in a similar way as the λ parameter, so fitting both makes the fit underconstrained. Hence we did fits also with fixed α , and for comparison, also with fixed κ_3 . These latter fits show the same $\lambda(m_t)$ behavior as in the Gaussian case.

The m_t dependence of λ can be used to extract information on the mass-reduction of the η' meson, a signal of the $U_A(1)$ symmetry restoration in hot and dense matter: It is known [25], that if the chiral $U_A(1)$ symmetry is restored, then the mass of the η' boson (the ninth Goldstone-boson) is tremendously decreasing and its production cross section tremendously increasing. Thus η' bosons are copiously produced, and decaying through η bosons (with a very long lifetime) into low momentum pions. Hence the strength of the two-particle correlation functions at low relative momenta might change significantly. [24].

A comparison of the measurements of fig. 5.3 with model calculations of ref. [24] using Fritiof results for the composition of the long-lived resonances and a variation of the η' mass

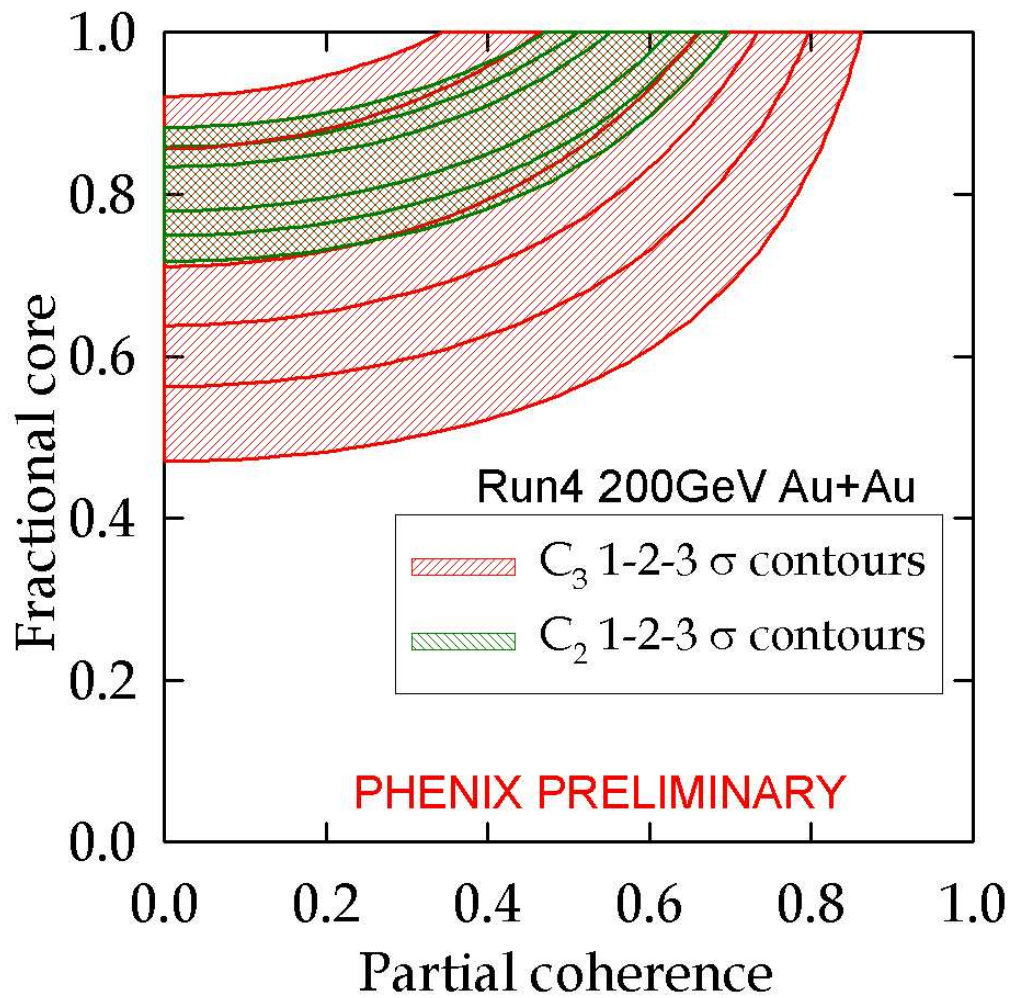


Figure 5.2: Partial coherence versus core fraction

Allowed region of partial coherence versus core fraction extracted from Levy fits is shown on this plot. Contours obtained from C_3 are much larger due to smaller statistics of π^+ triplets compared to π^+ pairs.

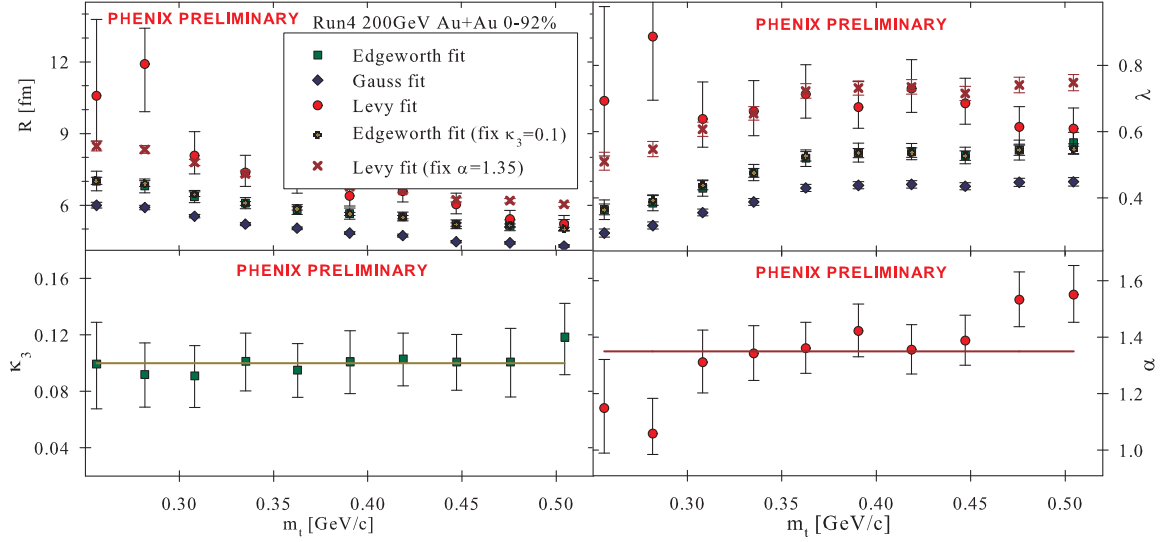


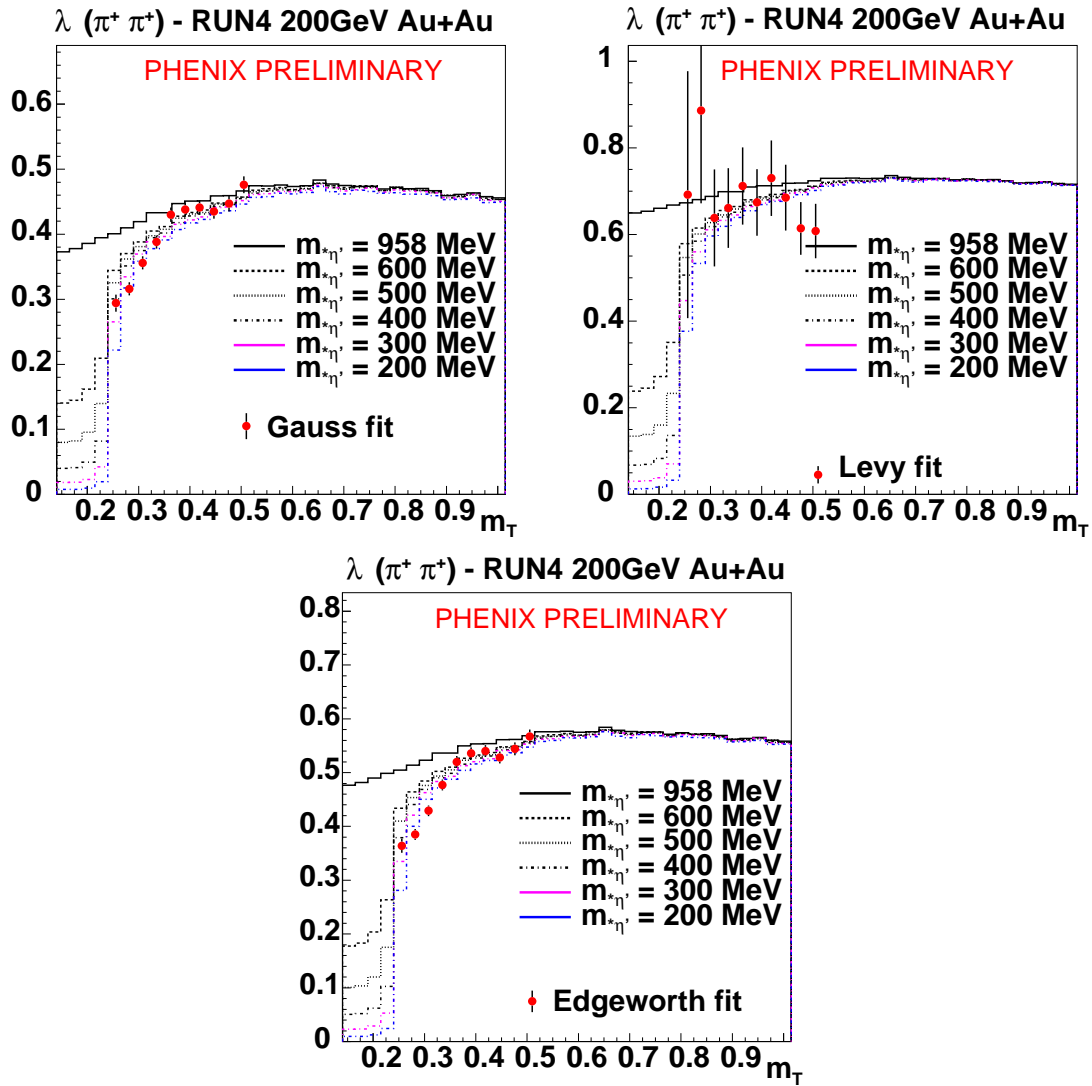
Figure 5.3: $\lambda(m_t)$, $R(m_t)$, $\alpha(m_t)$ and $\kappa_3(m_t)$ from Gauss, Levy and Edgeworth fits

is presented in fig. 5.4.

5.9 Results summary

From simultaneous analysis of two- and three-pion correlations we obtained an allowed region of partial coherence versus core fraction. Nonzero partial coherence is allowed when having larger core size, at total incoherence ($p_c = 0$) the core fraction is slightly higher than previous analysis using Gaussian fits (see refs. [23, 32–34]). This is due to the fact that we used Levy fits, the only investigated one that gave acceptable confidence levels.

We also analyzed the m_t dependence of the λ parameter obtained from various fits. Gauss fit results agree with former PHENIX measurements (see ref. [34]). Regarding $U_A(1)$ symmetry restoration, we conclude that at present, results are critically dependent on our understanding of statistical and systematic errors, and additional analysis is required to make a definitive statement.

Figure 5.4: Mass modification of η'

Measured $\lambda(m_t)$ from different fits compared to calculations using the model of ref. [24] with various η' mass values, and the Fritiof results for the composition of the long-lived resonances.

Chapter 6

Two-particle source functions at RHIC

6.1 Power law tails in Au+Au collisions at RHIC

The observed long power-law tail of two-particle source functions at RHIC PHENIX [35] indicates non-Gaussian probability distributions in the emission processes. In second order phase transitions the basic observables to characterize processes are critical exponents. One of these exponents characterizes the spatial distribution of the order parameter, traditionally denoted by η . It is known [36], that this exponent can be measured by looking at two-particle correlation functions. One can show, that $\eta=\alpha$, where α is the Lévy-stability index of two-particle correlation functions. It is known furthermore [37], that the universality class of QCD at the critical point is the same as the one of 3d Ising models. The exponent of the correlation function is very small in these models, $\eta = 0.03\pm 0.01$. In high energy heavy-ion collisions however random fields can be present, which change the universality class and increase η . These are the random field Ising models, which have $\eta(=\alpha) = 0.50 \pm 0.05$.

This is why it's worthwhile to determine the power-law exponent of the source tail. The value could be obtained from a simple fit to the source functions obtained via imaging, but the errors of the source function are correlated, hence the errors of the fit parameters will not represent the data. We modelled the source function with Lévy distribution [31], because a generalization of the Central Limit Theorem suggests this. We will briefly recall the properties of these distributions [31] and show their application to the data of [35]. Note furthermore, that Coulomb-correction of the correlation functions was done similarly to the method showed in Chapter 5, but here the below described Lévy-type source functions were used in that method.

6.2 Assumption for the source function

The Central Limit Theorem says that if we have many independent statistical variables, and the probability distribution of these variables possess finite variance, then the (somehow normalized) distribution of the sum of these variables (in the limiting case of infinitely many variables) will be Gaussian. This is the reason why we encounter Gaussian distributions in so many cases in the nature. A generalization of this theorem says that if the independent variables as before don't necessarily have finite variance, then the limiting distribution will be one of the Lévy-stable distributions, which in case of symmetric and centered Lévy

distributions are characterized by two parameters: the so called Lévy-exponent or stability parameter α and (in N dimensions) the $N \times N$ radius parameter matrix \mathcal{R}_{kl} . The density function $\mathcal{L}(\mathcal{R}, \alpha, x)$ is expressed as a Fourier transform:

$$\mathcal{L}(\mathcal{R}, \alpha, x) = \int \frac{d^N q}{(2\pi)^N} \exp(iq_k x_k) \exp\left(-\frac{1}{2} |q_k \mathcal{R}_{kl} q_l|^{\alpha/2}\right). \quad (6.1)$$

This density function is normalized to unity and yields the usual Gaussian distribution in the $\alpha = 2$ case, which is the only case when this distribution has finite variance. The $\alpha = 1$ case is known as Cauchy distribution, and there aren't any known simple analytic formulas for the $\alpha \neq 1, \alpha \neq 2$ cases.

From now on we restrict ourselves to the spherically symmetric case in three dimensions, then we have $\mathcal{R}_{kl} = (2^{1/\alpha} R)^2 \delta_{kl}$. We introduced the $2^{1/\alpha}$ numerical prefactor for convenience, and we refer to R as radius parameter. In this case, eq. 6.1 can be simplified to [31]

$$\mathcal{L}(R, \alpha, r) = \frac{1}{2\pi^2 R^2} \int_0^\infty dt \frac{t}{r} \sin\left(\frac{tr}{R}\right) \exp(-t^\alpha). \quad (6.2)$$

This has a power law tail decreasing as $\sim r^{-(3+\alpha)}$, this is obviously the other strong reason for the Lévy distribution.

We assumed a core-halo picture [29], i.e. is the source is separated into a core, which obeys collective dynamics and a halo, which consists of the decay products of long-lived resonances, similarly to Section 5.6 of present PhD thesis. One introduces the λ intercept parameter, which measures the ratio of particles coming from the core. The halo-component of the source can be quite arbitrary, the only condition for S_{halo} is that it has large extension and may not vary in the region where S_{core} is significant. We have chosen the Lévy distribution with large radius for the halo, because this makes the calculations simpler. So the single-particle source function is

$$S_1(r) = S_{core} + S_{halo} = \sqrt{\lambda} \mathcal{L}(2^{-1/\alpha} R_{core}, \alpha, r) + (1 - \sqrt{\lambda}) \mathcal{L}(2^{-1/\alpha} R_{halo}, \alpha, r). \quad (6.3)$$

Then, similarly to eq. 5.20,

$$S(r_{12}) = \int d^3 R S_1\left(R + \frac{r_{12}}{2}\right) S_1\left(R - \frac{r_{12}}{2}\right), \quad (6.4)$$

is the coordinate-averaged two-particle source function, with R being the three-vector of the average spatial coordinates.

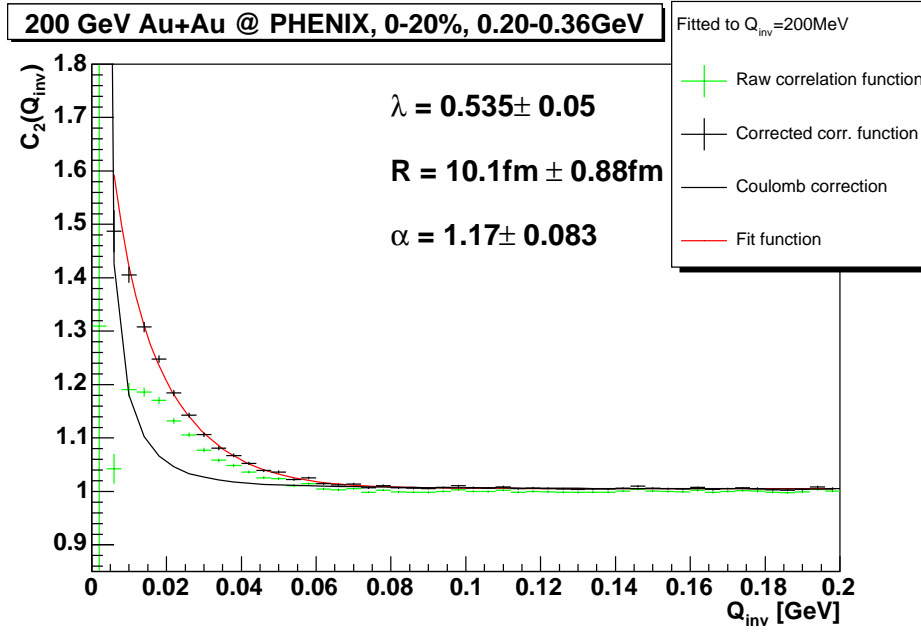


Figure 6.1: Iterative Lévy fit results for 0-20%, $0.2 \text{ GeV}/c < k_t < 0.36 \text{ GeV}/c$

This source function and the correlation functions obtained from it will now be compared to PHENIX source function data [35], in and exactly equal way how it was done in Chapter 5, see especially Section 5.5 of it.

6.3 Application to PHENIX data

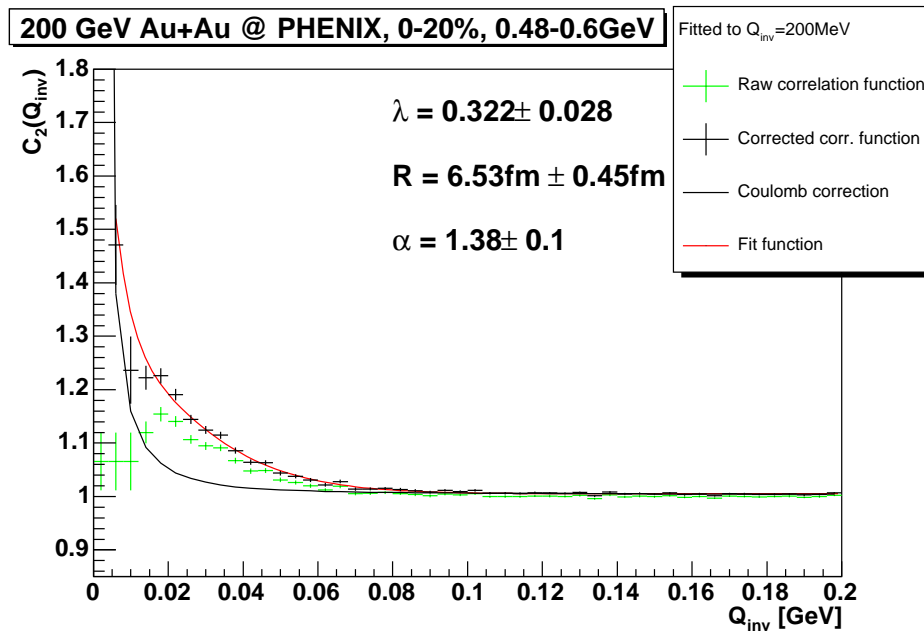
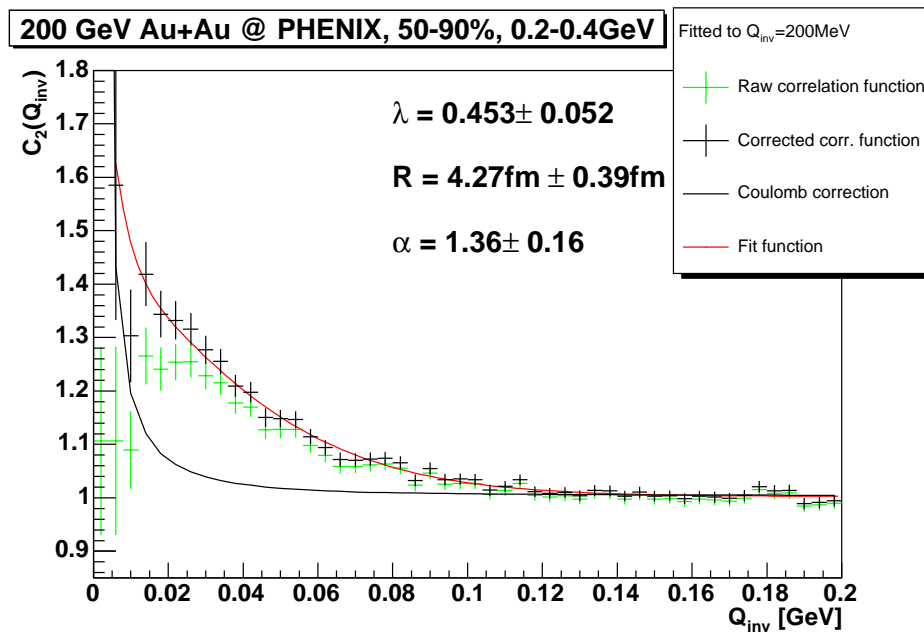
We used the three datasets of PHENIX [35]: they are plotted on fig. 1, fig. 2a and fig. 2b of ref. [35], respectively, henceforth we refer to these datasets with their plot names. The kinematical cuts were:

0–20% centrality, $0.2\text{GeV} < k_t < 0.36\text{GeV}$ for fig. 1 of ref. [35],

0–20% centrality, $0.48\text{GeV} < k_t < 0.6\text{GeV}$ for fig. 2a of ref. [35] and

50–90% centrality, $0.2\text{GeV} < k_t < 0.4\text{GeV}$ for fig. 2b of ref. [35].

Figs. 6.1, 6.2 and 6.3 indicate the result of this method and the obtained source parameters for fig. 1, fig. 2a and fig. 2b of ref. [35], the results are summarized in Table 6.1. The fit range was $q_{inv} = 0.005\text{GeV}$ to 0.2GeV .

Figure 6.2: Iterative Lévy fit results for 0-20%, $0.48 \text{ GeV}/c < k_t < 0.6 \text{ GeV}/c$ Figure 6.3: Iterative Lévy fit results for 40-90%, $0.2 \text{ GeV}/c < k_t < 0.4 \text{ GeV}/c$

PHENIX data	λ	R [fm]	α
Fig. 1 of ref. [35]	0.535 \pm 0.05	10.1 \pm 0.88	1.17 \pm 0.083
Fig. 2a of ref. [35]	0.322 \pm 0.028	6.53 \pm 0.45	1.38 \pm 0.1
Fig. 2b of ref. [35]	0.453 \pm 0.052	4.27 \pm 0.39	1.36 \pm 0.16

Table 6.1: Results on λ , R and α

Source parameters via iterative Coulomb-correction method. R_h was set to 50fm, the fit range was $q_{inv} = 5\text{MeV}$ to 200MeV.

6.4 Systematic tests

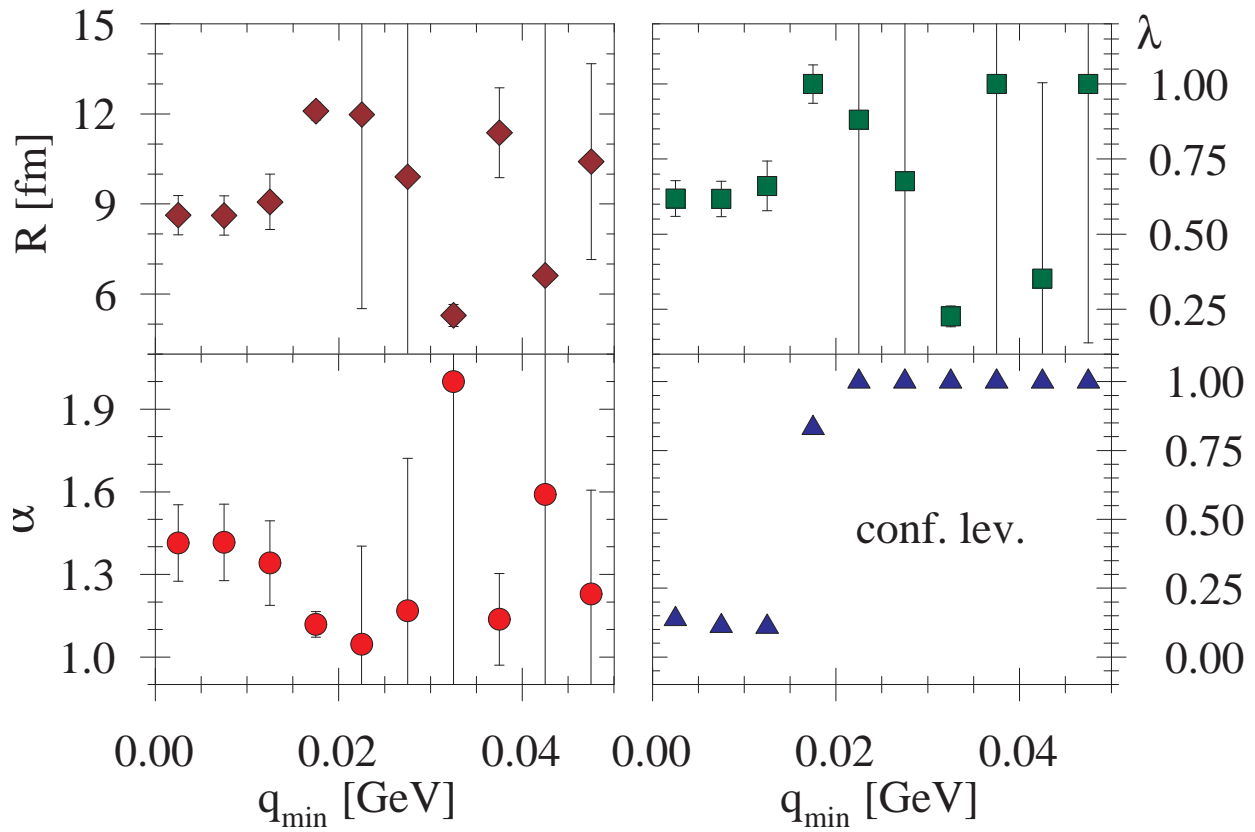
There was an arbitrariness in the iteration process in the choice of the maximum and minimum of the fit range, q_{inv}^{\min} and q_{inv}^{\max} and the R_h halo radius value. Figs. 6.5-6.7 show the change in the obtained parameter values if one changes the fit range, figs. 6.8-6.10 indicates the dependence on the assumed R_{halo} value.

6.5 Direct fit to the experimental source functions

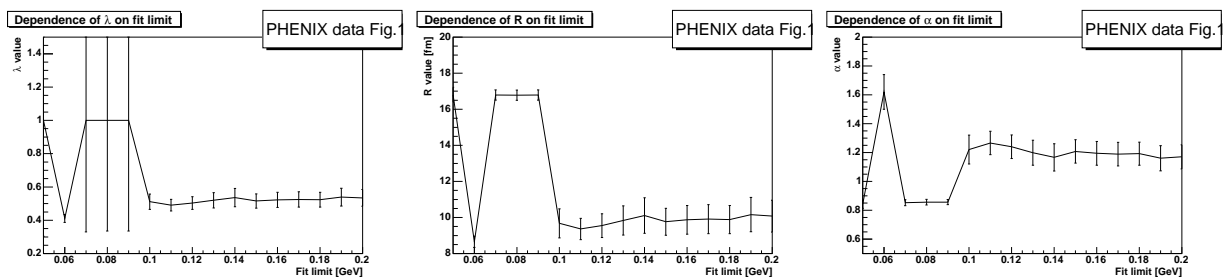
If we directly fit the measured source function, we obtain a parameter set in a much easier manner, but surely this yields wrong errors, because the $S(r_{12})$ obtained via imaging has correlated error bars on itself. But this analysis can cross-test the Coulomb-iterative one.

We calculated the Lévy-like $S(r_{12})$ functions with the parameters obtained from the iterative method discussed above, and compared them to the $S(r_{12})$ functions of ref. [35], which were calculated via the imaging method. The result is plotted on fig. 6.11. Fig. 6.12 shows the result of the direct fit to the $S(r_{12})$ of ref. [35]. The fit parameter values are indicated on the plot.

We made the reconstruction of the $S(r)$ function and the direct fit to $S(r)$ data of ref. [35] in two different ways: In one of the cases we used the numeric tables containing function values in the Coulomb-correction, and in the other case we did not, to see if we make an error by using these function tables (to gain on computing speed). Fig. 6.5 shows the two plots, they are essentially identical, so this method is accurate enough for this analysis.

Figure 6.4: Systematic $q_{\text{inv}}^{\text{min}}$ dependence analysis

Systematic dependence of the source parameters and the confidence level (lower right panel) on $q_{\text{inv}}^{\text{min}}$ is shown. It is clear from the figure that the first three data-points are crucial in determining the fit values.

Figure 6.5: Systematic dependence of the source parameters for fig.1 of ref. [35] on $q_{\text{inv}}^{\text{max}}$

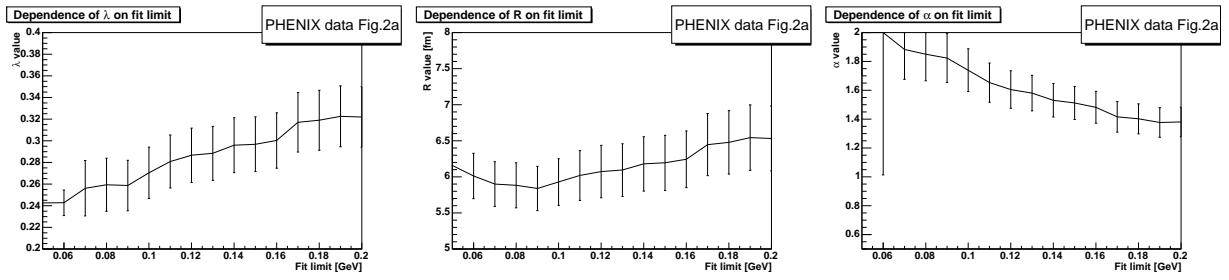


Figure 6.6: Systematic dependence of the source parameters for fig.2a of ref. [35] on q_{inv}^{max}

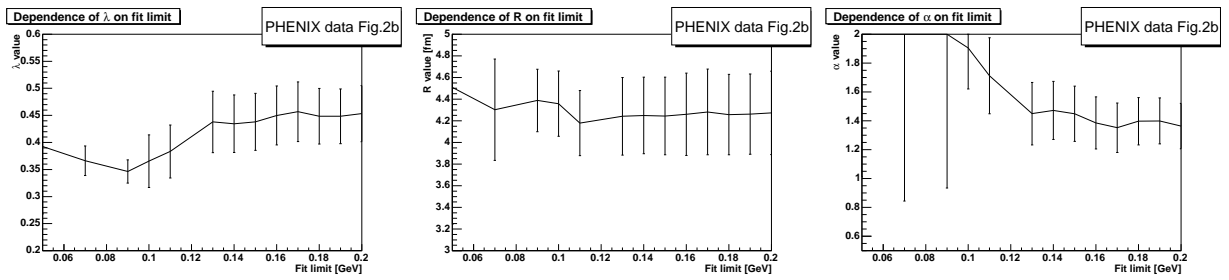


Figure 6.7: Systematic dependence of the source parameters for fig.2b of ref. [35] on q_{inv}^{max}

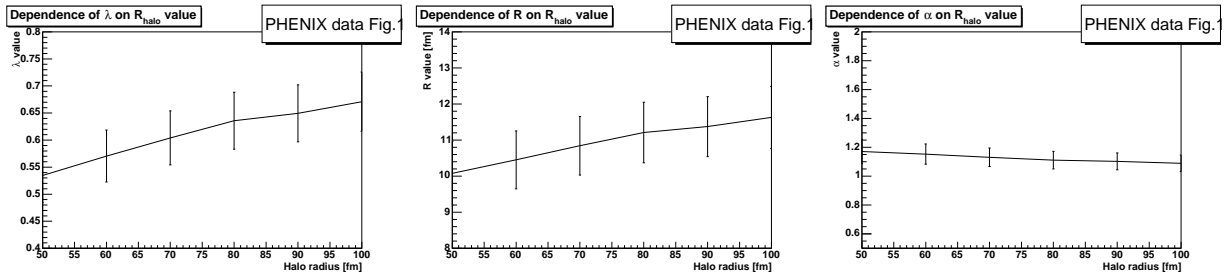


Figure 6.8: Systematic R_{halo} dependence of the source parameters for fig. 1 of ref. [35]

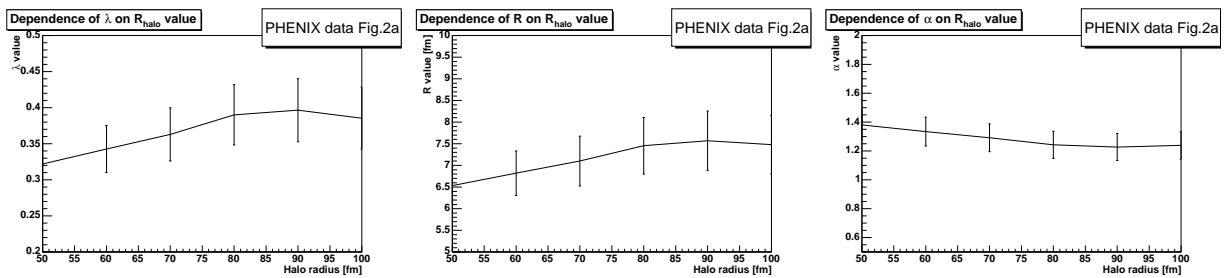


Figure 6.9: Systematic R_{halo} dependence of the source parameters for fig. 2a of ref. [35]

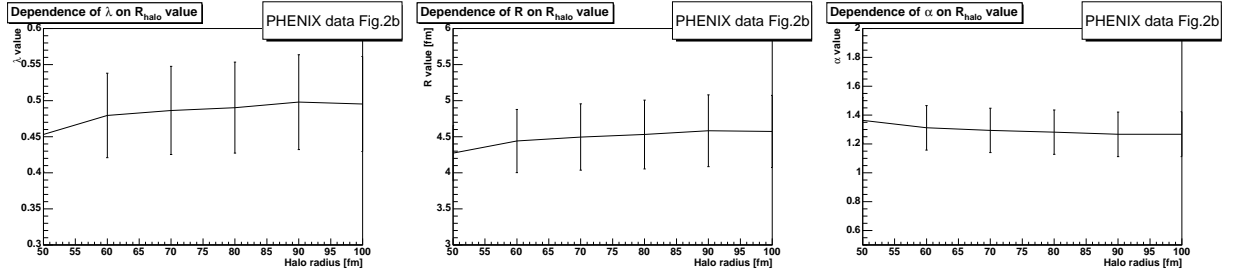
Figure 6.10: Systematic R_{halo} dependence of the source parameters for fig. 2b of ref. [35]

Fig. 1 of ref. [35]				
q_{max} [GeV]		λ	R [fm]	α
0.05	NA	1 \pm 0.7	16.8 \pm 0.41	0.842 \pm 0.029
0.06		0.411 \pm 0.024	8.66 \pm 0.32	1.62 \pm 0.12
0.07	NA	1 \pm 0.67	16.8 \pm 0.28	0.852 \pm 0.021
0.08	NA	1 \pm 0.66	16.8 \pm 0.28	0.856 \pm 0.019
0.09	NA	1 \pm 0.66	16.8 \pm 0.28	0.857 \pm 0.018
0.10		0.512 \pm 0.046	9.68 \pm 0.8	1.22 \pm 0.1
0.11		0.491 \pm 0.035	9.36 \pm 0.59	1.27 \pm 0.081
0.12		0.503 \pm 0.038	9.55 \pm 0.66	1.24 \pm 0.082
0.13		0.52 \pm 0.046	9.83 \pm 0.81	1.2 \pm 0.087
0.14		0.536 \pm 0.055	10.1 \pm 0.98	1.17 \pm 0.095
0.15		0.516 \pm 0.043	9.76 \pm 0.74	1.21 \pm 0.081
0.16		0.523 \pm 0.045	9.87 \pm 0.79	1.19 \pm 0.082
0.17		0.525 \pm 0.046	9.91 \pm 0.81	1.19 \pm 0.082
0.18		0.524 \pm 0.045	9.89 \pm 0.78	1.19 \pm 0.08
0.19		0.539 \pm 0.054	10.2 \pm 0.95	1.16 \pm 0.087
0.20		0.535 \pm 0.05	10.1 \pm 0.88	1.17 \pm 0.083

Table 6.2: Systematic q_{max} dependence analysis

Systematic dependence of the fig. 1 of ref. [35] source parameters on the q_{max} maximum fit value. NA means that the value is not acceptable (the fit algorithm gave the parameter limit back). The same is plotted on fig. 6.5.

Fig. 2a of ref. [35]				
q_{max} [GeV]		λ	R [fm]	α
0.05	NA	0.243 \pm 0.013	6.16 \pm 0.48	2 \pm 0.29
0.06	NA	0.243 \pm 0.012	6.01 \pm 0.31	2 \pm 0.99
0.07		0.256 \pm 0.026	5.9 \pm 0.31	1.88 \pm 0.21
0.08		0.259 \pm 0.025	5.88 \pm 0.31	1.85 \pm 0.18
0.09		0.259 \pm 0.023	5.84 \pm 0.31	1.82 \pm 0.17
0.10		0.27 \pm 0.024	5.93 \pm 0.32	1.74 \pm 0.15
0.11		0.281 \pm 0.024	6.02 \pm 0.34	1.65 \pm 0.14
0.12		0.287 \pm 0.025	6.07 \pm 0.36	1.61 \pm 0.13
0.13		0.288 \pm 0.025	6.09 \pm 0.36	1.58 \pm 0.12
0.14		0.296 \pm 0.025	6.18 \pm 0.38	1.53 \pm 0.12
0.15		0.297 \pm 0.025	6.19 \pm 0.38	1.51 \pm 0.11
0.16		0.3 \pm 0.026	6.24 \pm 0.39	1.48 \pm 0.11
0.17		0.317 \pm 0.027	6.45 \pm 0.43	1.42 \pm 0.11
0.18		0.319 \pm 0.028	6.48 \pm 0.44	1.4 \pm 0.1
0.19		0.323 \pm 0.028	6.54 \pm 0.45	1.38 \pm 0.1
0.20		0.322 \pm 0.028	6.53 \pm 0.45	1.38 \pm 0.1

Table 6.3: Systematic q_{max} dependence analysis

Systematic dependence of the fig. 2a of ref. [35] source parameters on the q_{max} maximum fit value. NA means that the value is not acceptable. The same is plotted on fig. 6.6.

Fig. 2b of ref. [35]				
q_{max} [GeV]		λ	R [fm]	α
0.05	NA	0.392 \pm 0.12	4.51 \pm 1.3	2 \pm 0.99
0.06	NC			\pm
0.07	NA	0.366 \pm 0.027	4.3 \pm 0.47	2 \pm 1.2
0.08	NC			\pm
0.09	NA	0.346 \pm 0.021	4.39 \pm 0.29	2 \pm 1.1
0.10		0.365 \pm 0.049	4.36 \pm 0.3	1.9 \pm 0.28
0.11		0.383 \pm 0.049	4.18 \pm 0.3	1.71 \pm 0.26
0.12	NC			\pm
0.13		0.438 \pm 0.057	4.24 \pm 0.36	1.45 \pm 0.22
0.14		0.435 \pm 0.053	4.25 \pm 0.35	1.47 \pm 0.2
0.15		0.438 \pm 0.053	4.24 \pm 0.36	1.45 \pm 0.19
0.16		0.45 \pm 0.054	4.26 \pm 0.38	1.39 \pm 0.18
0.17		0.457 \pm 0.055	4.28 \pm 0.4	1.35 \pm 0.17
0.18		0.448 \pm 0.051	4.26 \pm 0.37	1.4 \pm 0.16
0.19		0.448 \pm 0.051	4.26 \pm 0.37	1.4 \pm 0.16
0.20		0.453 \pm 0.052	4.27 \pm 0.39	1.36 \pm 0.16

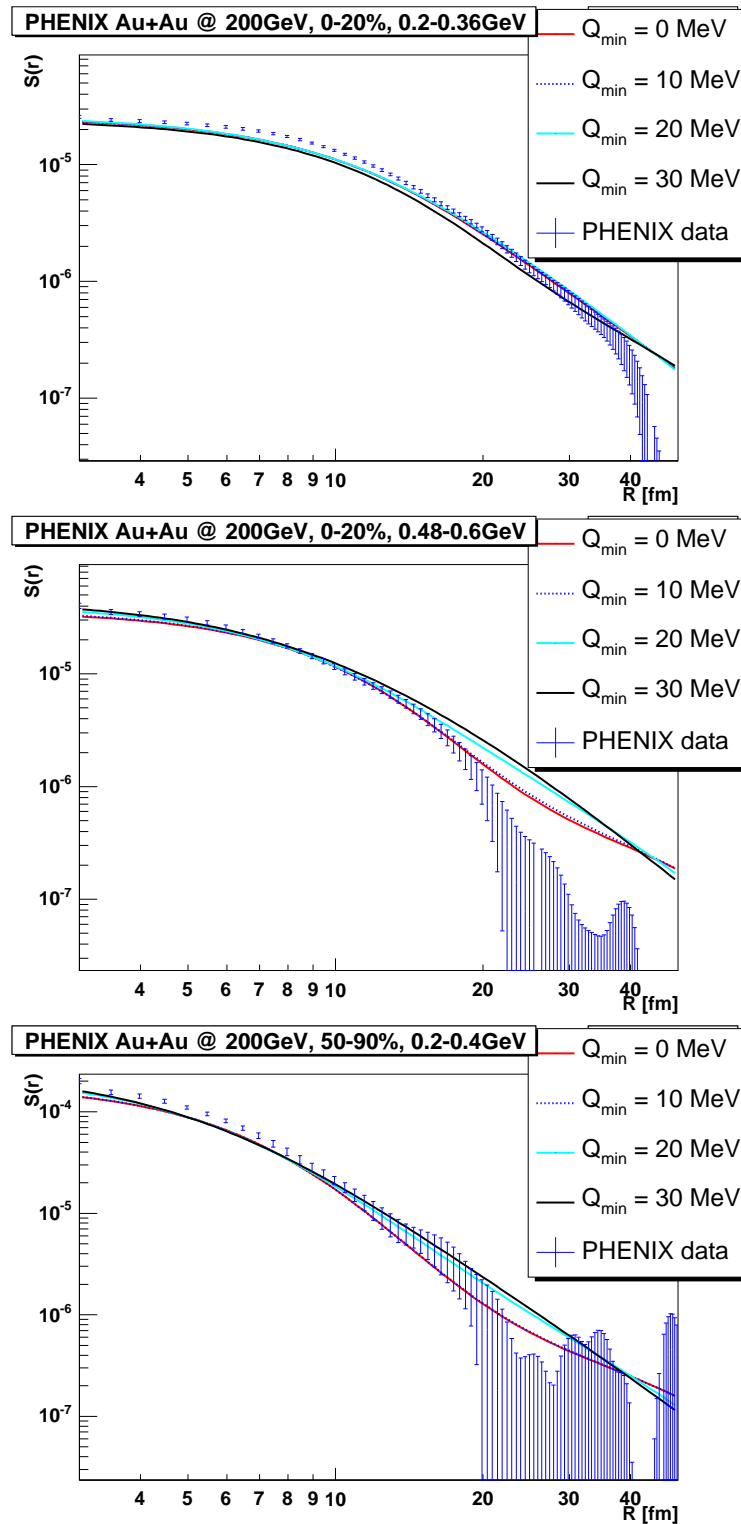
Table 6.4: Systematic q_{max} dependence analysis

Systematic dependence of the fig. 2b of ref. [35] source parameters on the q_{max} maximum fit value. NC indicates that the iteration did not converge, NA means that the value is not acceptable. The same is plotted on fig. 6.7.

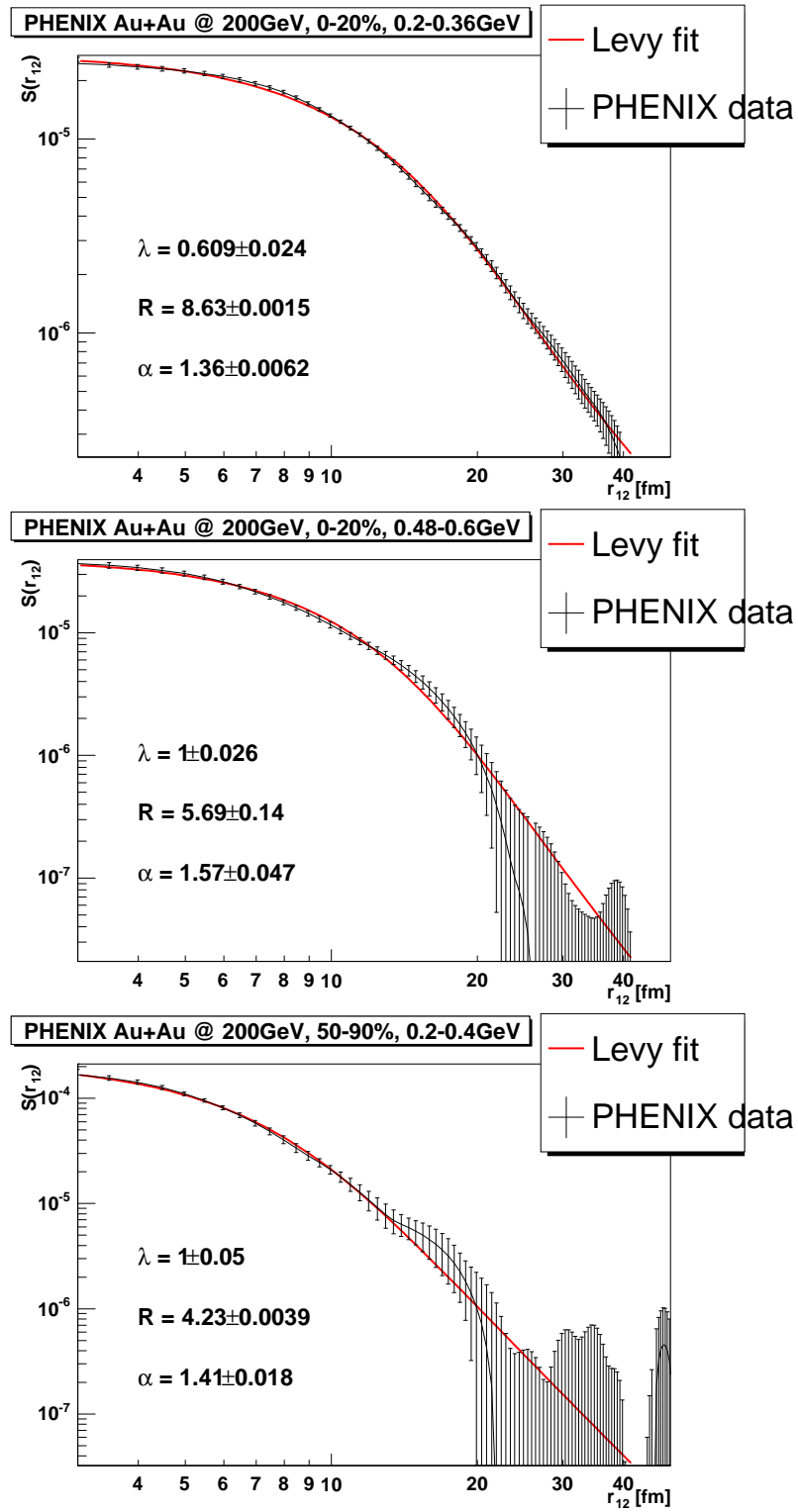
R_{halo} [fm]	λ	R [fm]	α
Fig. 1 of ref. [35]			
50	0.535 \pm 0.05	10.1 \pm 0.88	1.17 \pm 0.083
60	0.571 \pm 0.048	10.5 \pm 0.8	1.15 \pm 0.07
70	0.604 \pm 0.05	10.8 \pm 0.81	1.13 \pm 0.064
80	0.636 \pm 0.053	11.2 \pm 0.84	1.11 \pm 0.061
90	0.649 \pm 0.053	11.4 \pm 0.83	1.1 \pm 0.059
100	0.671 \pm 0.055	11.6 \pm 0.86	1.09 \pm 0.057
Fig. 2a of ref. [35]			
50	0.322 \pm 0.028	6.53 \pm 0.45	1.38 \pm 0.1
60	0.343 \pm 0.033	6.82 \pm 0.51	1.33 \pm 0.099
70	0.363 \pm 0.037	7.1 \pm 0.58	1.29 \pm 0.097
80	0.39 \pm 0.042	7.45 \pm 0.65	1.24 \pm 0.094
90	0.397 \pm 0.044	7.57 \pm 0.68	1.23 \pm 0.094
100	0.385 \pm 0.043	7.48 \pm 0.68	1.24 \pm 0.096
Fig. 2b of ref. [35]			
50	0.453 \pm 0.052	4.27 \pm 0.39	1.36 \pm 0.16
60	0.479 \pm 0.058	4.44 \pm 0.44	1.31 \pm 0.15
70	0.486 \pm 0.061	4.5 \pm 0.46	1.29 \pm 0.15
80	0.49 \pm 0.063	4.53 \pm 0.48	1.28 \pm 0.15
90	0.498 \pm 0.066	4.58 \pm 0.5	1.27 \pm 0.15
100	0.495 \pm 0.066	4.57 \pm 0.5	1.27 \pm 0.16

Table 6.5: Systematic R_{halo} dependence analysis

Systematic dependence of the source parameters on the R_{halo} . The same is plotted on figs. 6.8-6.10.

Figure 6.11: Lévy $S(r_{12})$ test

Comparing $S(r_{12})$ of ref. [35] to the calculated one with the parameters calculated with the Coulomb-iteration. The various curves indicates the minimum fitted q_{inv} values in the iteration.

Figure 6.12: Direct Lévy fit to $S(r_{12})$ 12 data of ref. [35]

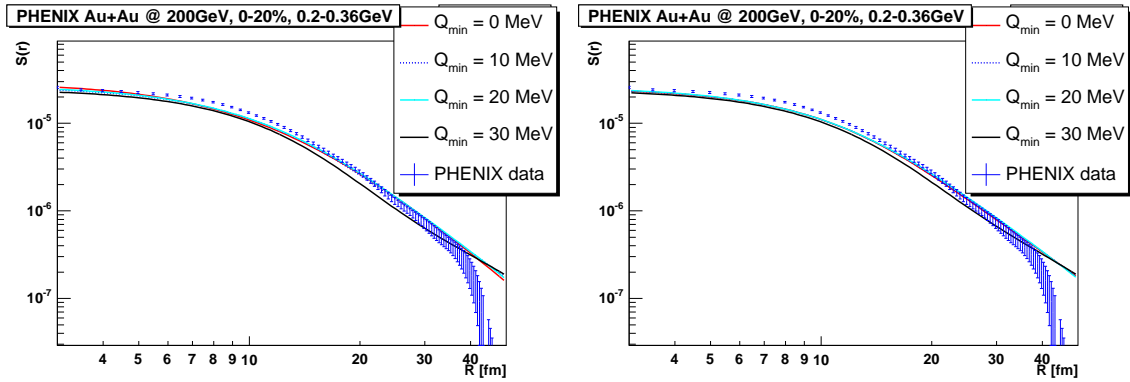


Figure 6.13: Test of the numeric routines

Comparing the first plot of fig. 6.11 if calculated with numeric integration (left) or calculated using data tables to store Lévy- and hypergeometric function values, as well as values for the solution of the Schrödinger-equation. (right)

6.6 Determining the power law tail

The various systematic tests enable us to estimate the systematic error of the parameters, as summarized in Table 6.6. We find from the analysis of the source functions and correlation functions measured by PHENIX [15], that the possible critical exponent α is rather far from as well the Gaussian value $\alpha=2$, as well as the value of $\alpha=0.5$ that would appear in case of a second order phase transition.

Variable	Value	Statistical error	Systematic error		
			from q_{\min}	from R_{halo}	from $S(r_{12})$ fit
Fig 1 of ref. [35]					
λ	0.535	± 0.05	+0.004-0.003	+0.13	+0.074
R [fm]	10.1	± 0.88	+0.05 -0.34	+1.5	-1.5
α	1.17	± 0.083	+0.07 -0.01	-0.08	+0.19
Fig 2a of ref. [35]					
λ	0.322	± 0.028	+0.001-0.04	+0.06	—
R [fm]	6.53	± 0.45	+0.01 -0.6	+0.95	-0.85
α	1.38	± 0.1	+0.3 -0.0	-0.14	+0.19
Fig 2b of ref. [35]					
λ	0.453	± 0.052	+0.04-0.015	+0.04	—
R [fm]	4.27	± 0.39	+0.01-0.03	+0.3	-0.04
α	1.36	± 0.16	+0.1 -0.0	-0.09	+0.05

Table 6.6: Final parameters with errors

Source parameters for data of ref. [35], there are indicated the parameter values, the statistical errors obtained from the fit and the estimated systematic errors.

Chapter 7

Introduction to hydrodynamics

7.1 Relevance of hydrodynamics

When two high energy heavy ions with antiparallel momentum are colliding, in their overlap region such energies, densities and pressures characterize the matter that were present shortly after the birth of our Universe, as described in Section 1.1. The goal of high energy heavy ion physics is to describe and understand this form of matter.

What is measured in experiments (as shortly described in Chapter 2) is the energy and momentum of those thousands of (known) particles that are produced in such collisions.

If we are looking at the distribution of the transverse momentum (p_t) (single particle spectra) of the identified particles one by one, we see an interesting result [38]. They were fitted with $\exp\left(-\frac{p_t^2}{2mT}\right)$ like formulas, where m was the mass of the given particles, and T is treated as the logarithmic slope of these distributions. Interestingly parameter T turned out to show an affine linear connection (or scaling) with the particle mass (see fig. 7.1). This result is however easy to explain by hydro models. Because of this, and because later more and more observables turned out to follow hydro based scalings, let us see how one finds and uses analytic hydro solutions.

In this chapter we shall describe how hydrodynamics in high energy relativistic heavy ion physics works. We will show, how observables can be calculated from an analytic, dynamical solution. Our exemplar will be the nonrelativistic solution of ref. [39].

7.2 Basic equations

Equations of nonrelativistic hydrodynamics are:

$$\partial_t n + \nabla(vn) = 0 \text{ (local conservation of matter, continuity equation),} \quad (7.1)$$

$$\partial_t v + (v\nabla)v = -\frac{\nabla p}{mn} \text{ (local conservation of momentum, Euler-equation),} \quad (7.2)$$

$$\partial_t \epsilon + \nabla(\epsilon v) = -p\nabla v \text{ (local conservation of energy, energy equation).} \quad (7.3)$$

Here n is the number density of the matter, v is the velocity field (i.e. a vector), p the pressure and ϵ the energy. Furthermore m is some kind of mass-equivalent, which makes mass density from n in the right hand side of eq. 7.2, the Euler-equation (i.e. the local version of the Newton-equation). This set of equations is however not yet closed, so we

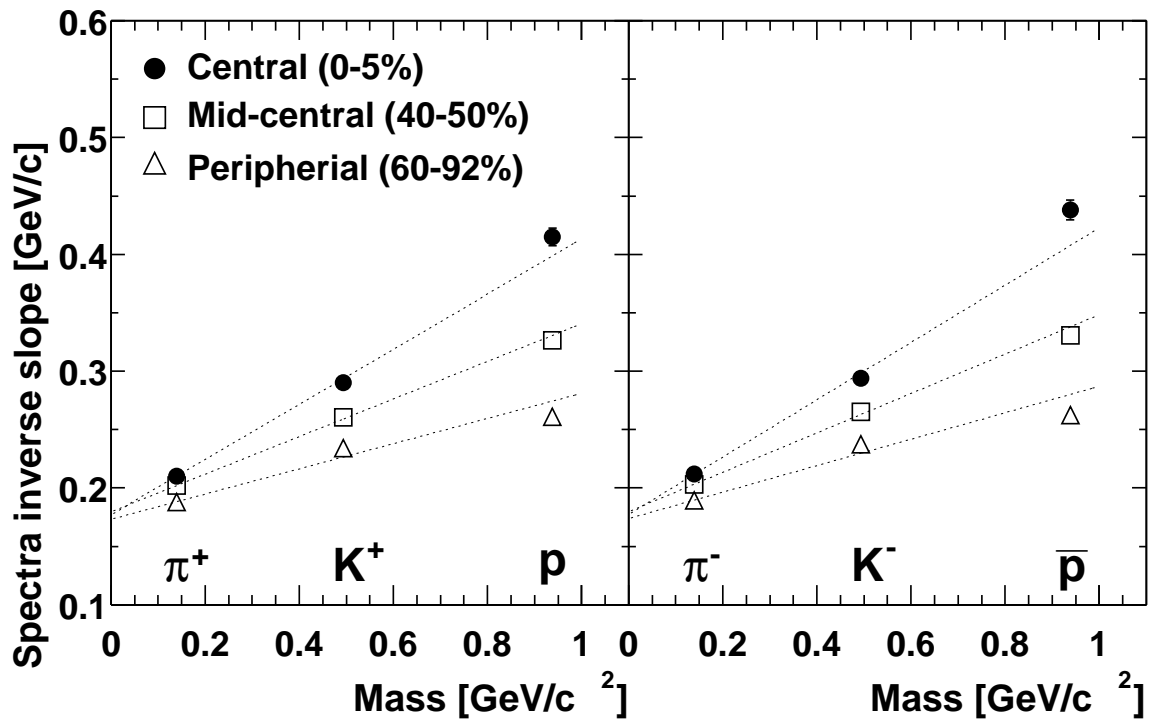


Figure 7.1: Slope of identified particle spectra at PHENIX

Slope parameter T obtained by fitting with $\exp(-p_t^2/2mT)$ of pion, kaon and proton spectra measured in $\sqrt{s_{NN}}=200\text{GeV}$ Au+Au collisions at PHENIX [38].

introduce the following equation of state (EoS):

$$\epsilon = \kappa p, \quad (7.4)$$

and define temperature:

$$p = nT. \quad (7.5)$$

These are the equations which we intend to solve. As our system is highly nonlinear, we have to make several assumptions: these will characterize our model. The first and most important assumption is that of a geometrical symmetry. There are several known solutions with cylindrical symmetry, but these entail longitudinal invariance, which is not supported by the data. Spherical symmetry helps us to find interesting solutions as well, but these cannot be very successful either because of the distinguished direction of the beam. Very natural is however to use ellipsoidal symmetry, we will try to solve the above hydro equations using this idealization. For eq. 7.4 note furthermore, that $\kappa = \partial p / \partial \epsilon = 1/c_s^2$ with c_s being the speed of sound, and $\kappa=3$ corresponds to a massless relativistic gas and $\kappa=3/2$ to an ideal gas.

7.3 Continuity, number density and the velocity field

Let's start with eq. 7.1, and factorize number density as

$$n = f(t)g(s), \quad (7.6)$$

where $f(t)$ is a solely time-dependent function, and $g(s)$ is also a univariate function of scaling variable s . This s being a scaling variable means, that all thermodynamical quantities depend on the space-coordinates only through s . The spatial symmetry of the model will be then the symmetry of s . An ellipsoidally symmetric s will be

$$s = \frac{r_x^2}{X^2} + \frac{r_y^2}{Y^2} + \frac{r_z^2}{Z^2}, \quad (7.7)$$

with the time-dependent parameters of X , Y and Z . It is clear that $s = \text{const.}$ surfaces describe ellipsoids with time-dependent principal axes of X , Y and Z . These principal axes will represent the scales of our system. Our goal is to reduce the non-linear partial differential equations of hydrodynamics to ordinary differential equations on $X(t)$, $Y(t)$ and $Z(t)$.

As a first step, let's look at the derivatives of n present in eq. 7.1, using the factorization of eq. 7.6:

$$\partial_t n = f'(t)g(s) + f(t)g'(s)\partial_t s, \quad (7.8)$$

$$\nabla(vn) = f(t)g(s)\nabla v + f(t)g'(s)v\nabla s. \quad (7.9)$$

If the comoving derivative of s vanishes, i.e.

$$\partial_t s + v\nabla s = 0, \quad (7.10)$$

then eq. 7.1 will look like

$$f'(t) + f(t)\nabla v = 0. \quad (7.11)$$

We find, that with the scaling variable of eq. 7.7, and the following (Hubble-type of) velocity field:

$$v = \left(\frac{\dot{X}}{X} r_x, \frac{\dot{Y}}{Y} r_y, \frac{\dot{Z}}{Z} r_z \right), \quad (7.12)$$

eq. 7.10 can be satisfied.

Now from eq. 7.11 $f(t)$ can be determined, calculating

$$\nabla v = \left(\frac{\dot{X}}{X} + \frac{\dot{Y}}{Y} + \frac{\dot{Z}}{Z} \right), \quad (7.13)$$

we get:

$$f(t) = \frac{X_0 Y_0 Z_0}{XYZ}. \quad (7.14)$$

The other function, $g(s)$ is arbitrary, we can choose for example a gaussian-like density profile:

$$g(s) = e^{-s/2}. \quad (7.15)$$

With this,

$$g'(s) = -g(s)/2. \quad (7.16)$$

7.4 The Euler-equation and the pressure

Continuing with eq. 7.2, the derivatives of v look like this:

$$\partial_t v_x = \frac{X\ddot{X} - \dot{X}^2}{X^2} r_x, \text{ and} \quad (7.17)$$

$$(v\nabla)v_x = \frac{\dot{X}^2}{X^2} r_x, \quad (7.18)$$

and similarly for directions y and z .

So the spatial derivatives of p are as follows,

$$\partial_x p = -mn \left(\frac{X\ddot{X} - \dot{X}^2}{X^2} r_x + \frac{\dot{X}^2}{X^2} r_x \right) = -mn \frac{\ddot{X}}{X} r_x. \quad (7.19)$$

Because the spatial derivatives of n are

$$\partial_x n = f(t)\partial_x g(s) = f(t)g'(s)\partial_x s = 2f(t)g'(s)\frac{r_x}{X^2} = -n\frac{r_x}{X^2}, \quad (7.20)$$

we arrive at these equations:

$$\partial_x p = m\ddot{X}X\partial_x n, \quad (7.21)$$

$$\partial_y p = m\ddot{Y}Y\partial_y n, \quad (7.22)$$

$$\partial_z p = m\ddot{Z}Z\partial_z n. \quad (7.23)$$

Finally, we get from the above:

$$p = m\ddot{X}Xn + F_x(t, y, z), \quad (7.24)$$

$$p = m\ddot{Y}Yn + F_y(t, x, z), \quad (7.25)$$

$$p = m\ddot{Z}Zn + F_z(t, x, y). \quad (7.26)$$

Now if we calculate the derivative of eq. 7.24 by y and put it into eq. 7.22 we get

$$\partial_y F_x(t, y, z) = m(\ddot{Y}Y - \ddot{X}X)\partial_y n, \quad (7.27)$$

where $\partial_y n$ in the right hand side depends on r_x (since we assumed $n \sim g(s)$, n cannot be linear in any coordinate of r , thus $\partial_y n$ has to depend on r_x , except if n is constant) and because the left hand side does not, the prefactor of $\partial_y n$ has to be zero. This argument can be used similarly for the r_z dependence of F_x and the r_x, r_z dependence of F_y and the r_x, r_y dependence of F_z . Thus, if n is not constant, then the only possibility to fulfill eq. 7.27 is by

$$\ddot{X}X = \ddot{Y}Y = \ddot{Z}Z. \quad (7.28)$$

Thus $\partial_i F_j = 0$ and $F_x(y, z, t) = F_y(x, z, t) = F_z(x, y, t) = F(t)$. Finally the result for the pressure is:

$$p = m\ddot{X}Xn + F(t). \quad (7.29)$$

7.5 The energy equation and the temperature

Finally, let's see the energy equation eq. 7.3! Here the derivatives of ϵ look like:

$$\partial_t \epsilon = \kappa T \partial_t n + n \frac{d\kappa T}{dT} \partial_t T, \text{ and} \quad (7.30)$$

$$\nabla(\epsilon v) = \kappa T \nabla(nv) + n \frac{d\kappa T}{dT} v \nabla T. \quad (7.31)$$

Putting these to eq. 7.3, and using eqs. 7.1 and 7.13), we get:

$$n \frac{d\kappa T}{dT} (\partial_t T + v \nabla T) = -nT \left(\frac{\dot{X}}{X} + \frac{\dot{Y}}{Y} + \frac{\dot{Z}}{Z} \right). \quad (7.32)$$

Suppose

$$T = h(t)\tau(s), \quad (7.33)$$

i.e. the temperature depends on the spatial coordinates only through s , and the dependence on time factorizes from this, then because $(\partial_t + v \nabla)\tau(s) = 0$ for arbitrary τ , we get:

$$\frac{d\kappa T}{dT} \frac{\partial_t h(t)}{h(t)} = - \left(\frac{\dot{X}}{X} + \frac{\dot{Y}}{Y} + \frac{\dot{Z}}{Z} \right) = - \frac{\partial_t V}{V}, \quad (7.34)$$

i.e. $\tau(s)$ is really arbitrary. Now suppose κ does not depend on T :

$$\partial_t \log h^\kappa = -\partial_t \log V, \quad (7.35)$$

and from this, we get:

$$T = T_0 \left(\frac{V_0}{V} \right)^{1/\kappa} \tau(s). \quad (7.36)$$

Comparing this to eqs. 7.29-7.28 and the definition of the temperature in eq. 7.5 ($T = p/n$), firstly we get $F(t) = 0$ in eq. 7.29, secondly $\tau(s) = 1$, thirdly:

$$\ddot{X}X = \ddot{Y}Y = \ddot{Z}Z = \frac{T}{m}. \quad (7.37)$$

So the temperature is here spatially homogeneous, this is a consequence of the gaussian density profile.

7.6 Observables

How can we calculate observables from this? First let's see the the Maxwell-Boltzmann distribution using the density, velocity field and temperature from hydro:

$$f(t, r, v) \sim n e^{-\frac{E}{T}} = n \exp \left(- \frac{(p - mv)^2}{2mT} \right), \quad (7.38)$$

where we omitted the normalization constant.

Then with the Boltzmann equation,

$$(\partial_t + v\nabla) f = S, \quad (7.39)$$

we get, that if the freeze-out is instantaneous, i.e. it happens in a $t = t_0$ moment (i.e. $S(t, r, p) \sim \delta(t - t_0)$), the source function (which gives the probability of the production of a particle at r with p momentum, and generates the $f(t, r, v)$ distribution) is:

$$S(r, p) \sim n|_{t_0} \exp\left(-\frac{(p - m v|_{t_0})^2}{2mT_0}\right). \quad (7.40)$$

The one-particle momentum distribution or single particle spectrum (which gives the number of particles with a given momentum) can be calculated from this if we integrate it on space:

$$\frac{d^3 n}{dp^3} = N_1(p) = \int d^3 r S(r, p) \quad (7.41)$$

This can be easily calculated in our case:

$$N_1(p) \sim \int d^3 r \exp\left(-\frac{(p_x - m r_x \dot{X}_0 / X_0)^2}{2mT_0} - \frac{r_x^2}{2X_0^2} - \dots\right), \quad (7.42)$$

where we only wrote out the part with the x direction, as similar terms appear for y and z . The above integration factorizes in the three dimensions, let's see only the x -part:

$$\int dx \exp\left(\frac{-p_x^2 - m^2 r_x^2 \dot{X}_0^2 / X_0^2 + 2p_x m r_x \dot{X}_0 / X_0}{2mT_0} - \frac{r_x^2}{2X_0^2}\right) \quad (7.43)$$

We can rewrite the expression in the exponent:

$$-\frac{p_x^2}{2mT_0} - \left(\frac{r_x^2}{2X_0^2} \frac{T_0 + m\dot{X}_0^2}{T_0} - \frac{r_x}{X_0} \frac{\dot{X}_0 p_x}{T_0}\right), \quad (7.44)$$

and because we have to integrate on r_x , we rewrite it to get a complete square:

$$-\frac{p_x^2}{2mT_0} - \frac{T_0 + m\dot{X}_0^2}{T_0} \left(\frac{r_x^2}{2X_0^2} - \frac{r_x}{X_0} \frac{\dot{X}_0 p_x}{T_0 + m\dot{X}_0^2} + \frac{\dot{X}_0^2 p_x^2}{2(T_0 + m\dot{X}_0^2)^2}\right) + \frac{1}{T_0} \frac{2\dot{X}_0^2 p_x^2}{T_0 + m\dot{X}_0^2}. \quad (7.45)$$

Here the square gives a Gaussian integral, we have to handle now only the rest:

$$-\frac{p_x^2}{2mT_0} + \frac{1}{T_0} \frac{2\dot{X}_0^2 p_x^2}{T_0 + m\dot{X}_0^2} = -\frac{p_x^2}{2m(T_0 + m\dot{X}_0^2)}, \quad (7.46)$$

and introducing

$$T_x = T_0 + m\dot{X}_0^2, \quad (7.47)$$

$$T_y = T_0 + m\dot{Y}_0^2, \quad (7.48)$$

$$T_z = T_0 + m\dot{Z}_0^2 \quad (7.49)$$

we get:

$$N_1(p) \sim \exp\left(-\frac{p_x^2}{2mT_x} - \frac{p_y^2}{2mT_y} - \frac{p_z^2}{2mT_z}\right). \quad (7.50)$$

We can see that the quantities T_x , T_y and T_z describe the slope of the spectra, and these are in affine connection with the particle mass, as it was seen experimentally at RHIC.

In the above parts we have seen, that if one finds an analytic, time dependent, parametric solution of the equations of hydrodynamics (eqs. 7.1-7.5), and assumes some type of a freeze-out, then one can (theoretically) easily calculate the hadronic observables that are measured in relativistic heavy ion collisions. The formulas that describe these observables will contain the model parameters, which can then be adjusted to the measurements, telling us about the state of the matter at the freeze-out. We also see, that the hydro calculation of eqs. 7.47-7.49 is in perfect agreement with the experimental result of fig. 7.1.

Chapter 8

Buda-Lund hydro model for ellipsoidally symmetric fireballs

8.1 Axially symmetric hydrodynamics

8.1.1 The Buda-Lund model

The Buda-Lund hydro model [40] successfully describes BRAHMS, PHENIX, PHOBOS and STAR data on identified single particle spectra and the transverse mass dependent Bose-Einstein or HBT radii as well as the pseudorapidity distribution of charged particles in central Au + Au collisions both at $\sqrt{s_{NN}} = 130$ GeV [41] and at $\sqrt{s_{NN}} = 200$ GeV [42] and in p+p collisions at $\sqrt{s_{NN}} = 200$ GeV [43], as well as data from $Pb + Pb$ collisions at CERN SPS [44] and $h + p$ reactions at CERN SPS [45, 46]

8.1.2 Transition from deconfined to hadronic matter

According to recent lattice QCD calculations, the three kind of equilibrium transitions are possible on the (T, μ_B) plane: if the temperature T is increased at zero or nearly zero μ_B chemical potentials, the transition from confined to deconfined matter is a cross-over [47], i.e. this is not a phase transition in the strict, thermodynamical sense: quark and gluon degrees of freedom are present below T_c , hadrons are present above T_c and various observables yield different estimates for the critical temperature itself. In contrast, at rather large bariochemical potentials, the transition from hadronic matter to deconfined matter is of first order. The line of first order transitions ends at a critical end point (CEP) that separates the first order phase transitions from the cross-over region. At this critical end point, (μ_{CEP}, T_{CEP}) , the transition from confined to deconfined matter is a second order phase transition. There are other more exotic states like color superconducting quark matter, or there is a nuclear liquid-gas phase transition, but the region of the phase diagram that is relevant for high energy heavy ion collisions at CERN SPS, RHIC and LHC, is the region around the CEP [48]. Recent calculations and experimental data indicate that in central Au+Au collisions at RHIC, the transition is likely a cross-over: The extracted central temperatures for the 0-5 % most central $\sqrt{s_{NN}} = 130$ GeV Au+Au data sample are $T_0 = 214 \pm 7$ MeV, and $\mu_B = 77 \pm 38$ MeV, respectively [49]. These values are to be contrasted also with the location of the critical end point of the line of the 1st order QCD phase transition, located preliminarily at $T_{CEP} = 162 \pm 2$ MeV and $\mu_{CEP} = 360 \pm 40$ MeV, according to the lattice

QCD estimate [48].

The result of the Buda-Lund fits to RHIC Au+Au data, both at $\sqrt{s_{\text{NN}}}=130$ and 200 GeV, indicate the existence of a very hot region. The temperature distribution $T(x)$ of this region is characterized with a central temperature T_0 , found to be greater than the critical value calculated from lattice QCD: $T_0 > T_c$ [50]. The Buda-Lund fits thus indicate quark deconfinement in Au + Au collisions at RHIC. The observation of a superheated center in Au+Au collisions at RHIC is confirmed by the analysis of p_t and η dependence of the elliptic flow [50], measured by the PHENIX [13] and PHOBOS collaborations [51, 52]. A similar analysis of Pb+Pb collisions at CERN SPS energies yields central temperatures lower than the critical value, $T_0 < T_c$ [44, 45].

8.1.3 General Buda-Lund hydrodynamics

Hydrodynamics is describing the local conservation of matter, momentum and energy. Due to this nature, hydrodynamical solutions are applied to a tremendous range of physical phenomena ranging from the stellar dynamics to the description of high energy collision of heavy ions as well as collisions of elementary particles. Some of the most famous hydrodynamical solutions, like the Hubble flow of our Universe or the Bjorken flow in ultra-relativistic heavy ion physics have the properties of self similarity and scale-invariance. Heavy ion collisions are known to create three dimensionally expanding systems. In case of non-central collisions, cylindrical symmetry is violated, but an ellipsoidal symmetry can be well assumed to characterize the final state. The data motivated, spherically or cylindrically symmetric hydrodynamical parameterizations and/or solutions of refs. [53, 54] are generalized in the Buda-Lund model, providing new families of exact analytic hydrodynamical solutions.

Hydrodynamics is used to calculate the phase-space distribution, because if we had the phase-space distribution, we could use the collisionless Boltzmann-equation after the freeze-out:

$$\left(\frac{\partial}{\partial t} + v\nabla\right) f = S(r, p, t), \quad (8.1)$$

with v being the velocity field and r the spatial coordinate-vector (both three-vectors). So, we would have the emission function. In order to calculate the phase-space distribution, we have to solve the equations of hydrodynamics. There were Buda-Lund solutions for

both relativistic and nonrelativistic cases. For example, a general group of solutions for nonrelativistic hydro presented in refs. [54–56] is

$$n(t, r) = n_0 \frac{V_0}{V} \nu(s), \quad (8.2)$$

$$v(t, r) = \left(\frac{\dot{X}}{X} r_x, \frac{\dot{Y}}{Y} r_y, \frac{\dot{Z}}{Z} r_z \right) \text{ and} \quad (8.3)$$

$$T(t, r) = T_0 \left(\frac{V_0}{V} \right)^{c_s^2} \mathcal{T}(s), \quad (8.4)$$

if the scales X , Y and Z fulfill

$$X\ddot{X} = Y\ddot{Y} = Z\ddot{Z} = \frac{T_i}{m} \left(\frac{V_0}{V} \right)^{1/\kappa}. \quad (8.5)$$

Here κ is connected to the equation of state (the one used here is $\epsilon = \kappa p = \kappa n T$) i.e. to the speed of sound c_s (in a simple picture):

$$\frac{1}{\kappa} = c_s^2 = \frac{\partial p}{\partial \epsilon}. \quad (8.6)$$

Furthermore, the scaling functions $\nu(s)$ and $\mathcal{T}(s)$ are not independent, but can be calculated from each other:

$$\nu(s) = \frac{1}{\mathcal{T}(s)} \exp \left(-\frac{T_i}{2T_0} \int_0^s \frac{du}{\mathcal{T}(u)} \right), \quad (8.7)$$

and they depend on a scaling variable s , which can be chosen similarly to eq. 7.7 as

$$s = \frac{r_x^2}{2X^2} + \frac{r_y^2}{2Y^2} + \frac{r_z^2}{2Z^2}. \quad (8.8)$$

Then, the Buda-Lund type of solution is a special case, with the choice of

$$\mathcal{T}(s) = \frac{1}{1 + bs} \text{ and} \quad (8.9)$$

$$\nu(s) = (1 + bs) \exp \left(-\frac{T_i}{2T_0} (s + bs^2/2) \right). \quad (8.10)$$

From this solution, the phase-space distribution is approximately

$$f(r, p, t) = C \exp \left(-\frac{r_x^2}{2X(t)^2} - \frac{r_y^2}{2Y(t)^2} - \frac{r_z^2}{2Z(t)^2} - \frac{(p - mv(r, t))^2}{2mT(r, t)} \right), \quad (8.11)$$

with the constant

$$C = \frac{N}{V_0 (4\pi^2 m T_0)^{3/2}}. \quad (8.12)$$

If we now assume a sudden freeze-out and take the simplest, spherically symmetric case with $X = Y = Z$, we can calculate the emission function:

$$S(r, p, t) = C \exp \left(-\frac{r^2}{2R_0^2} - \frac{(p - \frac{m}{\tau}r)^2}{2mT_0} \right) \delta(t - t_0). \quad (8.13)$$

In ref. [57, 58] a group of relativistic solutions was calculated:

$$u_\mu(x) = \frac{x_\mu}{\tau}, \quad (8.14)$$

$$n(x) = n_0 \left(\frac{\tau_0}{\tau} \right)^3 \nu(s), \quad (8.15)$$

$$p(x) = p_0 \left(\frac{\tau_0}{\tau} \right)^{3+3/\kappa}, \quad (8.16)$$

$$T(x) = T_0 \left(\frac{\tau_0}{\tau} \right)^{3/\kappa} \frac{1}{\nu(s)}. \quad (8.17)$$

It was shown [57, 58], that this solution corresponds to the asymptotic, late time limit $t \rightarrow \infty$ of the non-relativistic solution presented in eqs. 8.2-8.4. In the following sections, we will assume an ellipsoidally symmetric, relativistic source function, which is similar to the case of these solutions, but the exact solution, which would lead to that particular source function, was not found yet.

8.2 Ellipsoidal Buda-Lund hydro model

If the experiments at RHIC are performed near to the production threshold of a new state of matter, perhaps only the most violent and most central collisions are sufficient to generate a transition to a new state. However, if the energy is well above the production threshold, new states of matter may appear already in the mid-central or even more peripheral collisions. Hence the deviation from axial symmetry of the observed single particle spectra and two-particle correlation functions can be utilized to characterize the properties of such new states.

Based on the success of the Buda-Lund hydro model to describe the axially symmetric collisions, it is natural to develop an ellipsoidally symmetric extension of the Buda-Lund model, that goes back to the successful axially symmetric case [40, 41, 44, 59, 60] if axial symmetry is restored.

8.2.1 Buda-Lund hydro for relativistic, ellipsoidal expansions

The Buda-Lund model is defined with the help of its emission function $S(x, p)$, where $x = (t, r_x, r_y, r_z)$ is a point in space-time and $p = (E, p_x, p_y, p_z)$ stands for the four-momentum. To take into account the effects of long-lived resonances, we utilize the core-halo model, described in ref. [29] and Section 5.6 of present PhD thesis.

Based on the success of the axial, nonrelativistic Buda-Lund hydro model we assume that the core evolves in a hydrodynamical manner,

$$S_c(x, p)d^4x = \frac{g}{(2\pi)^3} \frac{p^\mu d^4\Sigma_\mu(x)}{B(x, p) + s_q}, \quad (8.18)$$

where g is the degeneracy factor ($g = 1$ for identified pseudoscalar mesons, $g = 2$ for identified spin=1/2 baryons), and $p^\mu d^4\Sigma_\mu(x)$ is a generalized Cooper-Frye term, describing the flux of particles through a distribution of layers of freeze-out hypersurfaces, $B(x, p)$ is the (inverse) Boltzmann phase-space distribution, and the term s_q is determined by quantum statistics, $s_q = 0, -1$, and $+1$ for Boltzmann, Bose-Einstein and Fermi-Dirac distributions, respectively.

For a relativistic, hydrodynamically expanding system, the (inverse) Boltzmann phase-space distribution is

$$B(x, p) = \exp\left(\frac{p^\nu u_\nu(x)}{T(x)} - \frac{\mu(x)}{T(x)}\right). \quad (8.19)$$

We will utilize some ansatz for the shape of the flow four-velocity, $u_\nu(x)$, chemical potential, $\mu(x)$, and temperature, $T(x)$ distributions. Their form is determined with the help of recently found exact solutions of hydrodynamics, both in the relativistic [57, 58, 61] and in the non-relativistic cases [54–56, 62], with the conditions that these distributions are characterized by mean values and variances, and that they lead to (simple) analytic formulas when evaluating particle spectra and two-particle correlations.

The generalized Cooper-Frye prefactor is determined from the assumption that the freeze-out happens, with probability $H(\tau)d\tau$, at a hypersurface characterized by $\tau = \text{const}$ and that the proper-time measures the time elapsed in a fluid element that moves together with the fluid, $d\tau = u^\mu(x)dx_\mu$. We parameterize this hypersurface with the coordinates (r_x, r_y, r_z) and find that $d^3\Sigma^\mu(x|\tau) = u^\mu(x)d^3x/u^0(x)$. Using $\partial_t\tau|_r = u^0(x)$ we find that in this case the generalized Cooper-Frye prefactor is

$$p^\mu d^4\Sigma_\mu(x) = p^\mu u_\mu(x)H(\tau)d^4x, \quad (8.20)$$

This finding generalizes the result of ref. [63] from the case of a spherically symmetric Hubble flow to anisotropic, direction dependent Hubble flow distributions.

From the analysis of CERN SPS and RHIC data [41,44,60], we find that the proper-time distribution in heavy ion collisions is rather narrow, and $H(\tau)$ can be well approximated with a Gaussian representation of the Dirac-delta distribution around the freeze-out proper-time τ_0 ,

$$H(\tau) = \frac{1}{(2\pi\Delta\tau^2)^{1/2}} \exp\left(-\frac{(\tau - \tau_0)^2}{2\Delta\tau^2}\right), \quad (8.21)$$

with $\Delta\tau$ being the proper-time duration of the particle production. Hence we assume $\Delta\tau \ll \tau_0$.

We specify a fully scale invariant, relativistic form for the velocity, temperature and chemical potential fields, which reproduce known non-relativistic hydrodynamic solutions too, in the limit when the expansion is non-relativistic. Both in the relativistic and the non-relativistic cases, the ellipsoidally symmetric, self-similarly expanding hydrodynamical solutions can be formulated in a simple manner, using a scaling variable s and a corresponding four-velocity distribution u^μ , that satisfy

$$u^\mu \partial_\mu s = 0, \quad (8.22)$$

which means that s is a good scaling variable if it's co-moving derivative vanishes [57,58]. This equation couples the scaling variable s and the flow velocity distribution. It is convenient to introduce the dimensionless, generalized space-time rapidity variables (η_x, η_y, η_z) , defined by the identification of

$$(\sinh \eta_x, \sinh \eta_y, \sinh \eta_z) = \left(r_x \frac{\dot{X}}{X}, r_y \frac{\dot{Y}}{Y}, r_z \frac{\dot{Z}}{Z}\right). \quad (8.23)$$

Here (X, Y, Z) are the characteristic sizes (for example, the lengths of the major axis) of the expanding ellipsoid, that depend on proper-time τ and their derivatives with respect to proper-time are denoted by $(\dot{X}, \dot{Y}, \dot{Z})$. The generalization goes back to the original model, if the transverse directed principal axes of the ellipsoid are equal, ie $X = Y$ (and also $\dot{X} = \dot{Y}$).

The deviation from axial symmetry is measured by the momentum-space eccentricity,

$$\epsilon = \frac{\dot{X}^2 - \dot{Y}^2}{\dot{X}^2 + \dot{Y}^2}, \quad (8.24)$$

and the average expansion rate u_t can be also expressed by means of \dot{X} and \dot{Y} :

$$\frac{1}{u_t^2} = \frac{1}{\dot{X}^2} + \frac{1}{\dot{Y}^2}. \quad (8.25)$$

The exact analytic solutions of hydrodynamics [54–58, 61, 62], which form the basis of the Buda-Lund hydro model, develop Hubble-flow for late times, ie $X \rightarrow_{\tau \rightarrow \infty} \dot{X}\tau$, so the momentum-space eccentricity ϵ nearly equals space-time eccentricity. Let us mention $\Delta\eta$ additionally, which represents the elongation of the source expressed in units of space-time rapidity. At the freeze-out $\tau \Delta\eta = Z$ and $Z \approx \dot{Z}\tau$, and so $\Delta\eta \approx \dot{Z}$. Hence we made a connection between the time evolution of the principal axes to conventional physical parameters of heavy ion collisions.

The distributions of $T(x)$, $\mu(x)$ and $u^\mu(x)$ in the above formulas will be given in the η_i variables defined in eq. 8.23, but the integral-form is the standard $d^4x = dt dr_x dr_y dr_z$, so we have to take a Jacobi-determinant into account. Eq. 8.22) is satisfied by the choice of

$$s = \frac{\cosh \eta_x - 1}{\dot{X}^2} + \frac{\cosh \eta_y - 1}{\dot{Y}^2} + \frac{\cosh \eta_z - 1}{\dot{Z}^2}, \quad (8.26)$$

$$u^\mu = (\gamma, \sinh \eta_x, \sinh \eta_y, \sinh \eta_z), \quad (8.27)$$

The above form has the desired non-relativistic limit of eq. 8.8,

$$s \rightarrow \frac{r_x^2}{2X^2} + \frac{r_y^2}{2Y^2} + \frac{r_z^2}{2Z^2}. \quad (8.28)$$

From the normalization condition of $u^\mu(x)u_\mu(x) = 1$ we obtain that:

$$\gamma = \sqrt{1 + \sinh^2 \eta_x + \sinh^2 \eta_y + \sinh^2 \eta_z}. \quad (8.29)$$

For the fugacity distribution we assume a shape, that leads to Gaussian profile in the non-relativistic limit,

$$\frac{\mu(x)}{T(x)} = \frac{\mu_0}{T_0} - s, \quad (8.30)$$

corresponding to the solution discussed in refs. [39, 54, 55]. We assume that the temperature may depend on the position as well as on proper-time. We characterize the inverse temperature distribution similarly to the shape used in the axially symmetric model of ref. [40, 59], and discussed in the exact hydro solutions of refs [54, 55],

$$\frac{1}{T(x)} = \frac{1}{T_0} \left(1 + \frac{T_0 - T_s}{T_s} s \right) \left(1 + \frac{T_0 - T_e}{T_e} \frac{(\tau - \tau_0)^2}{2\Delta\tau^2} \right), \quad (8.31)$$

where T_0 , T_s and T_e are the temperatures of the center, and the surface at the mean freeze-out time τ_0 , while T_e corresponds to the temperature of the center after most of the particle

emission is over (cooling due to evaporation and expansion). Sudden emission corresponds to $T_e = T_0$, and the $\Delta\tau \rightarrow 0$ limit. It's convenient to introduce the following quantities:

$$a^2 = \frac{T_0 - T_s}{T_s} = \left\langle \frac{\Delta T}{T} \right\rangle_r, \quad (8.32)$$

$$d^2 = \frac{T_0 - T_e}{T_e} = \left\langle \frac{\Delta T}{T} \right\rangle_t. \quad (8.33)$$

In the above approach we assume the validity of the concept of local thermalization and the concept of ellipsoidal symmetry at the time of particle production. We do not know, what freeze-out condition that is realized exactly in Nature. Our above formulas can be also considered as a general, second order Taylor expansion of the inverse temperature and logarithmic fugacity distributions, which maintains ellipsoidal symmetry. We will attempt to determine the coefficients of this Taylor expansion from the data. As the saddle-point calculation presented below is sensitive only to second order Taylor coefficients, any model that has similar second order expansion leads to similar results. We also note that the applied distribution of freeze-out temperatures goes back to the dynamical calculation of ref. [64].

8.2.2 Integration and saddlepoint approximation

The observables can be calculated analytically from the Buda-Lund hydro model, using a saddle-point approximation in the integration, i.e. that the particle emission has a narrow and a broad factor in it, and we can take the broad one at the maximum of the narrow distribution and only integrate the latter one. This approximation is exact both in the Gaussian and the non-relativistic limit, and if $p^\nu u_\nu / T \gg 1$ at the point of maximal emittivity. In this approximation, the emission function looks like:

$$S(x, k) d^4x = \frac{g}{(2\pi)^3} \frac{p^\mu u_\mu(x_s) H(\tau_s)}{B(x_s, p) + s_q} \exp(-R_{\mu\nu}^{-2} (x - x_s)^\mu (x - x_s)^\nu) d^4x, \quad (8.34)$$

with x_s being the four-vector of the saddle-point (and further quantities with index s are also meant being at the saddle-point), and where we defined

$$R_{\mu\nu}^{-2} = \partial_\mu \partial_\nu (-\ln(S_0))(x_s, p), \quad (8.35)$$

where we introduced S_0 , as the 'narrow' part of the emission function:

$$S_0(x, p) = \frac{H(\tau)}{B(x, p) + s_q}. \quad (8.36)$$

Furthermore, x_ν stands here for (τ, r_x, r_y, r_z) . In the integration, a Jacobian $\frac{\tau}{t}$ has to be introduced when changing the integration measure from d^4x to $d\tau d^3x$.

The position of the saddle-point can be calculated from the equation

$$\partial_\mu(-\ln(S_0))(x_s, p) = 0. \quad (8.37)$$

In general, we get the following saddle-point equations in $(\tau, \eta_x, \eta_y, \eta_z)$ coordinates:

$$\tau_s = \tau_0, \quad (8.38)$$

$$\sinh \eta_{i,s} = \frac{p_i \dot{X}_i^2 \cosh \eta_{i,s}}{T(x_s) \left(1 + a^2 \frac{p_\mu u^\mu(x_s)}{T_0}\right) + p_0 \frac{\cosh \eta_{i,s}}{\gamma(x_s)} \dot{X}_i^2}, \quad (8.39)$$

where we used (X, Y, Z) as taken at the freeze-out, i.e. $(X(\tau_0), Y(\tau_0), Z(\tau_0))$ or also noted as $X_{1,2,3}$. We will keep this notation in the forthcoming.

The system of eqs. 8.38-8.39 can be solved efficiently for the saddle-point positions $\eta_{s,i}$ using a successive approximation. For the distribution widths, the exact result is:

$$R_{ij}^{-2} = \frac{B(x_s, p)}{B(x_s, p) + s_q} \left(\frac{\dot{X}_i \dot{X}_j}{X_i X_j \cosh \eta_{i,s} \cosh \eta_{j,s}} \frac{1}{\partial \eta_i \partial \eta_j} \right) \Big|_s, \quad (8.40)$$

$$R_{0,0}^{-2} = \frac{t_s}{\tau_s} \frac{1}{\Delta \tau_*^2} = \frac{1}{\Delta \tau^2} + \frac{B(x_s, p)}{B(x_s, p) + s_q} \frac{\partial^2 b}{\partial \tau^2} \Big|_s \quad (8.41)$$

$$R_{i,0}^{-2} = 0, \quad \text{with,} \quad (8.42)$$

$$\frac{\partial^2 b}{\partial \eta_{i,s} \partial \eta_j} \Big|_s = \delta_{ij} \left[\frac{\cosh \eta_{i,s}}{\dot{X}_i^2} + \frac{\cosh \eta_{i,s} a^2}{\dot{X}_i^2 T_0} p_\mu u^\mu(x_s) \right] + \quad (8.43)$$

$$\begin{aligned} &+ \frac{1}{T(x_s)} \left(\frac{E}{\gamma(x_s)} \cosh(2\eta_{i,s}) - p_i \sinh \eta_{i,s} \right) \Big] + \\ &+ \frac{a^2 \sinh \eta_{i,s}}{2T_0 \dot{X}_i^2} \left(\frac{E}{\gamma(x_s)} \sinh(2\eta_{i,s}) - p_i \cosh \eta_{i,s} \right) + \\ &+ \frac{a^2 \sinh \eta_{j,s}}{2T_0 \dot{X}_j^2} \left(\frac{E}{\gamma(x_s)} \sinh(2\eta_{j,s}) - p_j \cosh \eta_{j,s} \right) - \\ &- \frac{E}{4T(x_s) \gamma(x_s)^3} \sinh(2\eta_{i,s}) \sinh(2\eta_{j,s}), \quad \text{and} \end{aligned} \quad (8.44)$$

$$\frac{\partial^2 b}{\partial \tau^2} \Big|_s = \frac{p^\mu u^\mu(x)}{T_0} (1 + a^2 s). \quad (8.45)$$

We introduced here the exponent

$$b(x_s, p) = \log B(x_s, p). \quad (8.46)$$

For clarity, we give the resulting analytic expressions only in the case, where $r_{x,s}/X \ll 1$, $r_{y,s}/Y \ll 1$, and $\eta_s - y \ll \Delta \eta = \dot{Z}$. In this case, we expand the parts of the emission

function into a Taylor series of second order. First:

$$\begin{aligned} \frac{u^\mu(x)p_\mu}{T(x)} &= \frac{m_t \cosh(\eta_z - y)}{T_0} \times \\ &\times \left(1 + a^2 \left(\frac{r_x^2}{2X^2} + \frac{r_y^2}{2^2} + \frac{r_z^2}{2Z^2} \right) + d^2 \frac{(\tau - \tau_0)^2}{2\tau_0^2} + r_x^2 \frac{\dot{X}^2}{2X^2} + r_y^2 \frac{\dot{Y}^2}{2Y^2} \right) \\ &- \frac{p_x \dot{X}}{T_0 X} r_x - \frac{p_y \dot{Y}}{T_0 Y} r_y \end{aligned} \quad (8.47)$$

This way, we get:

$$\begin{aligned} b(x, p) &= \frac{m_t \cosh(\eta_z - y)}{T_0} \times \\ &\times \left(1 + a^2 \left(\frac{r_x^2}{2X^2} + \frac{r_y^2}{2Y^2} + \frac{r_z^2}{2Z^2} \right) + d^2 \frac{(\tau - \tau_0)^2}{2\tau_0^2} + r_x^2 \frac{\dot{X}^2}{2X^2} + r_y^2 \frac{\dot{Y}^2}{2Y^2} \right) \\ &- \frac{p_x \dot{X}}{T_0 X} r_x - \frac{p_y \dot{Y}}{T_0 Y} r_y - \frac{\mu_0}{T_0} + \frac{r_x^2}{2X^2} + \frac{r_y^2}{2Y^2} + \frac{r_z^2}{2Z^2} \end{aligned} \quad (8.48)$$

In this case, from eqs. 8.38-8.39 and eqs. 8.40-8.42 we get the following for the saddle-point and the distribution widths:

$$\frac{r_{i,s}}{Y} = \frac{\frac{p_i \dot{X}_i}{T_0}}{1 + \frac{X_i^2}{R_{T,i}^2}} \text{ for } i = x, y, \quad (8.49)$$

$$\eta_{z,s} - y = \frac{\frac{m_t}{T_0} \sinh y}{\frac{m_t}{T_0} \left(1 + \frac{a^2}{Z^2} \right) \cosh y + \frac{1}{Z^2}}, \quad (8.50)$$

$$\frac{1}{R_{i,j}^2} = \frac{\delta_{ij}}{R_{*,i}^2} = \frac{B(x_s, p)}{B(x_s, p) + s} \left(\frac{1}{X_i^2} + \frac{1}{R_{T,i}^2} \right) \text{ for } i = 1, 2, \quad (8.51)$$

$$\frac{1}{R_{3,3}^2} = \frac{1}{\tau_0^2 \Delta \eta_*^2} = \frac{B(x_s, p)}{B(x_s, p) + s} \left(\frac{1}{\tau_0^2 \dot{Z}^2} + \frac{1}{\tau_0^2 \Delta \eta_T^2} \right), \text{ and} \quad (8.52)$$

$$\frac{1}{\Delta \tau_*^2} = \frac{1}{\Delta \tau^2} + \frac{B(x_s, p)}{B(x_s, p) + s} \frac{1}{\Delta \tau_T^2}. \quad (8.53)$$

Eqs. 8.51-8.53 imply, that the HBT radii are dominated by the smaller of the thermal and the geometrical length scales in all directions. Note that the geometrical scales stem from the density distribution, governed by the fugacity term $\exp(\mu(x)/T(x))$, while the thermal lengths stem from the local thermal momentum distribution $\exp(-p^\mu u_\mu(x)/T(x))$, and in

this limit they are defined as

$$\frac{1}{\Delta\tau_T^2} = \frac{m_t}{T_0} \cosh(\eta_{z,s} - y) \frac{d^2}{\tau_0^2}, \quad (8.54)$$

$$\frac{1}{\Delta\eta_T^2} = \frac{m_t}{T_0} \cosh(\eta_{z,s} - y) \left(1 + \frac{a^2}{Z^2}\right), \quad (8.55)$$

$$\frac{1}{R_{T,i}^2} = \frac{m_t}{T_0} \cosh(\eta_{z,s} - y) \left(\frac{a^2}{X_i^2} + \frac{\dot{X}_I^2}{X_i^2}\right). \quad (8.56)$$

In the simplest case, where all three $\eta_{i,s}$ are small:

$$\frac{r_{i,s}}{X_i} = \frac{\frac{p_i}{T_0} \dot{X}_i}{1 + \frac{X_i^2}{R_{T,i}^2}}, \text{ for } i = x, y, z, \quad (8.57)$$

$$\frac{1}{R_{i,i}^2} = \frac{B(x_s, p)}{B(x_s, p) + s_q} \left(\frac{1}{X_i^2} + \frac{1}{R_{T,i}^2}\right), \text{ for } i = x, y, z, \text{ and} \quad (8.58)$$

$$\frac{1}{\Delta\tau_*^2} = \frac{1}{\Delta\tau^2} + \frac{B(x_s, p)}{B(x_s, p) + s} \frac{1}{\Delta\tau_T^2}. \quad (8.59)$$

In the above limit the thermal lengths are

$$\frac{1}{\Delta\tau_T^2} = \frac{m_t}{T_0} \frac{d^2}{\tau_0^2}, \quad (8.60)$$

$$\frac{1}{R_{T,i}^2} = \frac{m_t}{T_0} \left(\frac{a^2}{X_i^2} + \frac{\dot{X}_I^2}{X_i^2}\right). \quad (8.61)$$

8.3 The invariant momentum distribution

The invariant momentum distribution (IMD) or single-particle spectrum can be calculated as

$$N_1(p) = \int d^4x S(x, p) = \frac{1}{\sqrt{\lambda_*}} \int d^4x S_c(p, x). \quad (8.62)$$

Then the invariant momentum distribution is

$$N_1(p) = \frac{1}{\sqrt{\lambda_*}} \frac{g}{(2\pi)^3} p_\mu u^\mu(x_s) \frac{\Delta\tau_*}{\Delta\tau} [\det R_{i,j}^2]^{1/2} \frac{1}{B(x_s, p) + s_q}.$$

It can be expressed on a more simple way:

$$N_1(p) = \frac{g}{(2\pi)^3} \bar{E} \bar{V} \bar{C} \frac{1}{\exp b(x_s, p) + s_q}, \quad (8.63)$$

where

$$\bar{E} = p_\mu u^\mu(x_s), \quad (8.64)$$

$$\bar{V} = (2\pi)^{3/2} \frac{\Delta\tau_*}{\Delta\tau} [\det R_{ij}^2]^{1/2}, \quad (8.65)$$

$$\bar{C} = \frac{1}{\sqrt{\lambda_*}} \frac{\tau_s}{t_s}. \quad (8.66)$$

Here \bar{E} can be interpreted as the average energy at the freeze-out, \bar{V} the as the average volume at the freeze-out and \bar{C} as a correction factor.

Let us investigate the structure of this IMD. If we evaluate the exponent $b(x_s, p)$ in the limit, where the saddle-point coordinates are all small, (except $\eta_{z,s}$, which we denote from here as η_s simply):

$$\begin{aligned} b(x_s, p) &= -\frac{r_{x,s}}{2R_{*,x}^2} - \frac{r_{y,s}}{2R_{*,y}^2} + \frac{\eta_s^2}{2} \left(\frac{m_t}{T_0} \cosh(\eta_s - y) \frac{a^2}{\dot{Z}^2} + \frac{1}{\dot{Z}^2} \right) + \\ &+ \frac{m_t}{T_0} \cosh(\eta_s - y) - \frac{\mu_0}{T_0}. \end{aligned} \quad (8.67)$$

Or, in an other form

$$b(x_s, p) = \frac{p_x^2}{2\bar{m}_t T_{*,x}} + \frac{p_y^2}{2\bar{m}_t T_{*,y}} - \frac{p_t^2}{2\bar{m}_t T_0} + \frac{\eta_s^2}{2} \left(\frac{\bar{m}_t}{T_0} \frac{a^2}{\dot{Z}^2} + \frac{1}{\dot{Z}^2} \right) + \frac{\bar{m}_t}{T_0} - \frac{\mu_0}{T_0}, \quad (8.68)$$

where $\bar{m}_t = m_t \cosh(\eta_s - y)$ and the direction dependent slope parameters are

$$T_{*,x} = T_0 + \bar{m}_t \dot{X}^2 \frac{T_0}{T_0 + \bar{m}_t a^2}, \quad (8.69)$$

$$T_{*,y} = T_0 + \bar{m}_t \dot{Y}^2 \frac{T_0}{T_0 + \bar{m}_t a^2}. \quad (8.70)$$

It is useful to show the low-rapidity limit, where η is small, because it helps to understand the behavior of our formulas, although in data fitting we used the exact, more complicated formulas. The Boltzmann-exponent b is in this low-rapidity limit the following:

$$b(x_s, p) = \frac{p_x^2}{2\bar{m}_t T_{*,x}} + \frac{p_y^2}{2\bar{m}_t T_{*,y}} + \frac{p_z^2}{2m_t T_{*,z}} + \frac{m_t}{T_0} - \frac{p_t^2}{2m_t T_0} - \frac{\mu_0}{T_0}, \quad (8.71)$$

where

$$T_{*,z} = T_0 + m_t \dot{Y}^2 \frac{T_0}{T_0 + m_t a^2}. \quad (8.72)$$

In the limit when the possibility of a temperature inhomogeneity on the freeze-out hypersurface is neglected, we can substitute $a = 0$. Using a non-relativistic approximation

of $\bar{m}_t \approx m$, we recover the recent result of ref. [39] for the mass dependence of the slope parameters of the single-particle spectra:

$$T_{*,x} = T_0 + m \dot{X}^2, \quad (8.73)$$

$$T_{*,y} = T_0 + m \dot{Y}^2, \quad (8.74)$$

$$T_{*,z} = T_0 + m \dot{Z}^2. \quad (8.75)$$

Thus we have generalized the Buda-Lund hydro model to the case of ellipsoidally symmetric expanding fireballs. We calculated the source function and the invariant momentum distribution from the model, and we arrived at simple formulas. In the next two chapters we will use these to calculate more observables from the model, in particular correlation functions and the elliptic flow.

Chapter 9

Elliptic flow from the Buda-Lund model

9.1 Elliptic flow in high energy heavy ion collisions

One of the unexpected results from experiments at the Relativistic Heavy Ion Collider (RHIC) is the relatively strong second harmonic moment of the transverse momentum distribution, referred to as the elliptic flow. Measurements of the elliptic flow by the PHENIX, PHOBOS and STAR collaborations (see refs. [13, 65–69]) reveal rich details in terms of its dependence on particle type, transverse (p_T) and longitudinal momentum (η) variables, and on the centrality and the bombarding energy of the collision. In the soft transverse momentum region ($p_T \lesssim 2 \text{ GeV}/c$) measurements at mid-rapidity are found to be well described by hydrodynamical models [3, 70]. By contrast, differential measurement of the pseudo-rapidity dependence of elliptic flow and its excitation function have resisted several attempts at a description in terms of hydrodynamical models (but see their new description by the SPHERIO model [71]). Here we show that these data are consistent with theoretical, analytic predictions that are based on perfect fluid hydrodynamics.

We focus here on the analytic approach in exploring the consequences of the presence of perfect fluids in high energy heavy ion experiments in Au+Au collisions at RHIC. Such exact analytic solutions were published recently in refs. [39, 57, 61, 72]. A tool, that is based on the above listed exact, dynamical hydro solutions, is the Buda-Lund hydro model of Chapter 8 of present PhD thesis and refs. [40, 50]. This hydro model is successful in describing experimental data on single particle spectra and two-particle correlations [41, 42]. The model is defined with the help of its emission function; to take into account the effects of long-lived resonances, it utilizes the core-halo model [29].

9.2 Calculating the elliptic flow

The elliptic flow is an experimentally measurable observable and is defined as the azimuthal anisotropy or second Fourier-coefficient of the single-particle momentum distribution $N_1(p)$. The Fourier decomposition of N_1 in the angle φ is:

$$N_1(p) = \frac{dn}{dp_z p_t dp_t d\varphi} = \frac{dn}{dp_z p_t dp_t 2\pi} \left(1 + 2 \sum_n v_n \cos(n\varphi) \right) \quad (9.1)$$

From this equation follows, that

$$\frac{dn}{dp_z p_t dp_t d\varphi} \bigg/ \frac{dn}{dp_z p_t dp_t 2\pi} = \left(1 + 2 \sum_n v_n \cos(n\varphi) \right) \quad (9.2)$$

Hence, using the properties of the Fourier-decomposition, the definition of the flow coefficients is equal to:

$$v_n = \frac{\int_0^{2\pi} N_1(p) \cos(n\varphi) d\varphi}{\int_0^{2\pi} N_1(p) d\varphi}, \quad (9.3)$$

This formula returns the elliptic flow v_2 for $n = 2$.

We take $N_1(p)$ from the Buda-Lund model, see eq. 8.63. Here $b(x_s, p)$ is the only part of the invariant one-particle momentum distribution, that is explicitly angle dependent, so

$$\begin{aligned} N_1(p) &\sim \exp\left(-\frac{p_x^2}{2\bar{m}_t T_{*,x}} - \frac{p_y^2}{2\bar{m}_t T_{*,y}}\right) = \\ &= \exp\left(-\frac{p_t^2}{2\bar{m}_t T_{eff}} + \left(\frac{p_t^2}{2\bar{m}_t T_{*,x}} - \frac{p_t^2}{2\bar{m}_t T_{*,y}}\right) \frac{\cos(2\varphi)}{2}\right), \end{aligned} \quad (9.4)$$

where

$$T_{eff} = \frac{1}{2} \left(\frac{1}{T_{*,x}} + \frac{1}{T_{*,y}} \right). \quad (9.5)$$

For the definition of $T_{*,x,y}$, see eq. 8.69. Now we can easily extract the angular dependencies.

Let us compute v_2 by integrating on the angle:

$$v_2 = \frac{I_1(w)}{I_0(w)}, \quad (9.6)$$

where

$$w = \frac{p_t^2}{4\bar{m}_t} \left(\frac{1}{T_{*,y}} - \frac{1}{T_{*,x}} \right), \quad (9.7)$$

and $I_n(z)$ stands for the modified Bessel function of the second kind,

$$I_n(z) = (1/\pi) \int_0^\pi \exp(n \cos(\theta)) \cos(n\theta) d\theta. \quad (9.8)$$

Generally, we get from the definition (eq. 9.3) the following equations:

$$v_{2n} = \frac{I_n(w)}{I_0(w)}, \quad \text{and} \quad (9.9)$$

$$v_{2n+1} = 0. \quad (9.10)$$

As first and the third flow coefficients vanish in this case, a tilt angle ϑ has to be introduced to get results compatible with observations, as discussed in the subsequent parts.

Note that for large rapidities, $|\eta_s - y|$ becomes also large, so $\bar{m}_t = m_t \cosh(\eta_s - y)$ diverges and

$$\frac{1}{T_{*,y}} - \frac{1}{T_{*,x}} \rightarrow \frac{1}{T_0} \left(\frac{a^2}{a^2 + \dot{Y}^2} - \frac{a^2}{a^2 + \dot{X}^2} \right), \quad (9.11)$$

hence

$$w \xrightarrow[\eta \rightarrow \infty]{} 0. \quad (9.12)$$

Thus we find a natural mechanism for the decrease of v_2 for increasing values of $|y|$, as in this limit, $v_2 \rightarrow I_1(0)/I_0(0) = 0$.

9.3 Elliptic flow for tilted ellipsoidal expansion

Now, let us compute the elliptic flow for tilted, ellipsoidally expanding sources, too, because we can get a non-vanishing v_1 and v_3 only this way, in case of $\vartheta \neq 0$, similarly to the non-relativistic case discussed in ref. [39]. The observables are determined in the center of mass frame of the collision (CMS or LAB frame), where the r_x axis points to the direction of the impact parameter and the r_z axis points to the direction of the beam. In this frame, the ellipsoidally expanding fireball, described in the previous subsections, may be rotated. So let us assume, that we re-label all the x and p coordinates in the previous parts with the superscript ', e.g. $x \rightarrow x'$ and $p \rightarrow p'$, to indicate, that these calculations were performed in the system of ellipsoidal expansion (SEE), where the principal axis of the expanding ellipsoid coincide with the principal axis of SEE. In the following, we use the unprimed variables to denote quantities defined in the CMS, the frame of observation.

We assume, that the initial conditions of the hydrodynamic evolution correspond to a rotated ellipsoid in CMS [39]. The tilt angle ϑ represents the rotation of the major (longitudinal) direction of expansion, r'_z , from the direction of the beam, r_z . Hence the event plane is the (r'_x, r'_z) plane, which is the same, as the (r_x, r_z) plane. The (zenithal) angle between directions r_z and r'_z is the tilt angle ϑ , while (azimuthal) angle φ is between the event plane and the direction of the transverse momentum p_t .

We have made the coordinate transformation

$$p'_x = p_x \cos \vartheta - p_z \sin \vartheta, \quad (9.13)$$

$$p'_y = p_y, \quad (9.14)$$

$$p'_z = p_z \cos \vartheta + p_x \sin \vartheta, \quad (9.15)$$

where the ' means, that we have the IMD in the system of ellipsoidal expansion. In addition, we transform the momentum:

$$p_x = p_t \cos \varphi, \quad (9.16)$$

$$p_y = p_t \sin \varphi, \quad (9.17)$$

The changes in the coordinates are taken in first order in ϑ .

$$N_1(m_t, p_x, p_y, y) \rightarrow N'_1(m'_t, p'_t, \varphi, y) \quad (9.18)$$

$$p_x(m'_t, y', p'_t, \varphi) = p'_t \cos \varphi - (m'_t \sinh y') \vartheta \quad (9.19)$$

$$p_y(m'_t, y', p'_t, \varphi) = p'_t \sin \varphi \quad (9.20)$$

$$y(m'_t, y', p'_t, \varphi) = y' + \left(\frac{p'_t}{m'_t} \cosh y' \cos \varphi \right) \vartheta \quad (9.21)$$

$$m_t(m'_t, y', p'_t, \varphi) = m'_t - (p'_t \sinh y' \cos \varphi) \vartheta \quad (9.22)$$

Now, with second order calculations in p/T_0 and first order in ϑ , we get for $b(x_s, p') = \ln B(x_s, p')$:

$$\begin{aligned} b(x_s, p') &= \frac{p_t'^2 \cos^2 \varphi}{2m_t \tilde{T}'_{*,x}} + \frac{p_t'^2 \sin^2 \varphi}{2m_t T'_{*,y}} + \frac{p_z'^2}{2m_t \tilde{T}'_{*,z}} + \\ &+ \frac{p'_t p'_z}{m_t} \vartheta \cos \varphi \left(\frac{1}{T'_{*,z}} - \frac{1}{T'_{*,x}} \right) + \frac{1}{T_0} \left(\mu_0 - m_t + \frac{p_t'^2}{m_t} \right) \end{aligned} \quad (9.23)$$

Here for $i = x, y, z$

$$T'_{*,i} = T_0 \left(1 + m'_t \frac{\dot{R}_i^2}{T_0 + m'_t a^2} \right), \quad (9.24)$$

and

$$\frac{1}{\tilde{T}'_{*,x}} = \frac{\cos^2 \vartheta}{T'_{*,x}} + \frac{\sin^2 \vartheta}{\tilde{T}'_{*,z}} \simeq \frac{1}{T'_{*,x}} \quad (9.25)$$

$$\frac{1}{\tilde{T}'_{*,z}} = \frac{\cos^2 \vartheta}{T'_{*,z}} + \frac{\sin^2 \vartheta}{\tilde{T}'_{*,x}} \simeq \frac{1}{T'_{*,z}} \quad (9.26)$$

From the experiments, we now from the experiment that the prefactor of the IMD is approximately

$$m_t \cosh(\eta_s - y) \frac{\Delta\tau_*}{\Delta\tau} 2\pi R_{*,x} R_{*,y} \sqrt{2\pi\tau_0^2 \Delta\eta_*^2} = \left(\frac{T_0}{m_t}\right)^\alpha \quad (9.27)$$

$$= \left(\frac{T_0}{m'_t}\right)^\alpha (1 + C_1 \alpha \cos \vartheta) \quad (9.28)$$

so finally, we get:

$$N_1(m'_t, p'_t, \varphi, y) = C_0 (1 + C_1 \alpha \vartheta \cos \varphi) e^{w' \cos 2\varphi + c_2 \vartheta \cos \varphi + C_3 \vartheta \cos(3\varphi)} \quad (9.29)$$

where C_i may depend on all variables, except φ . So we get for the IMD, with a first order calculation in ϑ :

$$N_1(m'_t, p'_t, \varphi, y) \sim (1 + (\beta_1 \cos \varphi + \beta_2 \cos(3\varphi))\vartheta) e^{w' \cos 2\varphi} \quad (9.30)$$

Now, we can calculate v_n . For this, the following rule is very useful:

$$\cos(n_1 \varphi) \cos(n_2 \varphi) = \frac{1}{2} (\cos((n_1 + n_2)\varphi) + \cos((n_1 - n_2)\varphi)) \quad (9.31)$$

Finally (with a similar calculation to the one in the former section) we get a similar result to eq. 9.6:

$$v_{2n} = \frac{I_n(w')}{I_0(w')}, \quad (9.32)$$

$$v_{2n+1} = \frac{\vartheta \beta_1}{2} \left(\frac{I_n(w') + I_{n+1}(w')}{2} \right) + \frac{\vartheta \beta_2}{2} \left(\frac{I_{|n-1|}(w') + I_{n+2}(w')}{2} \right). \quad (9.33)$$

Here, the argument w is the same, as before, only, that it depends on the transformed coordinates:

$$w' = \frac{p_t'^2}{4m_t'} \left(\frac{1}{T'_{*,y}} - \frac{1}{T'_{*,x}} \right), \quad (9.34)$$

i.e. $w' \approx w$ for $\vartheta \approx 0$. In our case:

$$\begin{aligned} \beta_1 &= -\frac{p_t'^3 \sinh y'}{2m_t'^2} \left(\frac{3}{2} \frac{1 + \frac{\dot{X}^2}{a^2}}{T_{*,x}'^2} + \frac{1}{2} \frac{1 + \frac{\dot{Y}^2}{a^2}}{T_{*,y}'^2} - \frac{1}{T_0} \right) - \\ &\quad - p_t' \sinh y' \left(\frac{1}{T'_{*,z}} - \frac{1}{T'_{*,x}} \right) + \frac{p_t'}{m_t'} \alpha \sinh y' \cos \varphi \end{aligned} \quad (9.35)$$

$$\beta_2 = -\frac{p_t'^3 \sinh y'}{2m_t'^2} \frac{1}{2} \left(\frac{1 + \frac{\dot{X}^2}{a^2}}{T_{*,x}'^2} - \frac{1 + \frac{\dot{Y}^2}{a^2}}{T_{*,y}'^2} \right) \quad (9.36)$$

Specially:

$$v_1 = \frac{\vartheta\beta_1}{2} \left(\frac{I_0(w') + I_1(w')}{2} \right) + \frac{\vartheta\beta_2}{2} \left(\frac{I_1(w') + I_2(w')}{2} \right) \quad (9.37)$$

$$v_2 = \frac{I_1(w')}{I_0(w')} \quad (9.38)$$

$$v_3 = \frac{\vartheta\beta_1}{2} \left(\frac{I_1(w') + I_2(w')}{2} \right) + \frac{\vartheta\beta_2}{2} \left(\frac{I_0(w') + I_3(w')}{2} \right) \quad (9.39)$$

These are the easy-to-understand-formulas, but at present, experimental information on v_2 does enable us to determine ϑ , hence in comparing our results to experimental data, we restrict ourselves to the model without a tilt angle.

9.4 Universal scaling of the elliptic flow at RHIC

The result for the elliptic flow, that comes directly from a perfect hydro solution is again the following simple scaling law [39, 50]

$$v_2 = \frac{I_1(w)}{I_0(w)}, \quad (9.40)$$

where again, $I_n(z)$ stands for the modified Bessel function of the second kind.

Thus the Buda-Lund hydro model predicts [39] a *universal scaling*: every v_2 measurement is predicted to fall on the same scaling curve I_1/I_0 when plotted against the scaling variable w . This means, that v_2 depends on any physical parameter (transverse or longitudinal momentum, mass, center of mass energy, collision centrality, type of the colliding nucleus etc.) only through the scaling variable w . This scaling variable (defined in eq. 9.7) can be expressed as:

$$w = \frac{E_K}{T_*} \varepsilon \quad (9.41)$$

Here E_K is a relativistic generalization of the transverse kinetic energy, defined as

$$E_K = \frac{p_t^2}{2\bar{m}_t}, \quad (9.42)$$

with

$$\bar{m}_t = m_t \cosh \left(\frac{y}{1 + \Delta\eta \frac{m_t}{T_0}} \right), \quad (9.43)$$

y being the rapidity, $\Delta\eta$ the longitudinal expansion of the source, T_0 the central temperature at the freeze-out and $m_t = \sqrt{p_t^2 + m^2}$ the transverse mass, similarly to Section 8.3. We note,

that at mid-rapidity and for a leading order approximation, $E_K \approx m_t - m$, which also explains recent development on scaling properties of v_2 by the PHENIX experiment at midrapidity [14, 73]. We furthermore note, that parameter $\Delta\eta$ has recently been dynamically related [61] to the acceleration parameter of new exact solutions of relativistic hydrodynamics, where the accelerationless limit corresponds to a Bjorken type, flat rapidity distribution and the $\Delta\eta \rightarrow \infty$ limit.

The scaling variable w also depends on the parameter T_* , which is the effective, rapidity and transverse mass dependent slope of the azimuthally averaged single particle spectra, and on the momentum space eccentricity parameter, ε . These can be defined [39, 50] by the transverse mass and rapidity dependent slope parameters of the single particle spectra in the impact parameter (subscript x) and out of the reaction plane (subscript y) directions, T_x and T_y ,

$$\frac{1}{T_*} = \frac{1}{2} \left(\frac{1}{T_x} + \frac{1}{T_y} \right), \quad (9.44)$$

$$\varepsilon = \frac{T_x - T_y}{T_x + T_y}. \quad (9.45)$$

which are thus observable quantities. In the Buda-Lund hydro model [39, 50], the rapidity and the transverse mass dependence of the slope parameters is given as

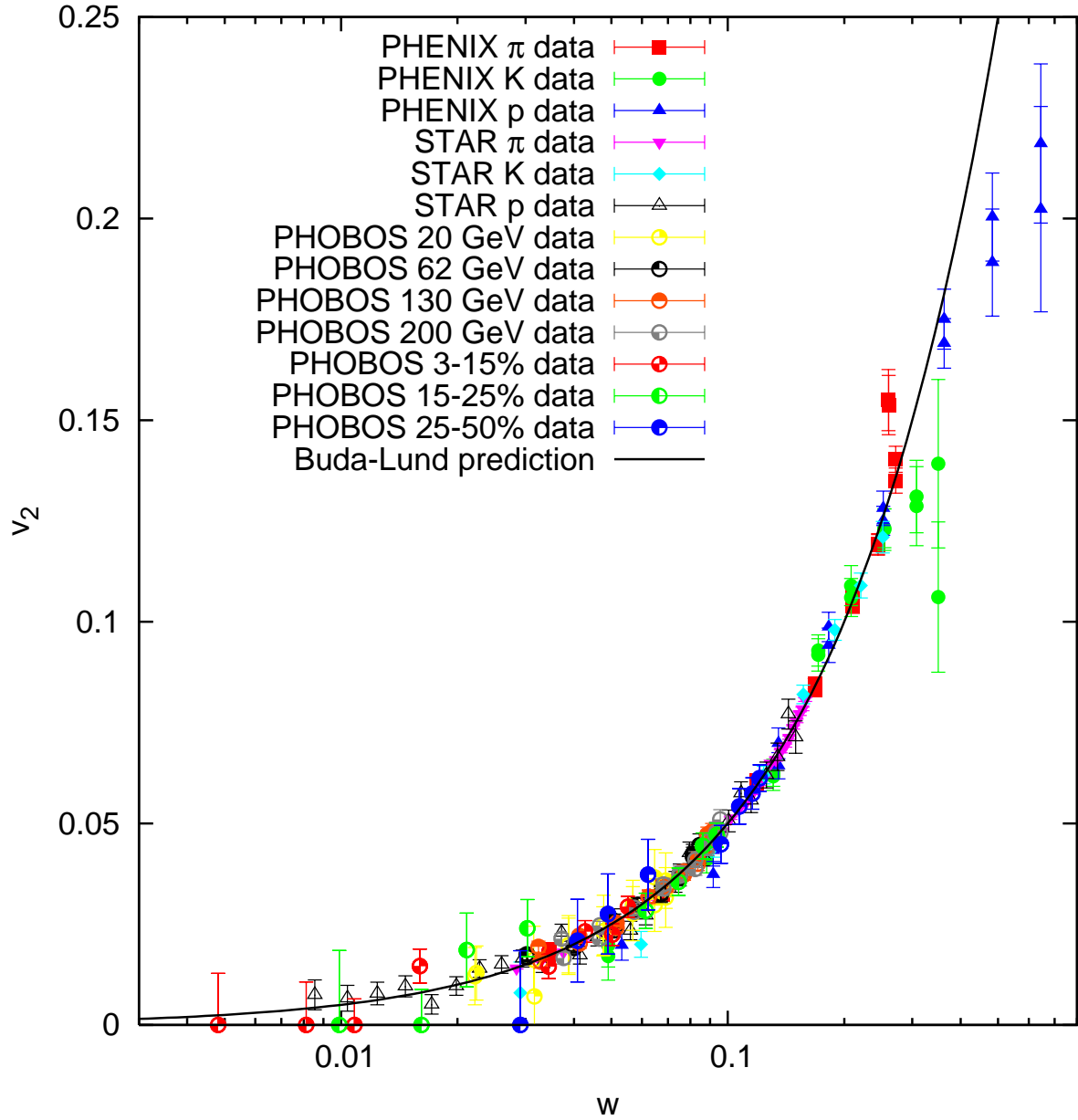
$$T_x = T_0 + \bar{m}_t \dot{X}^2 \frac{T_0}{T_0 + \bar{m}_t a^2}, \quad (9.46)$$

$$T_y = T_0 + \bar{m}_t \dot{Y}^2 \frac{T_0}{T_0 + \bar{m}_t a^2}. \quad (9.47)$$

Here $a^2 = \langle \frac{\Delta T}{T} \rangle$ measures the transverse temperature inhomogeneity of the particle emitting source in the transverse direction at the mean freeze-out time.

We note, that each of the kinetic energy term, the effective temperature T_* and the eccentricity ε are transverse mass and rapidity dependent factors. However, for $\bar{m}_t a^2 \gg T_0$, T_x and T_y , hence ε and T_* become independent of transverse mass and rapidity. This saturation of the slope parameters happens only if the temperature is inhomogeneous, ie $a^2 > 0$.

The above structure of w , the variable of the universal scaling function of elliptic flow suggests that the transverse momentum, rapidity, particle type, centrality, colliding energy, and colliding system dependence of the elliptic flow is only apparent in perfect fluid hydrodynamics: a data collapsing behavior sets in and a universal scaling curve emerges, which

Figure 9.1: Elliptic flow versus w

Elliptic flow data of previous plots versus variable w is shown: Data points show the predicted [50] universal scaling. Small scaling violations at large w values correspond to $v_2(p_t)$ data for $p_t > 2$ GeV.

coincides with the ratio of the first and zeroth order modified Bessel functions [39,50], when v_2 is plotted against the scaling variable w .

Interesting is furthermore, that the Buda-Lund hydro model also predicts the following universal scaling laws and relationships for higher order flows [50]: $v_{2n} = I_n(w)/I_0(w)$ and $v_{2n+1} = 0$. This is to be tested in a further analysis.

9.5 Comparison to experimental data

We emphasize first, that the scaling variable w is expressed in eq. 9.41 in terms of measurable factors. The elliptic flow v_2 is also directly measurable. Hence the universal scaling prediction, eq. 9.40 can in principle be subjected to a direct experimental test. Given the fact that such measurements were not yet published in the literature, we perform an indirect testing of the prediction, by determining the relevant parameters of the scaling variable w from an analysis of the transverse momentum and rapidity dependence of the elliptic flow in Au+Au collisions at RHIC.

Transverse momentum dependent elliptic flow data at mid-rapidity can be compared to the Buda-Lund result directly, as it was done in e.g. Ref. [50].

Eq. 9.40 depends, for a given centrality class, on rapidity y and transverse mass m_t . When comparing our result to $v_2(\eta)$ data of the PHOBOS Collaboration, we have performed a saddle point integration in the transverse momentum variable and performed a change of variables to the pseudo-rapidity $\eta = 0.5 \log(\frac{|p|+p_z}{|p|-p_z})$, similarly to Ref. [74]. This way, we have evaluated the single-particle invariant spectra in terms of the variables η and ϕ , and calculated $v_2(\eta)$ from this distribution, a procedure corresponding to the PHOBOS measurement described in Ref. [65].

Scaling implies data collapsing behavior, and also is reflected in a difficulty in extracting the precise values of these parameters from elliptic flow measurements: due to the data collapsing behavior, some combinations of these fit parameters become relevant, other combinations become irrelevant quantities, that cannot be determined from measurements. This is illustrated in fig. 9.1, where we compare the universal scaling law of eq. 9.40 with elliptic flow measurements at RHIC. This figure shows an excellent agreement between data and prediction. We may note the small scaling violations at largest w values, that correspond to

elliptic flow data taken in the transverse momentum region of $p_t > 2$ GeV.

The observed scaling itself shows, that only a few relevant combinations of T_0 , a^2 , \dot{X}^2 , \dot{Y}^2 determine the transverse momentum dependence of the v_2 measurements. Hence from these measurements it is not possible to reconstruct all these four source parameters uniquely. We have chosen the following to eq. 9.40 approximative formulas to describe the scaling of the elliptic flow:

$$w(\eta) = \frac{2A}{\cosh(B\eta)}, \text{ and} \quad (9.48)$$

$$w(p_t) = A' \frac{p_t^2}{4m_t} (1 + B'(m_t - m)), \quad (9.49)$$

and for small values of w eq. 9.40 simplifies to $v_2 \approx w/2$. The coefficients are as follows:

$$A = \frac{E_K}{2T_*} \varepsilon \Big|_{m_t=\langle m_t \rangle, y=0} \quad (9.50)$$

$$B = \left(1 + \Delta\eta \frac{m_t}{T_0} \right)^{-1} \Big|_{m_t=\langle m_t \rangle, y=0} \quad (9.51)$$

$$A' = \frac{2\varepsilon}{T_*} \Big|_{m_t=m, y=0} \quad (9.52)$$

$$B' = -\frac{1}{m} \frac{T_0}{T_0 + ma^2} \left(1 - 2\frac{T_0}{T_*} \right) \Big|_{m_t=m, y=0} \quad (9.53)$$

From this simple picture we had to deviate a little bit in case of proton $v_2(p_t)$ data, here only one parameter could have been used to find a valid Minit minimum, so we fixed B' there. In addition, for pion $v_2(p_t)$ data we had to introduce a third term, $C'(m_t - m)^2$, as the data were more detailed here. This parameter can be expressed from the Buda-Lund model as

$$\begin{aligned} C' &= \frac{1}{m} \left(\frac{T_0}{T_0 + ma^2} \right)^5 \frac{1}{T_x^2 T_y^2} \Big|_{m_t=m, y=0} \times \\ &\times \left[(\dot{X}^2 + a^2 + \dot{Y}^2)(T_0 + ma^2)^3 + \right. \\ &+ m \dot{X}^2 \dot{Y}^2 \left(m^2 (\dot{X}^2 \dot{Y}^2 + a^2 (\dot{X}^2 + \dot{Y}^2)) \right) \\ &\left. - 3m \dot{X}^2 \dot{Y}^2 T_0 (T_0 + ma^2) \right]. \end{aligned} \quad (9.54)$$

For the analysis of the PHOBOS $v_2(\eta)$ measurements at RHIC, we have excluded points with large rapidity from lower center of mass energies $v_2(\eta)$ fits ($\eta > 4$ for 19.6 GeV, $\eta > 4.5$ for 62.4 GeV). Points with large transverse momentum ($p_t > 2.0$ GeV) were excluded from

PHENIX and STAR $v_2(p_t)$ fits. These values give a hint at the boundaries of the validity of the model.

Fits to PHOBOS [65,66], PHENIX [13] and STAR [67] data are shown in figs. 9.2 and 9.3. The values of the parameters and the quality of the fits are summarized in table 9.1.

Thus we have shown that the excitation function of the transverse momentum and pseudorapidity dependence of the elliptic flow in Au+Au collisions is well described with the formulas that are predicted by the Buda-Lund type of hydrodynamical calculations. We have provided a quantitative evidence for the validity of the perfect fluid picture of soft particle production in Au+Au collisions at RHIC up to 1-1.5 GeV but also show here that this perfect fluid extends far away from mid-rapidity, up to a pseudorapidity of $\eta_{\text{beam}} - 0.5$.

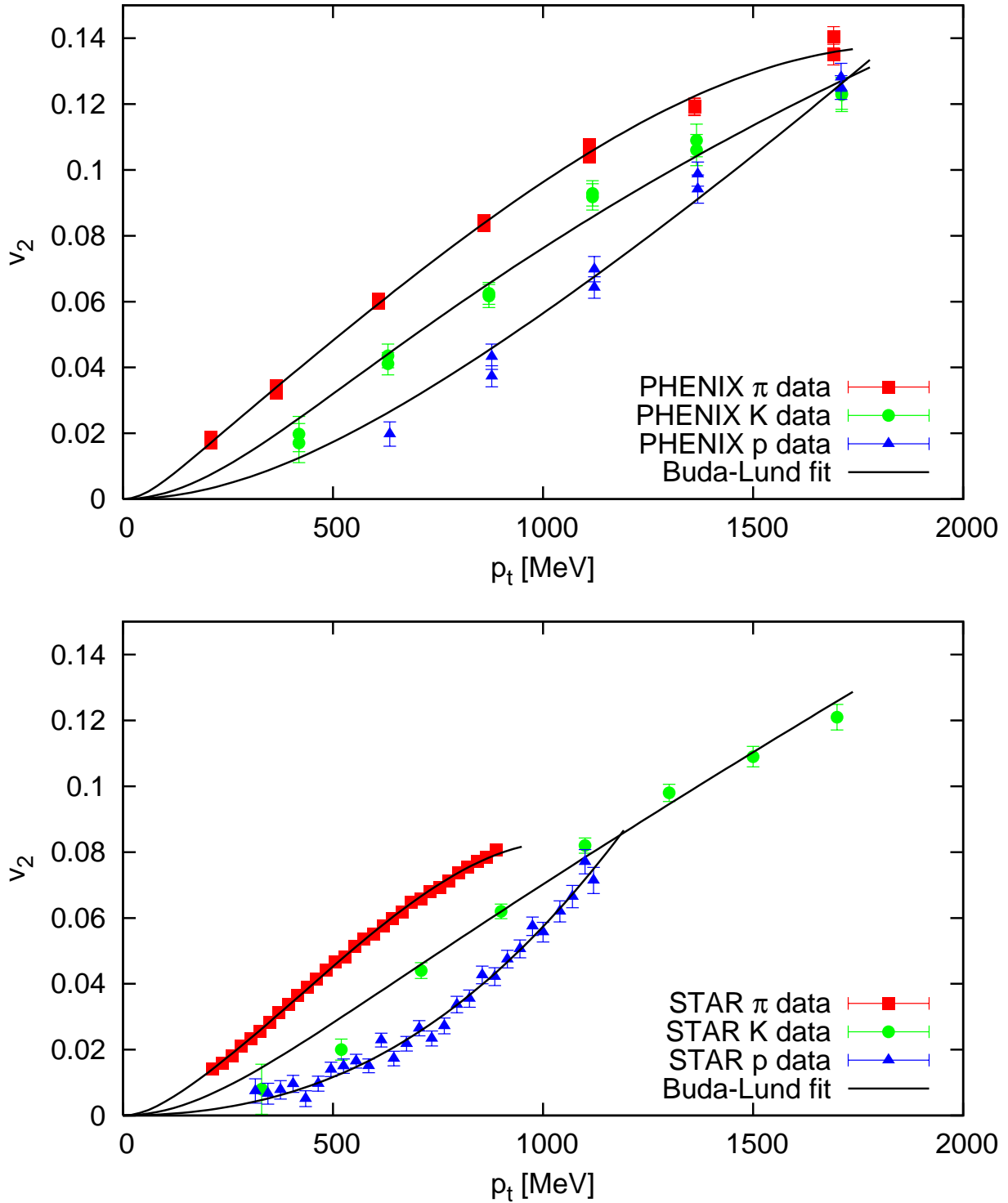
The universal scaling of PHOBOS $v_2(\eta)$ and PHENIX and STAR $v_2(p_t)$, expressed by eq. 9.40 and illustrated by fig. 9.1 provides a successful quantitative as well as qualitative test for the appearance of a perfect fluid in Au+Au collisions at various colliding energies at RHIC.

We also have shown, that at mid-rapidity and for a leading order approximation, $E_K \approx m_t - m$, which also explains recent development on scaling properties of v_2 by the PHENIX experiment.

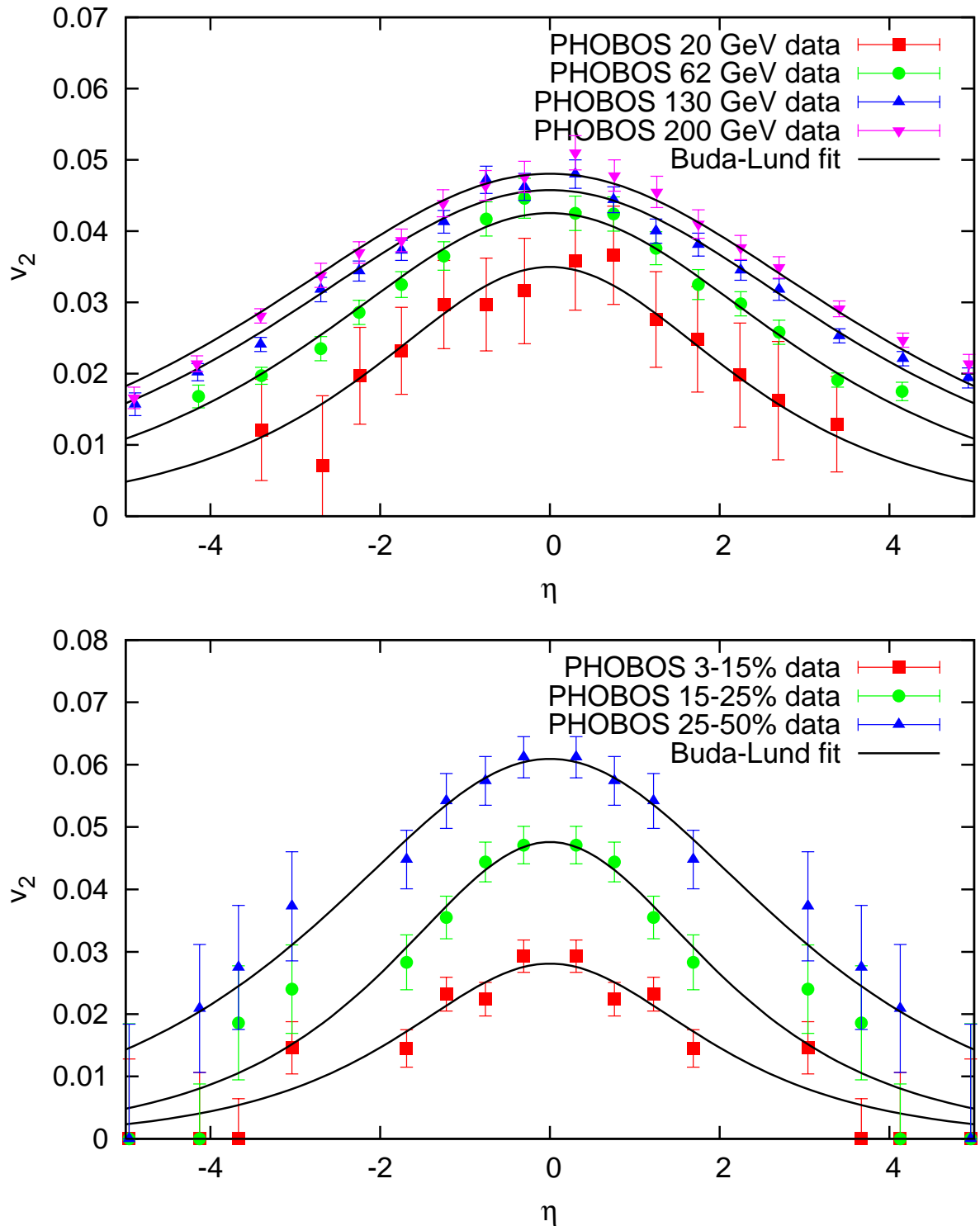
$v_2(\eta)$	20GeV	62GeV	130GeV	200GeV
A	0.035 ± 0.004	0.043 ± 0.001	0.046 ± 0.001	0.048 ± 0.001
B	0.53 ± 0.1	0.41 ± 0.01	0.34 ± 0.01	0.33 ± 0.01
χ^2/N_{DF}	1.7/11	9.3/13	17/15	18/15
CL	91%	74%	30%	28%
$v_2(\eta)$	3-15%	15-25%	25-50%	
A	0.028 ± 0.002	0.048 ± 0.002	0.061 ± 0.002	
B	0.64 ± 0.08	0.60 ± 0.06	0.43 ± 0.04	
χ^2/N_{DF}	12/13	8/13	4/13	
CL	51%	84%	96%	
$v_2(p_t)$	π	K	p	
A' [$10^{-4}/\text{MeV}$]	5.4 ± 0.1	6.4 ± 0.3	3.0 ± 0.1	
B' [$10^{-4}/\text{MeV}$]	16 ± 1	-0.2 ± 0.4	25, fixed	
C' [$10^{-6}/\text{MeV}^2$]	-1.5 ± 0.1	—	—	
χ^2/N_{DF}	96/27	17/5	27/26	
CL	$1\times 10^{-7}\%$	0.5%	40%	
$v_2(p_t)$	π	K	p	
A' [$10^{-4}/\text{MeV}$]	7.8 ± 0.2	7.4 ± 0.3	5.8 ± 0.1	
B' [$10^{-4}/\text{MeV}$]	1.4 ± 0.6	-1.3 ± 0.4	1.6, fixed	
C' [$10^{-6}/\text{MeV}^2$]	-1.6 ± 0.3	—	—	
χ^2/N_{DF}	21/10	13/9	17/7	
CL	2%	15%	2%	

Table 9.1: Elliptic flow fit results from the Buda-Lund model

Values of the parameters and the quality of the fits for collision energy dependent PHOBOS $v_2(\eta)$ data [65] is shown in the top table, the same for centrality dependent PHOBOS $v_2(\eta)$ data [66] in the second table. The third shows STAR [67], the fourth PHENIX [13] $v_2(p_t)$ data results.

Figure 9.2: PHENIX and STAR $v_2(p_t)$

PHENIX [13] and STAR [67] data on elliptic flow, v_2 , plotted versus p_t and fitted with Buda-Lund model.

Figure 9.3: PHOBOS $v_2(\eta)$

PHOBOS [65, 66] data on elliptic flow, v_2 , plotted versus η and fitted with Buda-Lund model.

Chapter 10

Correlation functions from the Buda-Lund model

10.1 The correlation function

In this chapter calculate rapidity dependent HBT (Bose-Einstein) radii in the framework of the model and make prediction on the universal scaling of these observables.

Our tool in describing the transverse momentum and pseudorapidity-dependence of correlations and the HBT radii is the ellipsoidal Buda-Lund hydrodynamical model, see Chapter 8 of present PhD thesis.

Let us calculate the two-particle Bose-Einstein correlation function (defined in eq. 5.23) from the saddle-point approximated source function (defined in eq. 8.34) of the Buda-Lund model! The correlation function can be then calculated using the core-halo model of Section 5.6 as

$$C(q, p) = 1 + \left| \frac{\tilde{S}(q, p)}{\tilde{S}(0, p)} \right|^2 = 1 + \lambda_* \left| \frac{\tilde{S}_c(q, p)}{\tilde{S}_c(0, p)} \right|^2, \quad (10.1)$$

with average momentum of the pair being $p = (p_1 + p_2)/2$ and their momentum-difference being $q = (p_1 - p_2)/2$. The quantities with $\tilde{}$ mean the Fourier-transformed, i.e.

$$\tilde{S}(q, p) = \int S(x, p) e^{iqx} d^4x, \quad \text{and} \quad (10.2)$$

$$\tilde{S}_c(q, p) = \int S_c(x, p) e^{iqx} d^4x. \quad (10.3)$$

From here on, we suppress the dependence on the average momentum of the pair p . The result for the correlation function can be obtained easily from eq. 8.34, the result is

$$C(q) = 1 + \lambda_* e^{-R_{\mu\nu}^2 q^\mu q^\nu}. \quad (10.4)$$

Let us from now on concentrate the physically interesting case of eq. 8.48, when the expansion is predominantly longitudinal. So, let us consider the case, when the emission function is characterized in terms of the variables (τ, η, r_x, r_y) , similarly to the axially symmetric case of the Buda-Lund model. If we solve the saddle-point equations in the $r_{x,s}/X \ll 1$, $r_{y,s}/Y \ll 1$, and $\eta_s - y \ll \Delta\eta = \dot{Z}$ limit (or make a Gaussian approximation of eq. 10.4), then the correlation function has the following diagonal form (for the radii, see eqs. 8.51-8.52):

$$C(q) = 1 + \lambda_* e^{-q_\tau^2 \Delta\tau_*^2 - q_x^2 R_{*,x}^2 - q_y^2 R_{*,y}^2 - q_\eta^2 \tau_0^2 \Delta\eta_*^2}. \quad (10.5)$$

Then we go over from coordinates q_τ and q_η to $q_t = q_0$ and q_z :

$$q_\tau = q_0 \cosh \eta_s - q_z \sinh \eta_s, \quad (10.6)$$

$$q_\eta = -q_0 \sinh \eta_s + q_z \cosh \eta_s, \quad (10.7)$$

with negligible second order corrections. From the mass-shell constraint of $p_1^2 = p_2^2 = m^2$ one finds that

$$q_0 = \beta_x q_x + \beta_y q_y + \beta_z q_z. \quad (10.8)$$

Thus we can rewrite eq. 10.4 to

$$C(q) = 1 + \lambda_* \exp \left(- \sum_{i,j=x,y,z} R_{i,j}^2 q_i q_j \right) \quad (10.9)$$

with the modified radii of

$$R_x^2 = R_{*,x}^2 + \beta_x^2 (\Delta\tau_*^2 \cosh \eta_s^2 + \tau_0^2 \Delta\eta_*^2 \sinh \eta_s^2), \quad (10.10)$$

$$R_y^2 = R_{*,y}^2 + \beta_y^2 (\Delta\tau_*^2 \cosh \eta_s^2 + \tau_0^2 \Delta\eta_*^2 \sinh \eta_s^2), \quad (10.11)$$

$$R_z^2 = \Delta\tau_*^2 (\sinh \eta_s - \beta_z \cosh \eta_s)^2 + \tau_0^2 \Delta\eta_*^2 (\cosh \eta_s - \beta_z \sinh \eta_s)^2, \quad (10.12)$$

$$\begin{aligned} 2R_{x,z}^2 &= -(\Delta\tau_*^2 + \tau_0^2 \Delta\eta_*^2) \beta_x \cosh \eta_s \sinh \eta_s + \\ &+ \beta_x \beta_z (\Delta\tau_*^2 \cosh \eta_s^2 + \tau_0^2 \Delta\eta_*^2 \sinh \eta_s^2), \end{aligned} \quad (10.13)$$

$$\begin{aligned} 2R_{y,z}^2 &= -(\Delta\tau_*^2 + \tau_0^2 \Delta\eta_*^2) \beta_y \cosh \eta_s \sinh \eta_s + \\ &+ \beta_y \beta_z (\Delta\tau_*^2 \cosh \eta_s^2 + \tau_0^2 \Delta\eta_*^2 \sinh \eta_s^2), \end{aligned} \quad (10.14)$$

$$2R_{x,y}^2 = \beta_x \beta_y (\Delta\tau_*^2 \cosh \eta_s^2 + \tau_0^2 \Delta\eta_*^2 \sinh \eta_s^2). \quad (10.15)$$

Then we make the coordinate-transformation from the system of ellipsoidal expansion to the laboratory frame, where the observables are measured (by angle ϑ , see Section 9.3 of present PhD thesis), and then to the Bertsch-Pratt frame [75] (by angle φ) of out (o , pointing towards the average momentum of the actual pair), longitudinal (l , pointing towards the beam direction) directions and side (s , perpendicular to both l and o) directions, see fig. 10.1:

$$q_x = q'_x \cos \vartheta - q'_z \sin \vartheta = q'_o \cos \varphi \cos \vartheta - q'_s \sin \varphi \cos \vartheta - q'_l \sin \vartheta, \quad (10.16)$$

$$q_y = q'_y = q'_s \cos \varphi + q'_o \sin \varphi, \quad (10.17)$$

$$q_z = q'_z \cos \vartheta + q'_x \sin \vartheta = q'_l \cos \vartheta + q'_o \cos \varphi \sin \vartheta - q'_s \sin \varphi \sin \vartheta. \quad (10.18)$$

After that, we get the following radii:

$$R_o'^2 = R_x'^2 \cos^2 \varphi + R_y'^2 \sin^2 \varphi + R_{x,y}'^2 \sin(2\varphi), \quad (10.19)$$

$$R_s'^2 = R_x'^2 \sin^2 \varphi + R_y'^2 \cos^2 \varphi - R_{x,y}'^2 \sin(2\varphi), \quad (10.20)$$

$$R_l'^2 = R_x'^2 \sin^2 \vartheta + R_z'^2 \cos^2 \vartheta - R_{x,z}'^2 \sin(2\vartheta), \quad (10.21)$$

$$2R_{o,s}'^2 = -R_x'^2 \sin(2\varphi) + R_y'^2 \sin(2\varphi) - 2R_{x,y}'^2 \cos(2\varphi), \quad (10.22)$$

$$2R_{s,l}'^2 = (R_x'^2 \sin(2\vartheta) - R_z'^2 \sin(2\vartheta) - 2R_{x,z}'^2 \cos(2\vartheta)) \sin \varphi - \\ - (2R_{x,y}'^2 \sin \vartheta - 2R_{y,z}'^2 \cos \vartheta) \sin \varphi, \quad (10.23)$$

$$2R_{l,o}'^2 = (R_z'^2 \sin(2\vartheta) - R_x'^2 \sin(2\vartheta) + 2R_{x,z}'^2 \cos(2\vartheta)) \cos \varphi - \\ - (2R_{x,y}'^2 \sin \vartheta - 2R_{y,z}'^2 \cos \vartheta) \sin \varphi, \quad (10.24)$$

if we introduce

$$R_x'^2 = R_x^2 \cos^2 \vartheta + R_z^2 \sin^2 \vartheta + 2R_{x,z}^2 \cos \vartheta \sin \vartheta, \quad \text{and} \quad (10.25)$$

$$R_{x,y}'^2 = R_{x,y}^2 \cos \vartheta + R_{y,z}^2 \sin \vartheta \quad (10.26)$$

In the LCMS frame, where $\beta_z = \beta_y = 0$:

$$R_o^2 = R_x^2 \cos^2 \varphi + R_y^2 \sin^2 \varphi, \quad (10.27)$$

$$R_s^2 = R_x^2 \sin^2 \varphi + R_y^2 \cos^2 \varphi, \quad (10.28)$$

$$R_l^2 = R_x^2 \sin^2 \vartheta + R_z^2 \cos^2 \vartheta - 2R_{x,z}^2 \sin \vartheta \cos \vartheta, \quad (10.29)$$

$$2R_{o,s}^2 = (R_y^2 - R_x^2) \sin 2\varphi \quad (10.30)$$

$$2R_{s,l}^2 = -(R_z^2 \sin 2\vartheta - R_x^2 \sin 2\vartheta + 2R_{x,z}^2 \cos 2\vartheta) \sin \varphi, \quad (10.31)$$

$$2R_{l,o}^2 = +(R_z^2 \sin 2\vartheta - R_x^2 \sin 2\vartheta + 2R_{x,z}^2 \cos 2\vartheta) \cos \varphi. \quad (10.32)$$

I computed also the transverse mass (m_t) sensitivity of the HBT radii in this latter simple case (see equations 10.27-10.32), for the parameter set obtained in ref [50]. The plots are shown in figure 10.2.

10.2 Rapidity dependent HBT radii

In the framework of the model we can also calculate the rapidity dependence of the HBT radii. From eqs. 10.27-10.32 the simplest case, where system of ellipsoidal expansion equals

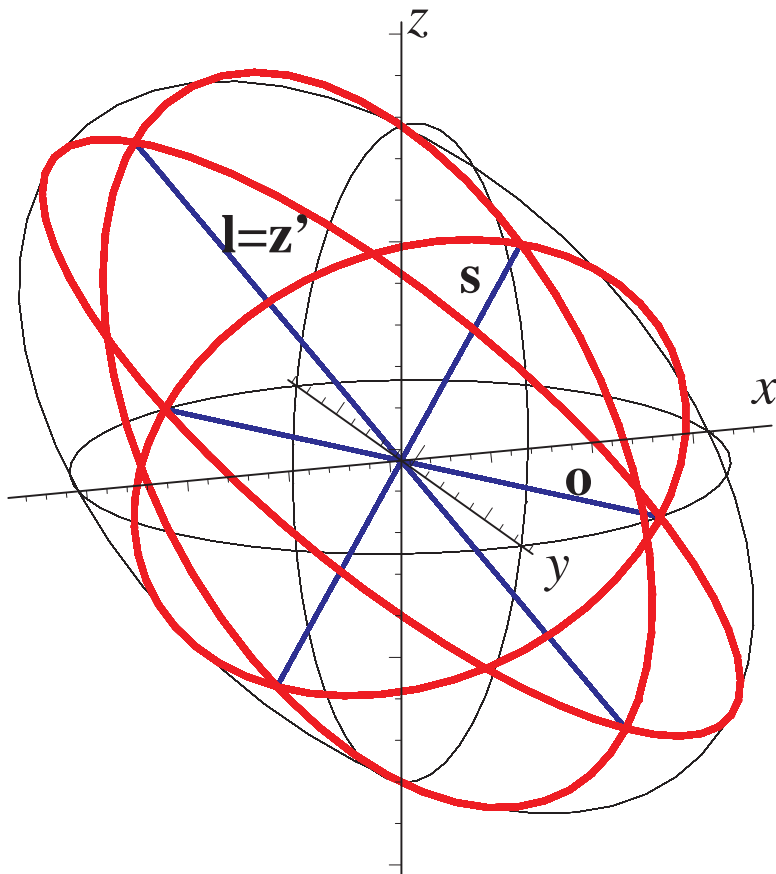


Figure 10.1: The coordinate transformation

The old coordinate system (x, y, z) is shown with thin lines, the new (after two coordinate-transformations) $(\mathbf{o}, \mathbf{s}, \mathbf{l})$ with thick lines. The axes of the new coordinate system are the main axes of the ellipsoid. The angle between axes z and $l = z'$ is ϑ , angle φ is not explicitly shown as it is the angle between x and the intermediate coordinate system of x' . The ellipsoid is drawn with thick lines. Its sections with the xy , yz and zx coordinate planes are drawn with thin lines. The ratio of the three main axes are in this case $3 : 4 : 5$, while $\vartheta = \pi/5$ and $\varphi = \pi/4$.

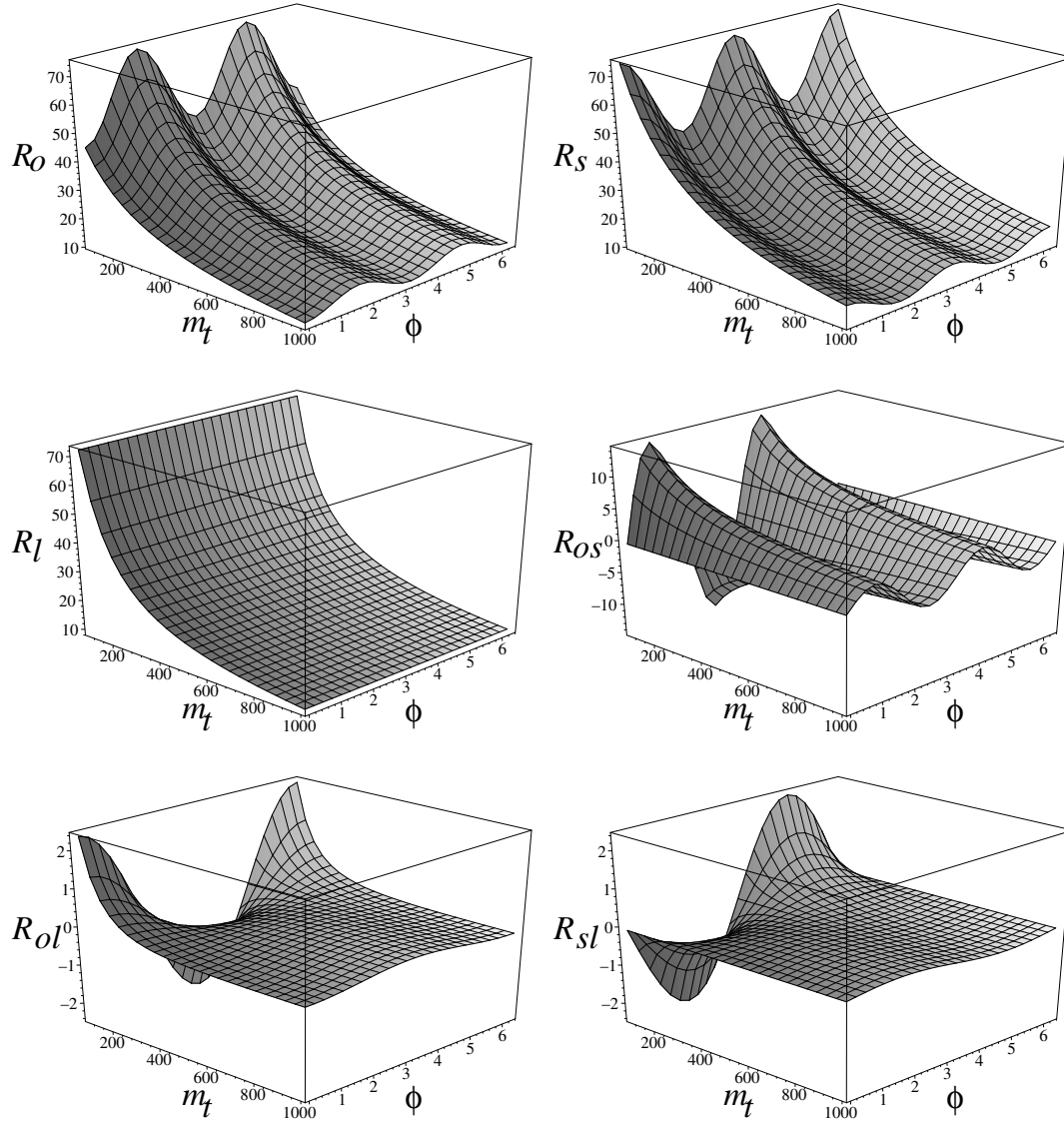


Figure 10.2: Transverse mass dependence of the HBT radii

On these figures, we see the transverse mass (m_t) and azimuthal angle (φ) dependence of the HBT radii. The period in R_O , R_S and $R_{O,S}$ is π , in $R_{S,l}$ and $R_{l,O}$ it is 2π , and R_l does not depend on φ , as it is shown in equations 10.27-10.32.

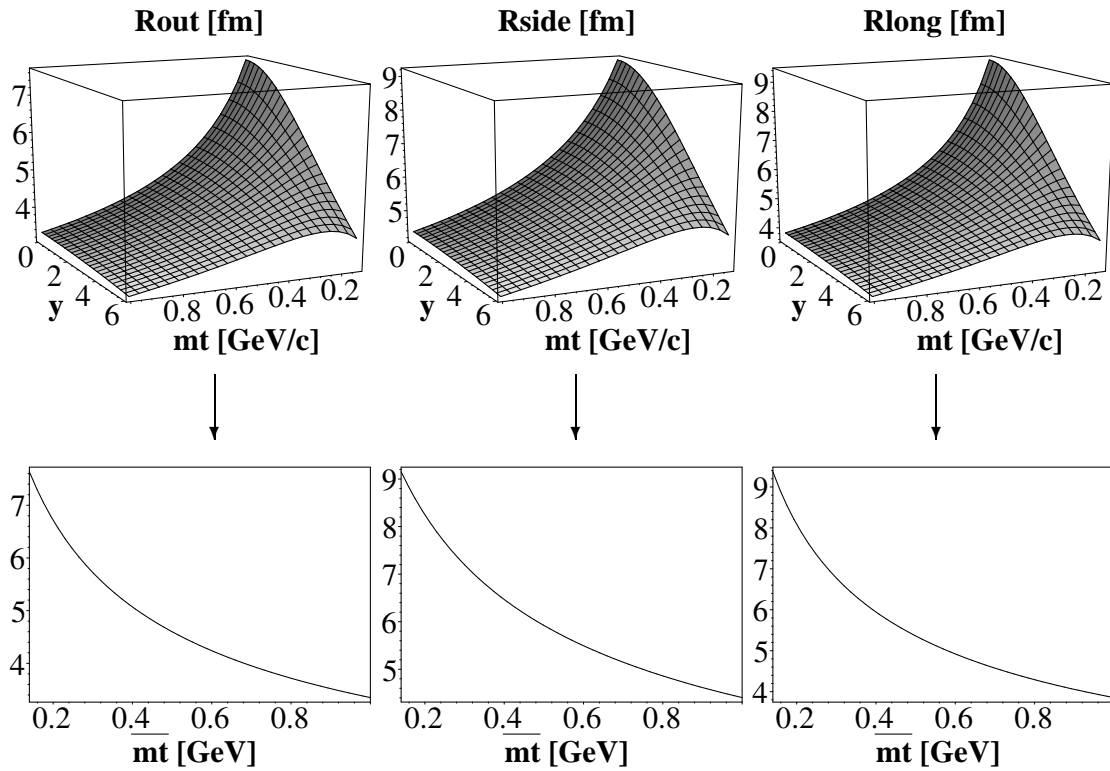
the out-side-longitudinal coordinate system:

$$R_{\text{out}}^2 = X^2 \left(1 + \frac{\bar{m}_t (a^2 + \dot{X}^2)}{T_0} \right)^{-1}, \quad (10.33)$$

$$R_{\text{side}}^2 = Y^2 \left(1 + \frac{\bar{m}_t (a^2 + \dot{Y}^2)}{T_0} \right)^{-1}, \quad (10.34)$$

$$R_{\text{long}}^2 = Z^2 \left(1 + \frac{\bar{m}_t (a^2 + \dot{Z}^2)}{T_0} \right)^{-1}. \quad (10.35)$$

This means, that the HBT radii depend on transverse mass and rapidity only through the scaling parameter \bar{m}_t , as illustrated on fig. 10.3. This behavior could easily be checked by measurement of rapidity and transverse momentum dependence of the HBT radii and comparing this data to the present prediction of the Buda-Lund model. Such a comparison could be a further test of perfect fluid hydrodynamics.

Figure 10.3: HBT radii versus η

Upper panel: R_{out} , R_{side} and R_{long} as a function of rapidity y and transverse mass m_t . Lower panel: The two-dimensional $R(m_t, y)$ functions are predicted to show a scaling behavior, insofar as they depend only on scaling variable \overline{m}_t .

Chapter 11

From Quark Gluon Plasma to a Perfect Fluid of Quarks

*Gray, my dear friend, is every theory,
And green alone life's golden tree*

FAUST, GOETHE

11.1 Perfect fluids at RHIC

11.1.1 A sign for hydrodynamic behavior: elliptic flow

Azimuthal asymmetry of single particle spectra measured in relativistic heavy ion collisions is called elliptic flow (v_2). It is an indication of liquid-like behavior [13], and can be explained by hydrodynamics [50, 76, 77]. In the hydrodynamic picture it turns out, that elliptic flow can result from the initial spatial asymmetry but also from momentum-space asymmetry. Important is, that in contrast to a uniform distribution of particles expected in a gas-like system, this liquid behavior means that the interaction in the medium of these copiously produced particles is rather strong, as one expects from a fluid. Detailed investigation of these phenomena suggests that this liquid flows with almost no viscosity [14].

11.1.2 Relativistic perfect fluids

Perfect hydrodynamics is based only on local conservation of charge and energy-momentum and on the assumption of local thermal equilibrium, and this is the tool that we use to describe and calculate the properties of the matter created in relativistic heavy ion collisions at RHIC. While there are accelerating non-relativistic solutions in the literature, recent development shows also relativistic solutions that can be compared to the data [61, 78].

Local conservation of charge and four-momentum reads as

$$\partial_\nu(nu^\nu) = 0, \quad (11.1)$$

$$\partial_\nu T^{\mu\nu} = 0, \quad (11.2)$$

$$T^{\mu\nu} = (\varepsilon + p)u^\mu u^\nu - pg^{\mu\nu}. \quad (11.3)$$

We find the following new solution (for arbitrary λ in $d = 1$, $\kappa = 1$ and for $\lambda = 2$ in arbitrary d with $\kappa = d$) [61]:

$$v = \tanh \lambda\eta \quad (11.4)$$

$$n = n_0 \left(\frac{\tau_0}{\tau}\right)^{\lambda d} \nu(s), \quad (11.5)$$

$$T = T_0 \left(\frac{\tau_0}{\tau}\right)^{\lambda d/\kappa} \frac{1}{\nu(s)}, \quad (11.6)$$

where $\nu(s)$ is an arbitrary function of the scale variable s , and η is the pseudo-rapidity. As an illustration, fluid trajectories of this solution are shown on fig. 11.1.2. See details in ref. [61].

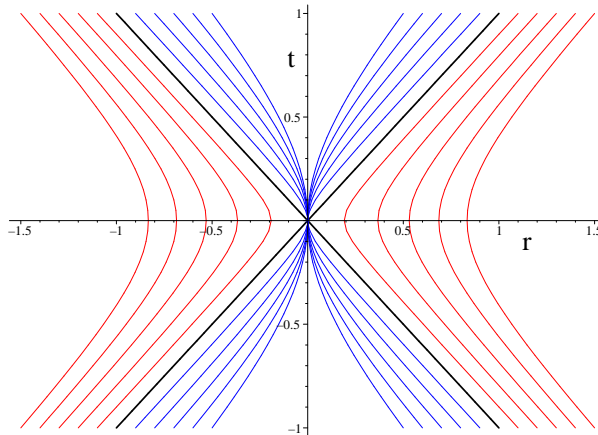


Figure 11.1: Fluid trajectories of the new solution

Fluid trajectories of the new exact solution of perfect fluid hydro are shown, corresponding to $d = 1$ and $\lambda = 2$. The trajectories are shown both inside and outside the lightcone.

11.2 Characterizing the matter produced at RHIC

11.2.1 An advanced estimate on the initial energy density

Based on the above solution of eqs. 11.4-11.6 let us estimate the initial energy density of relativistic heavy ion or p+p reactions. As our solution is an accelerating one, and we do not neglect the initial acceleration period, we improve the renowned Bjorken estimate both quantitatively and qualitatively. Similarly to Bjorken's method [79], we can estimate the initial energy density (see ref. [61] for details). Finally we get a correction to the widely used Bjorken formula, depending on the acceleration parameter (λ):

$$\frac{\varepsilon_0}{\varepsilon_{Bj}} = \frac{\alpha}{\alpha - 2} \left(\frac{\tau_f}{\tau_0} \right)^{1/(\alpha-2)} = (2\lambda - 1) \left(\frac{\tau_f}{\tau_0} \right)^{\lambda-1}, \quad (11.7)$$

The acceleration parameter can be extracted from the measured rapidity distribution [61]. For flat rapidity distributions, $\alpha \rightarrow \infty$ ($\lambda \rightarrow 1$, i.e. no acceleration) and the Bjorken estimate is recovered. For $\lambda > 1$, the correction factor is bigger than 1. Hence we conclude that the initial energy densities are under-estimated by the Bjorken formula. For realistic RHIC data from BRAHMS [80], the correction factor can be as big as $\varepsilon/\varepsilon_{Bj} \approx 2.2$ [61]. Thus smaller initial bombarding (or colliding) energies are needed to reach the critical energy density in high energy heavy ion collisions, than thought previously using Bjorken's renowned formula.

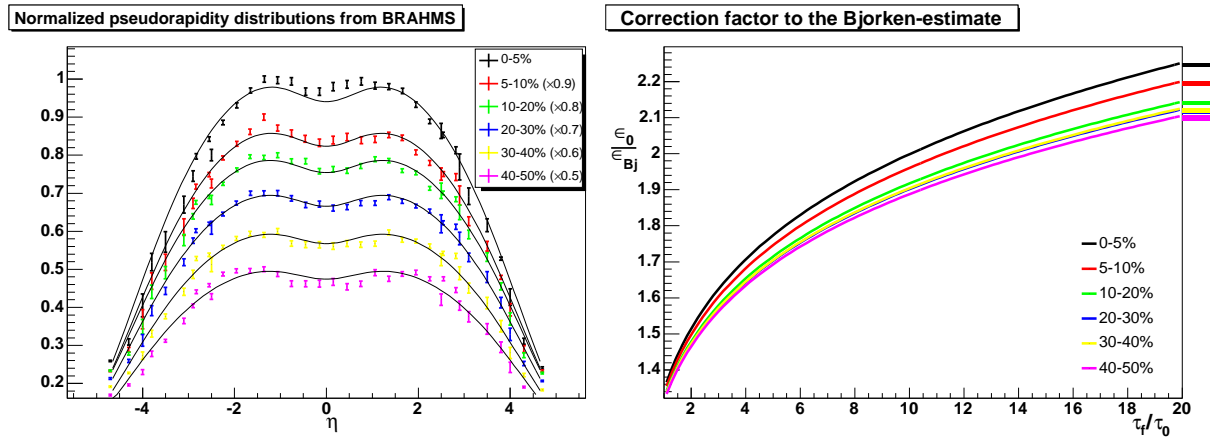


Figure 11.2: $\frac{dn}{d\eta}$ and resulting correction to the Bjorken-estimate

Left: charged particle $\frac{dn}{d\eta}$ distributions of ref. [80] fitted with the result of the relativistic hydro solution of ref. [61]. Right: the correction parameter (obtained from fits show on the left panel) as a function of freeze-out time versus thermalization time (τ_f/τ_0). At reasonable values of 10-15, the correction to the Bjorken estimate of energy density is a factor of ~ 2 .

11.2.2 Estimating the freeze-out temperature

According to recent lattice QCD calculations, at the at RHIC observed small μ_B chemical potentials, the transition from confined to deconfined matter is a cross-over [47]. For more details, see subsection 8.1.2 of Chapter 8.

We estimated the freeze-out temperature of these Little Bangs, fitting data to the Buda-Lund hydro model of Chapter 8 of present PhD thesis and refs. [40, 50]. The result of the Buda-Lund fits to RHIC Au+Au data of refs. [34, 38, 80–85] (shown on fig. 11.3), in particular the value of the fit parameter T_0 (central freeze-out temperature, see details in ref. [49]), indicates the existence of a region several standard deviations hotter than the critical temperature. This is an indication on quark deconfinement in Au + Au collisions with $\sqrt{s_{NN}} = 130$ and 200 GeV at RHIC [41, 42, 49], confirmed by the analysis of p_t and η dependence of the elliptic flow [50]. A similar analysis of Pb+Pb collisions at CERN SPS energies yields central temperatures lower than the critical value, $T_0 < T_c$ [44, 45].

11.2.3 Universal scaling of the elliptic flow

The Buda-Lund calculation of the elliptic flow results (under certain conditions detailed Chapter 9 and in ref. [50]) in the simple universal scaling law expressed in eq. 9.40.

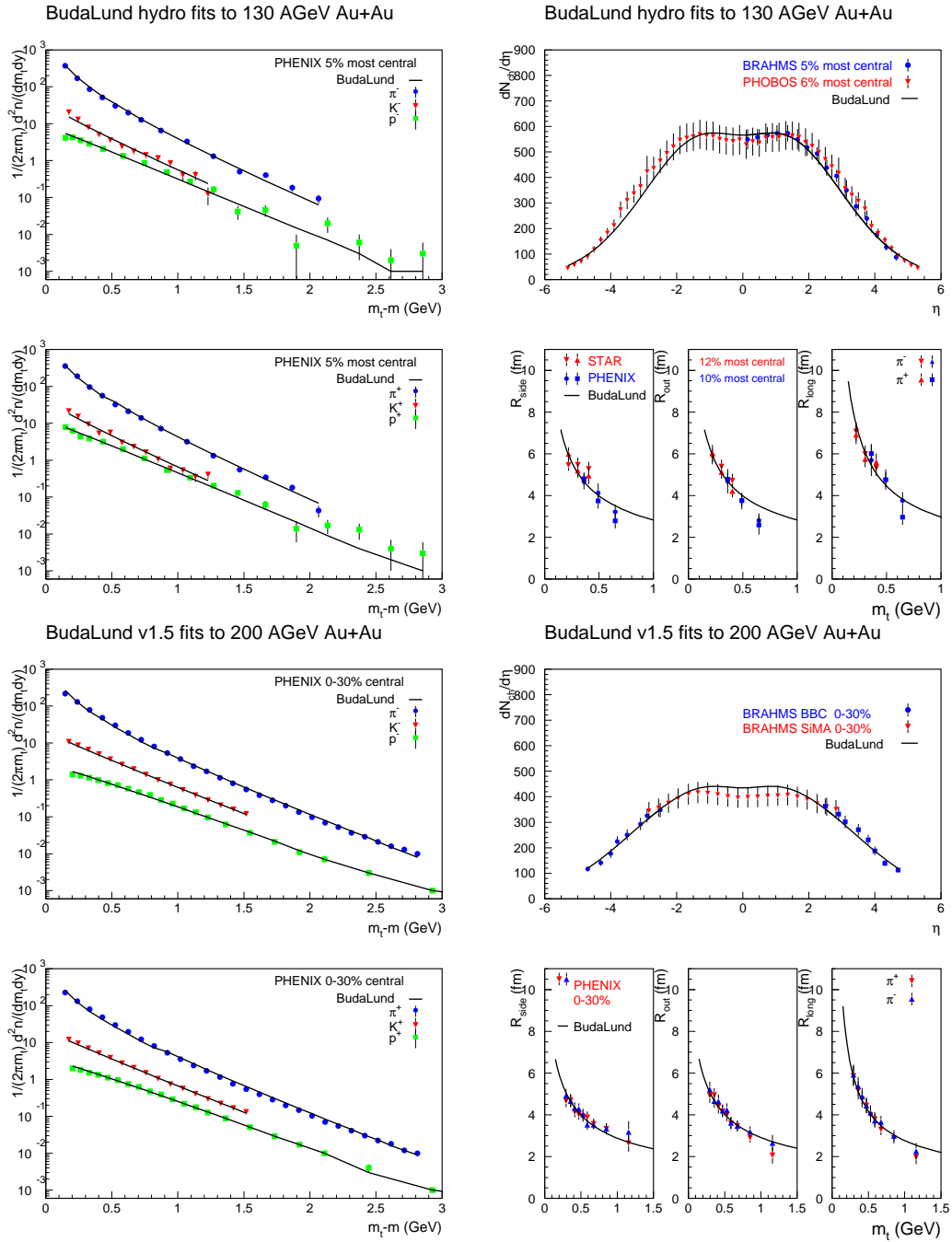


Figure 11.3: Fits to RHIC $\sqrt{s_{NN}} = 130$ and 200 GeV data

The upper four panels show a simultaneous Buda-Lund fit to 0-5(6) % central Au+Au data at $\sqrt{s_{NN}} = 130$ GeV, refs. [81–85]. The lower four panels show similar fits to 0-30 % central Au+Au data at $\sqrt{s_{NN}} = 200$ GeV, refs. [34, 38, 80]. Note that the identified particle spectra are published in more detailed centrality classes, but we recombined the 0-30% most central collisions so that the fitted spectra and radii be obtained in the same centrality class. The fit parameters are summarized in ref. [50].

Thus the model predicts a *universal scaling*: every v_2 measurement is predicted to fall on the same *universal* scaling curve I_1/I_0 when plotted against the scaling variable w (see details in ref. [86] and in Chapter 8).

This means, that v_2 depends on any physical parameter (transverse or longitudinal momentum, center of mass energy, centrality, type of the colliding nucleus etc.) only through the (universal) scaling parameter w .

In ref. [86] we have shown that the excitation function of the transverse momentum and pseudorapidity dependence of the elliptic flow in Au+Au collisions (RHIC data from refs. [13,65,67]) is well described with the formulas that are predicted by the Buda-Lund type of hydrodynamical calculations. We have provided a quantitative evidence of the validity of the perfect fluid picture of soft particle production in Au+Au collisions at RHIC up to 1-1.5 GeV but also show here that this perfect fluid extends far away from mid-rapidity, up to a pseudorapidity of $\eta_{\text{beam}} - 0.5$. The universal scaling of PHOBOS $v_2(\eta)$ [65], PHENIX $v_2(p_t)$ [13] and STAR $v_2(p_t)$ [67], expressed by eq. 9.40 and illustrated by fig. 9.1 provides a successful quantitative as well as qualitative test for the appearance of a perfect fluid in Au+Au collisions at various colliding energies at RHIC.

11.2.4 Chiral symmetry restoration

Correlation functions are important to see the collective properties of particles and the space-time structure of the emitting source, e.g. the observed size of a system can be measured by two-particle Bose-Einstein correlations [22]. The m_t dependent strength of two-pion correlations, the so-called λ_* parameter, which is related to the extrapolated value of the correlation function at zero relative momentum, can be used to extract information on the mass-reduction of the η' meson, a signal of $U_A(1)$ symmetry restoration in the source [24–27].

PHENIX analyzed [87] $\lambda_*(m_t)$ with fits to two-pion correlation functions using three different shapes, Gauss, Levy and Edgeworth, as described in refs. [31,45,87] and in Section 5.8 of present PhD thesis. A comparison of the measurements with model calculations of ref. [24] using FRITIOF results for the composition of the long-lived resonances and a variation of the η' mass is presented in fig. 5.4. If we re-norm the $\lambda_*(m_t)$ curves with their maximal value on the investigated m_t interval, they overlap, confirming the existence and characteristics of the hole in the $\lambda_*(m_t)$ distribution.

Gauss fit results agree with former PHENIX measurements (see ref. [34]). Regarding $U_A(1)$ symmetry restoration, conclusion is that at present, results are critically dependent on the understanding of statistical and systematic errors, and additional analysis is required to make a definitive statement.

11.3 Summary of the results

In summary, we can make the definitive statement, based on elliptic flow measurements and the broad range success of analytic hydro models, that in relativistic Au+Au collisions observed at RHIC we see a perfect fluid. Based on our estimates on the temperature and energy density we also conclude that the observed matter is in a deconfined state. We also see a possible signal of partial symmetry restoration in the mass reduction of η' bosons. Future plan is to explore all properties of the Quark Matter, by analyzing more data and using higher luminosity. We are after the full map of the QCD phase diagram, and in order to explore it, we also have to go to higher energies and compare them to lower energy data. If the Quark Matter is the New World, then Columbus just realized he is not in India, but on a new continent.

Statement of Contributions

Here I summarize my own contributions to the present PhD thesis and my coauthored papers the thesis is based on.

1 Online monitoring of the ZDC and the SMD

The Zero Degree Calorimeter (ZDC) is a neutron detector of three modules, which is placed in the line where the two beams of RHIC cross each other. It measures the energy of the neutrons that evaporated from the spectators of the collision, as these are not deflected by the magnets that keep the ions on their track. Thus the ZDC enables the experiment to determine the centrality of the observed collisions, as this clearly effects the number of evaporated collisions. The ZDC is furthermore capable of determining the longitudinal position of the collision. The Shower Max Detector (SMD), placed between first two ZDC modules, measures the transverse distribution of the evaporated neutrons, thus the geometry of the beam. I automated these measurements and solved the real-time plotting and the database-storage of the results of them within the PHENIX Online Monitoring. [2, 3, 88–96]

2 Measurements and simulations with the ZDC

I determined the expected distribution of neutrons in the ZDC at RHIC and LHC energies with Pythia simulations. I measured in 200 GeV ultra-peripheral Au+Au collisions (characterized by impact parameters higher than the nucleus size) the production cross-section of J/Ψ particles in incoherent processes and of e^\pm pairs in coherent processes. Results are in agreement with theoretical predictions. [97, 98]

3 Partial coherence in Au+Au collisions at PHENIX

I measured two- and three-particle correlation functions in 200 GeV Au+Au collisions. I fitted these with calculated correlation functions using Gaussian, Lévy and Edgeworth shapes, and from this I determined the allowed region for the fraction of the hydrodynamically evolving core (f_c) and the fraction of a partially coherent part (p_c) within the core. Nonzero partial coherence is allowed when having larger core size than the one allowed at total incoherence ($p_c = 0$). [87, 99, 100]

4 Analysis of two-pion correlations

I measured the transverse momentum dependence of the strength of the two-pion correlation functions, as this provides information about a possible mass modification of the η' boson, the ninth Goldstone-boson. These measurements indicated a large decrease of the η' mass, i.e. a sign of $U_A(1)$ symmetry restoration in the source. [87, 99, 100]

5 Lévy-stability of the particle emitting source

I compared two-particle source functions measured in 200 GeV Au+Au collisions to Lévy-stable distributions, and measured the Lévy-stability exponent of the source (α), which corresponds to the critical exponent in a second order phase transition. I found, that the α parameter takes a value of around 1.4 ± 0.1 . In case of second order phase transitions this value was predicted to be maximally $\alpha=0.5$, which, based on this analysis, is not in agreement with the experimental data. [15, 101, 102]

6 Generalization of the Buda-Lund model

I generalized the Buda-Lund model for ellipsoidally symmetric fireballs arisen from high energy heavy ion collisions. I calculated the transverse momentum and rapidity dependence elliptic flow from the model, and found it to be in agreement with experimental data of peripheral Au+Au collisions at RHIC. With this comparison I confirmed the previously found indirect evidence for a deconfinement of quarks and gluons, based on the central temperature of the fireball compared to critical temperatures calculated from lattice QCD. I also found,

that the volume, where the temperature is higher than the critical one is approximately 1/8th of the total volume, however, the surface of the fireball is rather cold. [41, 42, 49, 103]

7 Correlations from the Buda-Lund model

I calculated the two-particle correlations from the generalized Buda-Lund model. I showed, that the transverse momentum and rapidity dependence of the HBT radii can be merged to a single scaling function. I also suggested a method for experimentally testing this scaling as a method of testing the validity of the perfect hydro picture at RHIC. [104, 105]

8 Scaling of the elliptic flow at RHIC

I calculated the elliptic flow from the generalized Buda-Lund model. I showed, that the elliptic flow depends on any physical parameter (transverse or longitudinal momentum, mass, center of mass energy, collision centrality, type of the colliding nucleus etc.) only through a scaling variable. I showed that this scaling is present in RHIC Au+Au data, and this provides a quantitative evidence for the validity of the perfect fluid picture of soft particle production in Au+Au collisions at RHIC up to transverse momenta of $\sim 1.0-1.5$ GeV and that this perfect fluid extends far away from mid-rapidity, up to a pseudorapidity of $\eta_{\text{beam}} - 0.5$. Finally I showed that the kinetic energy scaling of the elliptic flow found experimentally at PHENIX is a consequence of this universal scaling. [15, 86, 104, 106]

Acknowledgements

I would like to thank Tamás Csörgő, my supervisor, for teaching and guiding me, for talking about the important things which are not certainly part of physics, and for his constant support during my studies.

I am thankful to Ádám Kiss, who always helped me on my way to experience experimental and theoretical physics.

I would like to thank the PHENIX Collaboration, especially the Global/Hadron Working Group, Roy Lacey, Gábor Dávid and Péter Tarján for initiating me into the secrets of experimental physics, Sebastian White and Alexei Denisov for teaching me about ZDC and SMD. I would like to thank Bengt Lörstad for helping me out so many times when being lost in the labyrinth' of theoretical research.

I am also thankful to Ákos Horváth who gave a starting impulse by guiding me at my very first steps as a researcher.

Of course, I am grateful to my parents and grandparents for their patience, support and *love*. Without them this work would never have come into existence (literally).

My researches were supported by the US-Hungarian Fulbright Commission, by the Hungarian - US MTA OTKA NSF grant INT0089462 and by the OTKA grants T038406, T034269, T049466, by the NATO Collaborative Linkage Grant PST.CLG.980086 and by a KBN-OM Hungarian - Polish programme in S&T.

Budapest, Hungary

Csanád Máté

May 30, 2007

List of Figures

2.1	Arial view of RHIC	14
2.2	Detector arrangement in PHENIX during Run 7	22
3.1	Plan view of the collision region "beam's eye" view of the ZDC location	26
3.2	Sketch of a high energy heavy ion collision	27
3.3	ZDC main online monitor in a Au+Au run	32
3.4	ZDC main online monitor in a d+Au run	33
3.5	LED energy values versus event number	34
3.6	LED timing values versus event number	35
3.7	Expert plots in a Au+Au run	36
3.8	Expert plots in a Au+Au run	37
3.9	Expert plots in a Au+Au run	38
3.10	ZDC to BBC vertex in a Au+Au run	39
4.1	Beam and side view of the SMD within the ZDC modules	42
4.2	SMD energy distribution	44
4.3	Expert plots in a Au+Au run	46
4.4	Expert plots in a d+Au run	47
4.5	SMD position versus event number	48
4.6	Raw ADC value distributions in the north vertical SMD	49
4.7	LED energy in the SMD stripes in a Au+Au run	50
4.8	Vernier scan plots	51
5.1	Raw- and Coulomb-corrected correlation functions	63
5.2	Partial coherence versus core fraction	64

5.3	$\lambda(m_t)$, $R(m_t)$, $\alpha(m_t)$ and $\kappa_3(m_t)$ from Gauss, Levy and Edgeworth fits	65
5.4	Mass modification of η'	66
6.1	Iterative Lévy fit results for 0-20%, $0.2 \text{ GeV}/c < k_t < 0.36 \text{ GeV}/c$	70
6.2	Iterative Lévy fit results for 0-20%, $0.48 \text{ GeV}/c < k_t < 0.6 \text{ GeV}/c$	71
6.3	Iterative Lévy fit results for 40-90%, $0.2 \text{ GeV}/c < k_t < 0.4 \text{ GeV}/c$	71
6.4	Systematic $q_{\text{inv}}^{\text{min}}$ dependence analysis	73
6.5	Systematic dependence of the source parameters for fig.1 of ref. [35] on $q_{\text{inv}}^{\text{max}}$	73
6.6	Systematic dependence of the source parameters for fig.2a of ref. [35] on $q_{\text{inv}}^{\text{max}}$	74
6.7	Systematic dependence of the source parameters for fig.2b of ref. [35] on $q_{\text{inv}}^{\text{max}}$	74
6.8	Systematic R_{halo} dependence of the source parameters for fig. 1 of ref. [35]	74
6.9	Systematic R_{halo} dependence of the source parameters for fig. 2a of ref. [35]	74
6.10	Systematic R_{halo} dependence of the source parameters for fig. 2b of ref. [35]	75
6.11	Lévy $S(r_{12})$ test	79
6.12	Direct Lévy fit to $S(r_{12})$ 12 data of ref. [35]	80
6.13	Test of the numeric routines	81
7.1	Slope of identified particle spectra at PHENIX	85
9.1	Elliptic flow versus w	115
9.2	PHENIX and STAR $v_2(p_t)$	120
9.3	PHOBOS $v_2(\eta)$	121
10.1	The coordinate transformation	127
10.2	Transverse mass dependence of the HBT radii	128
10.3	HBT radii versus η	130
11.1	Fluid trajectories of the new solution	133
11.2	$\frac{dn}{d\eta}$ and resulting correction to the Bjorken-estimate	134
11.3	Fits to RHIC $\sqrt{s_{\text{NN}}} = 130$ and 200 GeV data	135

List of Tables

2.1	PHENIX central arm detectors	20
2.2	PHENIX detectors outside of the central arm	21
3.1	ZDC channels	29
3.2	Drawing functions	30
4.1	SMD channels	43
6.1	Results on λ , R and α	72
6.2	Systematic q_{max} dependence analysis	75
6.3	Systematic q_{max} dependence analysis	76
6.4	Systematic q_{max} dependence analysis	77
6.5	Systematic R_{halo} dependence analysis	78
6.6	Final parameters with errors	82
9.1	Elliptic flow fit results from the Buda-Lund model	119

Bibliography

- [1] S. Weinberg, *The First Three Minutes* (Basic Books, New York, 1977).
- [2] S. S. Adler *et al.*, Phys. Rev. Lett. **91**, 072303 (2003).
- [3] K. Adcox *et al.*, Nucl. Phys. **A757**, 184 (2005).
- [4] M. Riordan and W. A. Zajc, Sci. Am. **294N5**, 24 (2006).
- [5] Feynman videos, <http://heelspurs.com/zpics/feynman9.rm>.
- [6] E. V. Shuryak, Nucl. Phys. **A750**, 64 (2005).
- [7] K. Adcox *et al.*, Phys. Rev. Lett. **88**, 022301 (2002).
- [8] S. S. Adler *et al.*, Phys. Rev. Lett. **91**, 072301 (2003).
- [9] K. Adcox *et al.*, Phys. Rev. Lett. **88**, 192303 (2002).
- [10] K. Adcox *et al.*, Phys. Rev. Lett. **89**, 082301 (2002).
- [11] K. Adcox *et al.*, Phys. Rev. **C66**, 024901 (2002).
- [12] K. Adcox *et al.*, Phys. Rev. Lett. **89**, 212301 (2002).
- [13] S. S. Adler *et al.*, Phys. Rev. Lett. **91**, 182301 (2003).
- [14] A. Adare *et al.*, Phys. Rev. Lett. **98**, 162301 (2007).
- [15] S. S. Adler *et al.*, Phys. Rev. Lett. **98**, 132301 (2007).
- [16] T. J. Humanic, Phys. Rev. **C73**, 054902 (2006).
- [17] C. Adler *et al.*, Nucl. Instrum. Meth. **A470**, 488 (2001).

- [18] M. Chiu *et al.*, Phys. Rev. Lett. **89**, 012302 (2002).
- [19] A. J. Baltz, C. Chasman, and S. N. White, Nucl. Instrum. Meth. **A417**, 1 (1998).
- [20] PHENIX Online Monitoring,
http://www.phenix.bnl.gov/WWW/run/??/online_monitoring/.
- [21] ZDC and SMD online monitoring code,
<http://www.phenix.bnl.gov/viewcvs/online/monitoring/Run3/subsystems/zdc>.
- [22] R. Hanbury Brown and R. Q. Twiss, Nature **178**, 1046 (1956).
- [23] T. Csörgő, B. Lörstad, J. Schmid-Sorensen, and A. Ster, Eur. Phys. J. **C9**, 275 (1999).
- [24] S. E. Vance, T. Csörgő, and D. Kharzeev, Phys. Rev. Lett. **81**, 2205 (1998).
- [25] J. I. Kapusta, D. Kharzeev, and L. D. McLerran, Phys. Rev. **D53**, 5028 (1996).
- [26] Z. Huang and X.-N. Wang, Phys. Rev. **D53**, 5034 (1996).
- [27] T. Hatsuda and T. Kunihiro, Phys. Rept. **247**, 221 (1994).
- [28] E. O. Alt, T. Csörgő, B. Lörstad, and S.-S. rensen, hep-ph/0103019.
- [29] T. Csörgő, B. Lörstad, and J. Zimányi, Z. Phys. **C71**, 491 (1996).
- [30] T. Csörgő, Phys. Lett. **B409**, 11 (1997).
- [31] T. Csörgő, S. Hegyi, and W. A. Zajc, Eur. Phys. J. **C36**, 67 (2004).
- [32] H. Boggild *et al.*, Phys. Lett. **B455**, 77 (1999).
- [33] M. Biyajima, M. Kaneyama, and T. Mizoguchi, Phys. Lett. **B601**, 41 (2004).
- [34] S. S. Adler *et al.*, Phys. Rev. Lett. **93**, 152302 (2004).
- [35] S. S. Adler *et al.*, Phys. Rev. **D74**, 072002 (2006).
- [36] T. Csörgő, S. Hegyi, T. Novak, and W. A. Zajc, AIP Conf. Proc. **828**, 525 (2006).
- [37] K. Rajagopal and F. Wilczek, Nucl. Phys. **B399**, 395 (1993).

- [38] S. S. Adler *et al.*, Phys. Rev. **C69**, 034909 (2004).
- [39] T. Csörgő *et al.*, Phys. Rev. **C67**, 034904 (2003).
- [40] T. Csörgő and B. Lörstad, Phys. Rev. **C54**, 1390 (1996).
- [41] M. Csanád, T. Csörgő, B. Lörstad, and A. Ster, Acta Phys. Polon. **B35**, 191 (2004).
- [42] M. Csanád, T. Csörgő, B. Lörstad, and A. Ster, nucl-th/0402037.
- [43] T. Csörgő, M. Csanád, B. Lörstad, and A. Ster, Acta Phys. Hung. **A24**, 139 (2005).
- [44] A. Ster, T. Csörgő, and B. Lörstad, Nucl. Phys. **A661**, 419 (1999).
- [45] T. Csörgő, Heavy Ion Phys. **15**, 1 (2002).
- [46] N. M. Agababyan *et al.*, Phys. Lett. **B422**, 359 (1998).
- [47] Y. Aoki *et al.*, Nature **443**, 675 (2006).
- [48] Z. Fodor and S. D. Katz, JHEP **04**, 050 (2004).
- [49] M. Csanád, T. Csörgő, B. Lörstad, and A. Ster, J. Phys. **G30**, S1079 (2004).
- [50] M. Csanád, T. Csörgő, and B. Lörstad, Nucl. Phys. **A742**, 80 (2004).
- [51] B. B. Back *et al.*, Phys. Rev. Lett. **89**, 222301 (2002).
- [52] S. Manly *et al.*, Nucl. Phys. **A715**, 611 (2003).
- [53] J. P. Bondorf, S. I. A. Garpman, and J. Zimányi, Nucl. Phys. **A296**, 320 (1978).
- [54] T. Csörgő, Acta Phys. Polon. **B37**, 483 (2006).
- [55] T. Csörgő, Central Eur. J. Phys. **2**, 556 (2004).
- [56] T. Csörgő and J. Zimányi, Heavy Ion Phys. **17**, 281 (2003).
- [57] T. Csörgő, F. Grassi, Y. Hama, and T. Kodama, Phys. Lett. **B565**, 107 (2003).
- [58] T. Csörgő, L. P. Csernai, Y. Hama, and T. Kodama, Heavy Ion Phys. **A21**, 73 (2004).
- [59] T. Csörgő and B. Lörstad, Nucl. Phys. **A590**, 465c (1995).

- [60] T. Csörgő and A. Ster, *Heavy Ion Phys.* **17**, 295 (2003).
- [61] T. Csörgő, M. I. Nagy, and M. Csanád, nucl-th/0605070.
- [62] S. V. Akkelin *et al.*, *Phys. Lett.* **B505**, 64 (2001).
- [63] W. Broniowski and W. Florkowski, *Phys. Rev. Lett.* **87**, 272302 (2001).
- [64] T. Csörgő and L. P. Csernai, *Phys. Lett.* **B333**, 494 (1994).
- [65] B. B. Back *et al.*, *Phys. Rev. Lett.* **94**, 122303 (2005).
- [66] B. B. Back *et al.*, *Phys. Rev.* **C72**, 051901 (2005).
- [67] J. Adams *et al.*, *Phys. Rev.* **C72**, 014904 (2005).
- [68] C. Adler *et al.*, *Phys. Rev. Lett.* **87**, 182301 (2001).
- [69] P. Sorensen, *J. Phys.* **G30**, S217 (2004).
- [70] J. Adams *et al.*, *Nucl. Phys.* **A757**, 102 (2005).
- [71] F. Grassi, Y. Hama, O. Socolowski, and T. Kodama, *J. Phys.* **G31**, S1041 (2005).
- [72] Y. M. Sinyukov and I. A. Karpenko, *Acta Phys. Hung.* **A25**, 141 (2006).
- [73] S. Afanasiev *et al.*, nucl-ex/0703024.
- [74] D. Kharzeev and E. Levin, *Phys. Lett.* **B523**, 79 (2001).
- [75] S. Pratt, *Phys. Rev.* **D33**, 1314 (1986).
- [76] Y. Hama *et al.*, *Nucl. Phys.* **A774**, 169 (2006).
- [77] W. Broniowski, A. Baran, and W. Florkowski, *AIP Conf. Proc.* **660**, 185 (2003).
- [78] S. Pratt, nucl-th/0612010.
- [79] J. D. Bjorken, *Phys. Rev.* **D27**, 140 (1983).
- [80] I. G. Bearden *et al.*, *Phys. Rev. Lett.* **88**, 202301 (2002).
- [81] I. G. Bearden *et al.*, *Phys. Lett.* **B523**, 227 (2001).

-
- [82] K. Adcox *et al.*, Phys. Rev. Lett. **88**, 242301 (2002).
- [83] K. Adcox *et al.*, Phys. Rev. Lett. **88**, 192302 (2002).
- [84] B. B. Back *et al.*, Phys. Rev. Lett. **87**, 102303 (2001).
- [85] C. Adler *et al.*, Phys. Rev. Lett. **87**, 082301 (2001).
- [86] M. Csanád *et al.*, nucl-th/0512078.
- [87] M. Csanád, Nucl. Phys. **A774**, 611 (2006).
- [88] M. Csanád, nucl-ex/0505001.
- [89] S. S. Adler *et al.*, Phys. Rev. **C74**, 024904 (2006).
- [90] S. S. Adler *et al.*, Phys. Rev. **C73**, 054903 (2006).
- [91] S. S. Adler *et al.*, Phys. Rev. Lett. **96**, 012304 (2006).
- [92] S. S. Adler *et al.*, Phys. Rev. Lett. **94**, 082302 (2005).
- [93] S. S. Adler *et al.*, Phys. Rev. Lett. **94**, 232302 (2005).
- [94] S. S. Adler *et al.*, Phys. Rev. **C71**, 051902 (2005).
- [95] S. S. Adler *et al.*, Phys. Rev. Lett. **93**, 202002 (2004).
- [96] M. Csanád, PHENIX internal technical note 419.
- [97] D. d'Enterria, nucl-ex/0601001.
- [98] M. Chiu *et al.*, PHENIX internal analysis note 593.
- [99] M. Csanád and T. Csörgő, PHENIX internal analysis note 404.
- [100] M. Csanád and T. Csörgő, PHENIX internal analysis note 436.
- [101] M. Csanád, T. Csörgő, and M. Nagy, hep-ph/0702032.
- [102] M. Csanád, T. Csörgő, and M. Nagy, PHENIX internal analysis note 527.
- [103] M. Csanád, T. Csörgő, and B. Lörstad, nucl-th/0402036.

- [104] M. Csanád, T. Csörgő, B. Lörstad, and A. Ster, Nucl. Phys. **A774**, 535 (2006).
- [105] M. Csanád, T. Csörgő, B. Lörstad, and A. Ster, AIP Conf. Proc. **828**, 479 (2006).
- [106] M. Csanád, T. Csörgő, R. A. Lacey, and B. Lörstad, nucl-th/0605044.